

*see back page  
1473*

*12*

*2*

AC 1050355

AD NO. \_\_\_\_\_  
DDC FILE COPY

## Semiannual Technical Summary

DDC  
RECEIVED  
MAR 1 1978  
F

## Seismic Discrimination

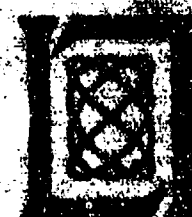
30 September 1977

Prepared for the Defense Advanced Research Projects Agency  
under Electronic Systems Division Contract F19628-76-C-0002 by

### Lincoln Laboratory

MASSACHUSETTS INSTITUTE OF TECHNOLOGY

LINCOLN, MASSACHUSETTS



Approved for public release; distribution unlimited.

The work reported in this document was performed at Lincoln Laboratory, a center for research operated by Massachusetts Institute of Technology. This research is a part of Project Vein Uniform, which is sponsored by the Defense Advanced Research Projects Agency under Air Force Contract F19628-76-C-0002 (ARPA Order 512).

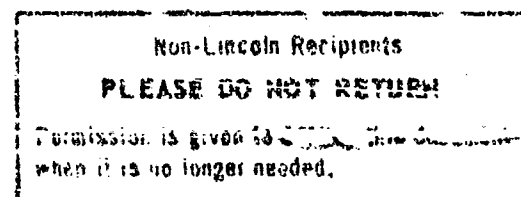
This report may be reproduced to satisfy needs of U.S. Government agencies.

The views and conclusions contained in this document are those of the contractor and should not be interpreted as necessarily representing the official policies, either expressed or implied, of the United States Government.

This technical report has been reviewed and is approved for publication.

FOR THE COMMANDER

*Raymond L. Loiosello*  
Raymond L. Loiosello, Lt. Col., USAF  
Chief, ESD Lincoln Laboratory Project Office



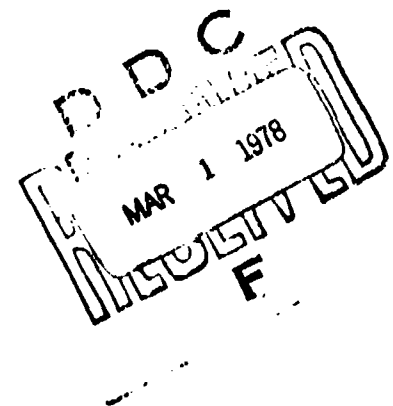
MASSACHUSETTS INSTITUTE OF TECHNOLOGY  
LINCOLN LABORATORY

SEISMIC DISCRIMINATION

SEMIANNUAL TECHNICAL SUMMARY REPORT  
TO THE  
DEFENSE ADVANCED RESEARCH PROJECTS AGENCY

1 APRIL - 30 SEPTEMBER 1977

ISSUED 5 JANUARY 1978



Approved for public release; distribution unlimited.

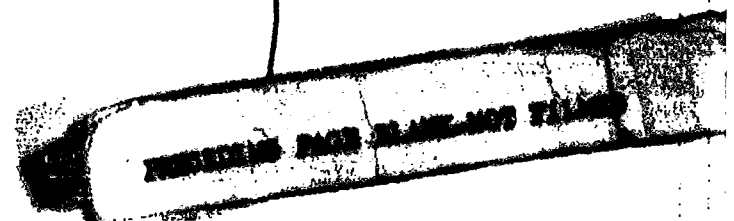
LEXINGTON

MASSACHUSETTS

# ABSTRACT

This report describes 21 investigations in the field of seismic discrimination. These are grouped as follows: surface-wave studies (6 contributions), studies of seismic scaling and body-wave magnitude  $m_b$  (4 contributions), miscellaneous studies (5 contributions), and investigations related to data analysis and computer systems (6 contributions).

ACCESSION for		
NRIS	2-1-68	13
DDC	2-1-68	13
DISPATCHED		13
BY		
DISTRICT CHAIRMAN		COPIES
13		SPECIAL
A		



## CONTENTS

Abstract	iii
Summary	v
<b>I. SURFACE-WAVE STUDIES</b>	<b>1</b>
A. Enhancement of Rayleigh Waves of Explosions Using Polarization Filtering	1
B. A Comparison of Love- and Rayleigh-Wave Discriminants at Mashhad SRO	2
C. A Rayleigh-Wave Structure for Novaya Zemlya: Results from More Data Analyses	3
D. A Comparison of P-Wave and Surface-Wave Focal- Mechanism Solutions for Three Sinkiang Earthquakes	6
E. Group Velocities Across Tibet to Mashhad SRO	7
F. Group Velocities in the West Pacific	8
<b>II. SEISMIC SCALING AND BODY-WAVE MAGNITUDE <math>m_b</math></b>	<b>27</b>
A. Moments and Stress Drops for the Rat Island Sequence of 1965	27
B. Incorrect Seismic Scaling from $m_b$	28
C. $m_b$ -Frequency Relations from Seismic Scaling Laws	30
D. Saturation of the $m_b$ Scale	32
<b>III. MISCELLANEOUS STUDIES</b>	<b>43</b>
A. An Analysis of the MAIO Recording of the 20 March 1976 Eastern Kazakh Event	43
B. Crustal-Phase Travel Times from NTS Explosions: Preliminary Results	44
C. The Depth of Seismicity in an Iranian Aftershock Sequence	46
D. Two-Dimensionalized Velocity Anomalies	47
E. Precise Location of Oceanic Ridge Earthquakes	48
<b>IV. DATA ANALYSIS AND COMPUTER SYSTEMS</b>	<b>63</b>
A. Transfer Functions for the Seismic Research Observatory Seismograph System	63
1. The Seismometer	63
2. Response-Shaping Filters	64
3. Anti-alias Filters	64
4. Overall Response Characteristics	66
B. Detection Results for an SRO Network	68
C. Automatic Picking of First Arrivals	69
D. PDP-11 System Software	71
E. UNIX Signal Display Package	71
F. Datacomputer-Related UNIX Software	73
Glossary	81

## SUMMARY

This is the twenty-seventh Semiannual Technical Summary report describing the activities of Lincoln Laboratory, M.I.T., in the field of seismic discrimination. This report covers the period 1 April to 30 September 1977. The objective of the Lincoln Laboratory program is to carry out fundamental research into the seismological problems associated with the detection, location, and identification of earthquakes and nuclear explosions, and with the estimation of explosion yields. In order to investigate these problems, we are continuously improving our ability to manipulate and process seismic data from a global network of high-quality digital stations and arrays.

Several investigations related to surface-wave propagation are described. Polarization filtering has been shown to be capable of enhancing the Rayleigh waves received at Mashhad Seismic Research Observatory (SRO) from presumed explosions in Eastern Kazakh. In particular, it is demonstrated that this technique will be valuable in separating the surface-wave trains from interfering events. A preliminary attempt to use Mashhad  $M_g$  values in application of the  $M_g$ - $m_b$  criterion to Eurasian events is quite successful. Separation of the explosion and earthquake populations is generally good, but one presumed explosion is not identified — perhaps due to unusual tectonic strain release. We have continued to improve our analysis of the crustal structure at Novaya Zemlya by comparing the data from two test sites on the island as observed at ALPA. A crustal thickness of 45 km appears to give a best fit to the data. A comparison of focal mechanisms determined by a recent surface-wave spectral amplitude fitting procedure with those obtained from long-period (LP) body waves shows rather large discrepancies. Our planned experiment to carry out a large-scale inversion of Eurasian group-velocity dispersion data is continuing, and requires data from more SRO sites soon to be operational. Data from a limited area in Southeastern Asia, as observed at Mashhad SRO, again document the low group velocities associated with the Tibetan plateau, and indicate that these velocities persist to the north of the plateau.

We have continued our efforts to understand the scaling of the seismic source and its effect on determinations of  $m_b$ . One study has shown that observations of  $m_b$  vs period for the Rat Island sequence (1965) are consistent with a relatively constant stress drop of about 25 bars. Estimates of seismic moment appear to agree well with other methods. Another investigation has studied the effect of the corner frequency and high-frequency fall-off in the seismic spectrum on the dominant period as observed through several short-period (SP) seismograph systems. It is shown that  $m_b$ , as usually measured, is not a consistent measure of spectral amplitude at 1 Hz unless corrections for corner frequency and path attenuation are included. Information about the seismic source can also be obtained from the saturation of the  $m_b$  scale as observed in frequency-magnitude data if an earlier-derived linear relation between  $\log$  (frequency) and  $\log$  (moment) is assumed to be correct. Observational data appear to be consistent with a high-frequency decay of the seismic spectrum intermediate between  $\omega^{-2}$  and  $\omega^{-3}$ .

Several other studies have been completed. We have carried out deconvolution and maximum entropy spectral analysis of the Mashhad SRO recording of the Eastern Kazakh event of 20 March 1976. This was an unusual event, and is clearly multiple. Our best interpretation of this record suggests that at least one of the sources was an earthquake, although further

data are needed to completely dispose of the possibility that it was a sequence of explosions. We have begun a study of discrimination at near-regional distances by compiling a set of LRSM data from U.S. explosions. The effects of crustal inhomogeneity and the difficulty in measuring the onset times of S phases are apparent in this data set. In another study, the application of the master-event technique to the teleseismic determination of focal depth is examined. In the study of an aftershock sequence in Iran, it was possible to determine relative epicenters and focal depths to considerable precision.

In the general areas of data analysis and computer systems, several studies are described. We have completed a careful study of the response characteristics of the SRO instrument. We note that the anti-alias filter has been removed from the SP SRO system, and we recommend that attempts be made to design a new anti-alias filter. We have examined the detection thresholds on the existing SRO SP systems by evaluating the detections at each station. We conclude that several of these thresholds are set too high. A new algorithm for the automatic picking of first arrivals is described which appears to show distinct advantages over current techniques.

We are continuing to upgrade the capabilities of our PDP-11 computer system. Currently, the major emphasis of our software program is aimed toward implementation of a multiple-CPU operating system, the development of a graphics package oriented specifically for seismological research, and the improvement of our interface with the datacomputer.

M. A. Chinnery

## SEISMIC DISCRIMINATION

### I. SURFACE-WAVE STUDIES

#### A. ENHANCEMENT OF RAYLEIGH WAVES OF EXPLOSIONS USING POLARIZATION FILTERING

Two-dimensional polarization filtering<sup>1</sup> is being used to enhance Rayleigh waves from explosions. Here, we show four examples of enhanced surface waves from presumed explosions in Eastern Kazakh recorded at the Mashhad SRO (MAIO).

The polarization scheme is based on the particle motion ellipse of the two components of motion, Z and R.<sup>1</sup> For Rayleigh waves, the Z and R components are 90° out of phase for all frequencies. The method we use is to shift the phase of R by +90°, thus making all Rayleigh components in phase with the Z component. The motion then appears to be highly polarized in a linear direction, such that  $d_1 \gg d_2$ , where  $d_1$  and  $d_2$  are the major and minor ellipse axes of the particle motion in the (R, Z) plane. The major component along  $d_1$  is projected onto the R and Z axes and scaled by a nonlinear filter  $f$  which was previously defined<sup>1</sup> by

$$f = 1 - e \quad (I-1)$$

where  $e$  equals the ellipticity of the particle ellipse given by  $e = d_2/d_1$ . Finally, R is shifted by -90° to restore its original polarity.

This filter passes waves with amplitude 1 when  $d_2/d_1 = 0$  and attenuates them gradually as  $d_2 \rightarrow d_1$ . Figure I-1 shows this filter response as a function of  $e$ . It smoothly attenuates waves as  $e \rightarrow 1$ , with the sharpest cutoff occurring near  $e = 1$ .

We have incorporated a better filter into the polarization program which is analogous to the Butterworth filter of order  $n$  used in frequency filtering. It has the formula

$$g = [1 + (e/e_0)^n]^{-1/2} \quad (I-2)$$

and is displayed in Fig. I-1 for orders  $n = 3$  and  $6$  with a 3-dB cutoff ellipticity  $e_0 = 0.2$ . This filter produces better rejection above  $e_0$  than is possible using Eq. (I-1). For  $e < e_0$ , a high-order filter produces a flat response for passing linearly polarized waves with some noise present.

This filter was used in the polarization program to pass surface waves from four explosions in Eastern Kazakh recorded at MAIO. The results are shown in Figs. I-2, I-3, and I-4. In each of these figures the two top traces, (a), are Z and R components, bandpass-filtered with a phase-free 6-pole filter to pass 0.02 to 0.08 Hz. The next two traces, (b), in each figure are the results of polarizing the data of the top two traces using the filter  $g$  of order 3, which is displayed as a function of time in trace 5. The two traces which follow, (c), are the polarized results using a 6th-order filter, which is displayed in trace 8.

In Fig. I-2, the explosion has an  $m_b$  of 5.8 with a very clear Rayleigh wave on the unpolarized traces. The main effect of polarization is to reduce the noise level somewhat without distorting the frequency content or amplitude of the surface wave.

Figure I-3(a) contains a smaller Rayleigh wave, masked in the coda of a larger earthquake. The earthquake coda is complex, containing many scattered arrivals which are not simply surface waves along the R direction. Thus, polarization in Figs. I-3(b) and I-3(c) clearly passes



the explosion Rayleigh wave with little amplitude reduction while reducing the earthquake coda level. Some dispersion is also preserved in the passed waves.

In Fig. I-4(a), two reported Kazakh explosions occurred within 5 min. of each other, both surface waves being masked by a larger earthquake coda. The polarization results in Figs. I-4(b) and I-4(c) show an increase in the signal/noise ratio (SNR) of the surface waves for the two events, at the expense of significant amplitude attenuation. The filter values  $g$  are only about  $\sim 0.25$  for these two Rayleigh waves; however, the filter peaks indicate the presence of surface waves which could be correlated by an analyst to clearer arrivals at other stations.

These results show that polarization filtering can be a useful detection and enhancement scheme for surface waves which does not introduce severe signal distortion when the SNR is high. The sensitivity of the method also makes it susceptible to false alarms, which would have to be eliminated by a network correlation of all the phases.

C. W. Frasier

#### B. A COMPARISON OF LOVE- AND RAYLEIGH-WAVE DISCRIMINANTS AT MASHHAD SRO

Theoretically, the relative generation of Love and Rayleigh waves is a powerful discriminant between earthquakes and explosions. The fact that Love waves are generated by explosions at all indicates some degree of tectonic stress release resulting in dipole and quadrupole source components in addition to the monopole components generated by an ideal explosion source. A convenient way of representing this tectonic stress release is given by the 'F' factor,<sup>2</sup> being the relative strength of multipolar to monopole source components. Values of  $F$  as high as 3 have been observed.<sup>2</sup> Spectral ratios of Love-to-Rayleigh waves have been suggested as a discriminant, but have not met with much success.<sup>2,3</sup>

We present here the results of a preliminary test of the relative discrimination capabilities of  $M_S$  vs  $m_b$ , where  $M_S$  is calculated from the maximum amplitudes of Rayleigh ( $M_S^R$ ) and Love ( $M_S^L$ ) waves recorded at MAIO. Our explosion dataset is necessarily rather small since we only have data for the first 9 months of 1976. During this time period, there were 9 presumed explosions in the USSR whose epicentral parameters are given in Table I-1. In addition, an event very close to the Eastern Kazakh test site took place on 20 March 1976; it has been identified as an earthquake in the PDF. A special study of this event was made in the previous SATS.<sup>1</sup>

Our earthquake dataset consists of 67 earthquakes within Eurasia recorded at distances of up to  $50^\circ$  from MAIO. Figure I-5 shows the location of the sources used. For both the earthquakes and the explosions, the horizontal seismograms were rotated into the epicenter azimuth and  $M_S^L$  measured from the transverse component through

$$M_S^L = 1.66 \log \Delta + \log \left( \frac{A}{T} \right)$$

where  $A$  is the maximum peak-to-peak amplitude of Love waves, and  $T$  is the dominant period.  $M_S^R$  was measured from the vertical component.  $T$  ranged from 16 to 22 sec for both explosions and earthquakes; these periods for explosions differ considerably from those recorded on WWSSN instruments for which  $T$  is often as small as 12 sec. This difference is primarily due to the longer period response of the SRO instrumentation.

TABLE I-1 PDE EPICENTRAL PARAMETERS OF PRESUMED EXPLOSIONS IN USSR, JANUARY - SEPTEMBER 1976 (Event 10 is identified by the PDE as an Earthquake)				
Event	Date	Time	Location	$m_b$
1	15 January	04:46:57.6	E. Kazakh	5.2
2	21 April	04:47:57.6	E. Kazakh	5.1
3	21 April	05:02:57.4	E. Kazakh	5.3
4	19 May	02:56:57.9	E. Kazakh	5.0
5	4 July	02:56:57.7	E. Kazakh	5.8
6	23 July	02:32:57.9	E. Kazakh	5.1
7	29 July	04:59:57.5	W. Kazakh	5.8
8	28 August	03:56:57.5	E. Kazakh	5.8
9	29 September	02:59:57.4	Novaya Zemlya	5.8
10	20 March	04:03:39.3	E. Kazakh (Earthquake?)	5.1

Figure I-6 shows the  $M_S^R$  and  $M_S^L$  values obtained; it can be seen that the line  $M_S^L = M_S^R$  is a very good fit to the explosion population. All the explosions fall below this line, but not sufficiently well to be useful as a discriminant. Figures I-7 and I-8 are  $M_g$ -vs- $m_b$  plots for  $M_S^R$  and  $M_S^L$ , respectively. The  $m_b$  values are taken from the PDE; for nearly all the earthquakes, and all the explosions, these are based on 10 or more observations. Due to large interfering events, we were unable to measure  $M_g$  for events 1 and 4.

It can be seen that, with one exception (event 6), the separation of the explosion and earthquake populations is good.  $M_S^L$  vs  $m_b$  appears to be a slightly better discriminant than  $M_S^R$  vs  $m_b$ ; excluding event 6, the separation of the two populations is 0.5  $M_g$  units using  $M_S^R$ , and 0.8 units using  $M_S^L$ . The failure of either to place event 6 in the explosion population is distressing; this event must have involved abnormally high tectonic stress release. This study will be continued as more SRO data become available.

R. G. North

#### C. A RAYLEIGH-WAVE STRUCTURE FOR NOVAYA ZEMLYA: RESULTS FROM MORE DATA ANALYSES

The continuing series of large (presumed) explosions at Novaya Zemlya generated unusually clear Rayleigh waves. Recordings of these, made at the Alaskan Long-Period Array (ALPA), were used to infer the crust and upper-mantle structure of Novaya Zemlya. For this experiment, we had data from five explosions which appeared to originate in two source regions. The first is a northern test site located near the channel separating the southernmost island in the chain. The second is a southern test site at the southern end of that island. A great-circle path passing through these two test sites also passes very close to ALPA. Thus, pairs of events in the northern and southern test sites, respectively, can be used to determine the structure in the

TABLE I-2 PDE EPICENTERS				
Event	Origin Time	Latitude (°N)	Longitude (°E)	m <sub>b</sub>
28 August 1972	05:59:56.5	73.34	55.09	6.3
2 November 1974	04:59:56.7	70.82	54.06	6.7
23 August 1975	08:59:57.9	73.37	54.64	6.4
18 October 1975	08:59:56.3	70.84	53.69	6.7
21 October 1975	11:59:57.3	73.35	55.08	6.5

TABLE I-3 NOVAYA ZEMLYA STRUCTURAL MODEL LAYER PARAMETERS				
Layer	Thickness (km)	P Velocity (km/sec)	S Velocity (km/sec)	Density (km/sec)
1	9	6.02	2.83	2.80
2	10	6.13	3.22	2.61
3	26	6.56	3.94	3.12
4	32	8.18	4.40	3.21
5	30	8.07	4.46	3.33
6	75	7.90	4.44	3.44
7	75	8.10	4.45	3.49
8	100	8.30	4.60	3.55
9	100	9.00	4.95	3.65
10	∞	9.75	5.37	3.95

source region, i.e., the common path between the events across the southern island of Novaya Zemlya. The appropriate method is the single-station, two-event method due to Alexander.<sup>4</sup>

ALPA center section seismograms from the five events are shown in Fig. I-9. Corresponding PDE information is given in Table I-2. In order to insure uniform epicenter accuracy, the five events were relocated using a common set of 35 stations. After constraining the depth of each event to zero, the resulting epicenter confidence error ellipses were all  $1.64 \text{ km}^2$ . The relocation procedure was necessary because the resulting phase velocities are inversely proportional to the relative event separation. The average test-site separation was approximately 285 km.

The method consists of computing the array-averaged cross-power spectral-density function. The phase of this is the phase velocity dispersion in the source region because the explosive source phase, instrument phase, and common path phase velocity dispersion from the northern event to ALPA all cancel. The amplitude of the cross power is the relative cross power in the two events. The phase velocity dispersion difference between northern and southern events can be easily seen in Fig. I-9 where the northern are events 1, 3, and 5, and the southern are events 2 and 4. The third event, 23 August 1975, is unusual in that it has noticeably less LP energy than the other two northern events. It has, however, the same apparent phase velocity dispersion.

ALPA is ideally suited to observing events in Novaya Zemlya. The propagation path crosses the Arctic Ocean basin, conveniently avoiding the North American and Eurasian continental shelves. Thus, interference due to multipathing is minimal. Little of this effect is apparent in the seismograms. The instrument response and propagation-path attenuation were such that dispersion could be measured over three octaves of signal bandwidth: from 8 to 64 sec period.

The measured phase velocities, their estimated errors, and the phase velocity dispersion from the best-fitting model are shown in Fig. I-10. The rms error of the input data was 0.082 km/sec. The phase velocity dispersion from the model fits the data with an rms error of 0.045 km/sec. Its layer parameters are given in Table I-3 and plotted in Fig. I-11. As can be seen in Fig. I-10, the data show slight phase velocity minima at approximately the 36, 21, and 13 sec periods. This could be due either to multipathing interference or the presence of dipping layers in the source region. The model does not account for either of these effects.

The model was obtained by generalized linear inversion of the phase velocity dispersion data. The method has been well reported in the literature; our particular version is due to Rodi *et al.*<sup>5</sup> The well-known Gutenberg Continent structural model<sup>6</sup> was used as a starting model. Several runs of the inverse program were made with different crustal thicknesses. A 45-km-thick crust appeared to give the best fit to our data.

Rayleigh-wave-dispersion data are known to delineate the shear-wave-velocity profile much better than either the compressional velocity or density profiles.<sup>7</sup> We therefore consider our shear-wave-velocity profile to be the major result of this inversion experiment; it is shown plotted in Fig. I-12 along with the corresponding shear-wave velocity from the starting Gutenberg Continent model. The major differences consist of lower velocities in the first two crustal layers and the virtual elimination of the low-velocity zone.

There is no specific information in the open literature concerning the structure of Novaya Zemlya. Kosminskaya *et al.*<sup>8</sup> give a Moho depth contour map of the USSR indicating that Novaya Zemlya is a northern extension of the Ural mountain belt. Various geological maps of the USSR support this. The actual Moho depth, or crustal thickness, given on the contour map is between

35 and 40 km. Our data do not support such a thin crust. In fact, the original Gutenberg Continent crust is 38 km thick. It seems unreasonable that even an old mountain belt would only be as thick as a typical continent. Our crustal thickness, 45 km, is only 7 km thicker than Gutenberg's typical continental crust.

The lack of a low-velocity zone in the shear-wave-velocity profile is indicative of an old, stable structure. Our particular profile does, in fact, resemble Ukrainian shield profiles presented by Kosminskaya *et al.*<sup>8</sup> Although these are appropriate to the continental USSR, they do represent the crust in the Ural mountains region. To summarize: our phase velocity dispersion data indicate a relatively old, stable shear-wave structure with a 45-km-thick crust.

D. W. McCowan  
P. Glover†  
S. S. Alexander†

#### D. A COMPARISON OF P-WAVE AND SURFACE-WAVE FOCAL-MECHANISM SOLUTIONS FOR THREE SINKIANG EARTHQUAKES

In a recent report,<sup>9</sup> Sun and Shaub use a surface-wave spectral amplitude fitting procedure to estimate the focal mechanism and depth of 19 events in the 1974 Sinkiang earthquake series. As a test of this procedure, their solutions for three of the largest events were superimposed on lower-hemisphere, equal-area plots of P-wave first motions. P-wave data were obtained from LP vertical WWSSN seismograms. The epicentral data and source parameters for these three events are given in Tables I-4 and I-5. Surface-wave mechanisms and P-wave first motions are compared in Figs. I-13, I-14, and I-15.

As the figures show, significant discrepancies exist between surface-wave solutions and the first motions. Large numbers of compressions are seen in quadrants that should contain only dilatations if the surface-wave solutions were compatible with the P-wave data. Furthermore, the solution displayed in Fig. I-15 seems to contradict what is known about the tectonics of the region. Shirokova,<sup>10</sup> Das and Filson,<sup>11</sup> and Molnar, Fitch, and Wu<sup>12</sup> have obtained many focal-mechanism solutions for this area and have found that the P-axis commonly trends approximately N-S. The trend of the P-axis in Fig. I-15 is nearly E-W.

Figure I-13 also shows a P-wave first-motion solution for event 1. Parameters for this solution are:

	<u>Strike</u>	<u>Dip</u>	<u>Slip</u>
Plane 1	50°	66SE	25°
Plane 2	310°	68NE	155°

	<u>Trend</u>	<u>Plunge</u>
P-axis	359°	02°
T-axis	269°	34°
B-axis	92°	57°

Plane 1 is well defined, and plane 2 is poorly defined. Although the data seem to suggest that a nodal plane should lie south of KEV and KBS, and north of NUR and GDH, none orthogonal to plane 1 could be drawn.

† Pennsylvania State University, University Park, PA.

TABLE I-4 EPICENTRAL DATA FOR THREE LARGE EVENTS OF 1974 SINKIANG SERIES						
Event	Date (1974)	Origin Time	Latitude (°N)	Longitude (°E)	$m_b$	Source
1	11 August	01:13:55.5	39.46	73.83	6.4	EDR
2	11 August	20:05:30.9	39.44	73.67	5.8	ISC
3	11 August	21:21:37.1	39.46	73.62	6.0	ISC

TABLE I-5 SOURCE PARAMETERS OBTAINED BY AMPLITUDE SPECTRAL FITTING <sup>9</sup>				
Event	Depth	Dip Angle (deg)	Slip Angle (deg)	Strike of Nodal Planes
1	10	90	0	75, 165
2	10	90	0	30, 120
3	6	50	-30	120

The discrepancies between the two types of focal-mechanism solutions are larger than were expected. Research into possible explanations for these differences, and into the reliability of the surface-wave spectral-amplitude-fitting procedure, is continuing.

M. W. Shields

#### E. GROUP VELOCITIES ACROSS TIBET TO MASHHAD SRO

We are continuing our study of group velocity dispersion across Eurasia, described earlier.<sup>1</sup> Although a large amount of SRO data is now available, progress in the inversion has been hampered by the following factors:

- (1) The extreme tardiness of PDE epicenter determinations,
- (2) Closure of the Taiwan SRO (TATO) for 8 months due to technical problems,
- (3) Delays in operation of Chiengmai (CHTO),
- (4) Large gain reduction at Guam (GUMO) which has rendered LP data from small events virtually unusable.

We have, however, collected surface-wave trains from over 200 events within and on the borders of Eurasia and recorded at Mashhad SRO (MAIO). These include some 80 events within the regions China, Tibet, Burma, and Mongolia. The locations of these events are shown in Fig. I-16. Many of the paths to these traverse the high-altitude region consisting of the

Himalayas, the Tibetan plateau, and the Hindu Kush, and the cross-hatched area shown on Fig. I-16 is at altitudes of 3000 m or greater. Paths leaving Mashhad at azimuths of 70° to 105° intersect this area (selected great-circle path shown).

Figure I-17 shows the envelopes of Rayleigh-wave group velocities measured at MAIO for events in the azimuth ranges 95° to 105° (Southern Tibet and the Himalayas), 80° to 90° (Northern Tibetan plateau), and 65° to 75° (Hindu Kush and Sinkiang), respectively. The lowest group velocities are those through Northern Tibet (80° to 90° azimuth), and the highest (though still remarkably low by comparison with dispersion for platform or shield regions) are those which cross the Himalayas. Perhaps the most remarkable feature of the data, however, is the continuation of these low group velocities in the most northerly azimuth sector, indicating that the anomalously low-velocity structure persists to the north of the Tibetan plateau as outlined by the cross-hatched region. These low group velocities abruptly cease for paths at azimuths of less than 65°, as can be seen from Fig. I-18 which shows dispersion for paths to Northern Sinkiang and Mongolia compared with those for Tibet. (The shaded region here is the envelope of the group velocity regions shown in Fig. I-17.)

Perhaps the most striking illustration of the effect of the Himalayas and Tibet upon group velocity is given by Fig. I-19 which shows group velocities to events in Burma and Szechwan. Dispersion to event 45 (Szechwan, path almost entirely through Tibet) is up to 0.5 km/sec slower than that to event 9 (Southern Burma), and it can be seen that the group velocities increase steadily as we move the source from north to south. Also shown on the figure is the dispersion calculated by Teng<sup>13</sup> for a model designed to fit his data for paths crossing Southern Tibet. The paths he used are similar to those for event 41 and the agreement is good. The remarkably slow results for event 45 are not therefore too surprising, since its path comprises more than twice as much of the Tibetan plateau as that for event 41.

Station CHTO has just come into operation and as soon as data are available we shall be able to further determine the precise outline of the low-velocity region in Central Asia.

R. G. North

#### F. GROUP VELOCITIES IN THE WEST PACIFIC

During the past six months, the frequency-filter method has been used to obtain dispersion curves for over 100 paths originating in the vicinity of the West Pacific and recorded at three SRO stations - GUMO (Guam), SNZO (New Zealand), and NWA0 (Australia). Paths are shown in Fig. I-20, along with major topological features of the area. The region is noted for peculiarities in both mantle and crustal properties. In particular, the Fiji Plateau is noted for high seismic attenuation and slow P-wave velocities,<sup>14,15</sup> and the Ontong-Java Rise, to the north of the Solomon Islands, has been recently shown by refraction studies to have a crustal thickness appropriate for continental structures.<sup>16</sup>

Group velocities are shown for several paths to GUMO in Fig. I-21(a-e). Velocities for paths from Melanesia to Guam changed in a systematic fashion as paths included more of the Fiji Plateau and the Ontong-Java Rise. Paths from Samoa [Fig. I-21(a)] gave the highest group velocities; these are in close agreement with velocities derived from the Dorman oceanic model 3099 (Ref. 17), shown in the figure for comparison. Paths from Kermadec [Fig. I-21(b)], which crossed both the Fiji and the Ontong-Java plateaus, showed a marked drop in group velocity at all frequencies relative to the Samoa paths. The results are more closely matched by

model ARC-1 (Ref. 18), derived from a path from the Banda Sea to Japan. The lowered velocities and the greater dispersion at short periods reflect the anomalous mantle of the Fiji Plateau and the thickened crust in the Ontong-Java region. Paths from the New Hebrides, Loyalty Islands, Solomon Islands, and Santa Cruz [Figs. 1-21(c), (d), and (e)] show even greater dispersion at the low frequencies than do the Kermadec paths, reflecting the fact that a larger percentage of the path is through the thickened crustal region.

TABLE 1-6 LAYERED MODEL USED TO OBTAIN VELOCITIES SHOWN IN FIGS. 1-21(c), (d), AND (e)							
Model A				Model B			
h	$\alpha$	$\beta$	$\rho$	h	$\alpha$	$\beta$	$\rho$
2.0	1.52	0	1.03	25.0	1.52	0	1.03
1.5	2.6	1.09	2.3	1.5	2.60	0.84	2.3
3.0	5.4	2.96	2.6	3.0	5.4	3.0	2.6
6.0	6.1	3.53	2.8	5.0	6.1	3.45	2.8
17.0	6.9	3.98	2.9	15.0	6.9	3.93	2.9
50.0	8.2	4.48	3.5	50.0	8.2	4.46	3.5
50.0	7.9	4.25	3.9	50.0	7.9	4.28	3.4
250.0	8.2	4.45	3.5	250.0	8.2	4.46	3.5
250.0	9.8	5.40	3.96	250.0	9.8	5.40	3.96
150.0	10.0	5.90	4.21	150.0	10.0	5.90	4.21
-	11.5	6.38	4.95	-	11.5	6.38	4.95

The points plotted on Figs. 1-21(c), (d), and (e) are for velocities computed from two flat-layered models obtained using the Harkrider-Rodi FORTRAN inverse program. The models, given in Table 1-6, include a crustal thickness of 27.5 and 24.5 km, far too high for both oceanic and island arc structures. Hence, the data support the existence of an unusually thick crust in the Ontong-Java Rise.<sup>16</sup>

Paths to NWA0 from adjacent events in the Fiji Plateau region gave consistent results, and a systematic decrease in dispersion with increasing oceanic component was observed, as shown in Fig. 1-22. Paths from the Fiji Plateau to SNZO gave results intermediate between continental and oceanic, appropriate for island arc structures. Paths crossing Indonesia showed strong dispersion, in agreement with previous results.<sup>19</sup>

S. Seneff



# REFERENCES

1. Seismic Discrimination SATS, Lincoln Laboratory, M.I.T. (31 March 1977), DDC AD-A045453.
2. M. N. Toksöz, D. G. Harkrider, and A. Ben-Menahem, "Determination of Source Parameters by Amplitude Equalization of Seismic Surface Waves," *J. Geophys. Res.* **70**, 907-922 (1965).
3. D. G. Lambert, A. I. Tolstoy, and E. S. Becker, "Seismic Detection and Discrimination Capabilities of the Very Long Period Experiment - Final Report," Texas Instruments Inc. (December 1974).
4. S. S. Alexander, Unpublished Research Note, The Pennsylvania State University, University Park, PA (1969).
5. W. L. Rodi, P. Glover, T. M. C. Li, and S. S. Alexander, "A Fast, Accurate Method for Computing Group Velocity Partial Derivatives for Rayleigh and Love Modes," *Bull. Seismol. Soc. Am.* **65**, 1105-1114 (1975).
6. Y. Tsai and K. Aki, "Precise Focal Depth Determination From Amplitude Spectra of Surface Waves," *J. Geophys. Res.* **75**, 5729-5743 (1970).
7. R. Wiggins, "The General Linear Inverse Problem: Implications of Surface Waves and Free Oscillations on Earth Structure," *Rev. Geophys. Space Phys.* **10**, 251-285 (1972).
8. L. P. Kosminskaya, N. A. Belyaevsky, and I. S. Volovosky, "Explosion Seismology in the USSR," in *The Earth's Crust and Upper Mantle*, Geophysical Monograph 13 (American Geophysical Union, Washington, DC, 1969).
9. D. Sun and J. S. Shaub, "Analysis of Seismic Surface Waves Using PDP-15 Interactive Graphics," *Proc. Intl. Symp. on Computer Aided Seismic Analysis and Discrimination*, Falmouth, Massachusetts, 16-17 June 1977, pp. 15-25.
10. E. L. Shirokova, "A Detailed Study of the Stresses and Fault Planes at Earthquake Foci of Central Asia," *Phys. Solid Earth* **11**, 707-717 (1974).
11. S. Das and J. R. Fialson, "On the Tectonics of Asia," *Earth Planet. Sci. Lett.* **28**, 241-253 (1975), DDC AD-A024180/2.
12. P. Molnar, T. J. Fitch, and F. T. Wu, "Fault Plane Solutions of Shallow Earthquakes and Contemporary Tectonics in Asia," *Earth Planet. Sci. Lett.* **19**, 101-112 (1973).
13. T.-L. Teng, "Surface Wave Studies on Crustal and Mantle Structure of China," Technique Report 1974-2, University of Southern California Geophysical Laboratory (1974).
14. M. Barazangi and B. Isacks, "Lateral Variations of Seismic Wave Attenuation in the Upper Mantle Above the Inclined Earthquake Zone of the Tonga Island Arc: Deep Anomaly in the Upper Mantle," *J. Geophys. Res.* **76**, 8493-8516 (1971).
15. J. Dubois, "Propagation of P Waves and Rayleigh Waves in Melanesia: Structural Implications," *J. Geophys. Res.* **76**, 7217-7240 (1971).
16. A. S. Furumoto, J. P. Webb, M. E. O'egard, and D. M. Hussong, "Seismic Studies on the Ontong Java Plateau, 1970," *Tectonophysics* **34**, 71-90 (1976).
17. J. Dorman, M. Ewing, and J. Oliver, "Study of Shear Velocity Distribution in the Upper Mantle by Mantle Rayleigh Waves," *Bull. Seismol. Soc. Am.* **50**, 87-115 (1960).
18. H. Kanamori and K. Abe, "Deep Structure of Island Arcs as Revealed by Surface Waves," *Bull. Earthquake Res. Inst.* **46**, 1001-1025 (1968).
19. T. Santo and Y. Sato, "World Wide Survey of the Regional Characteristics of Group Velocity Dispersion of Rayleigh Waves," *Bull. Earthquake Res. Inst.* **44**, 939-964 (1966).

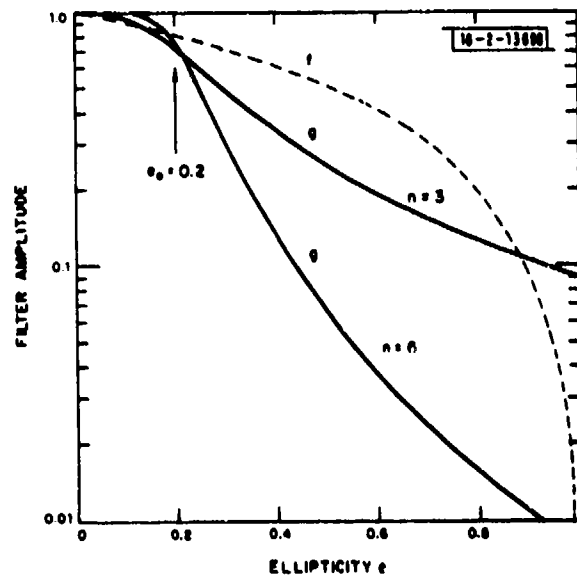


Fig. I-1. Filter response of ellipticity filters  $f = 1 - e$  and  $g = [1 + (e/e_0)^n]^{-1/2}$  described in text.

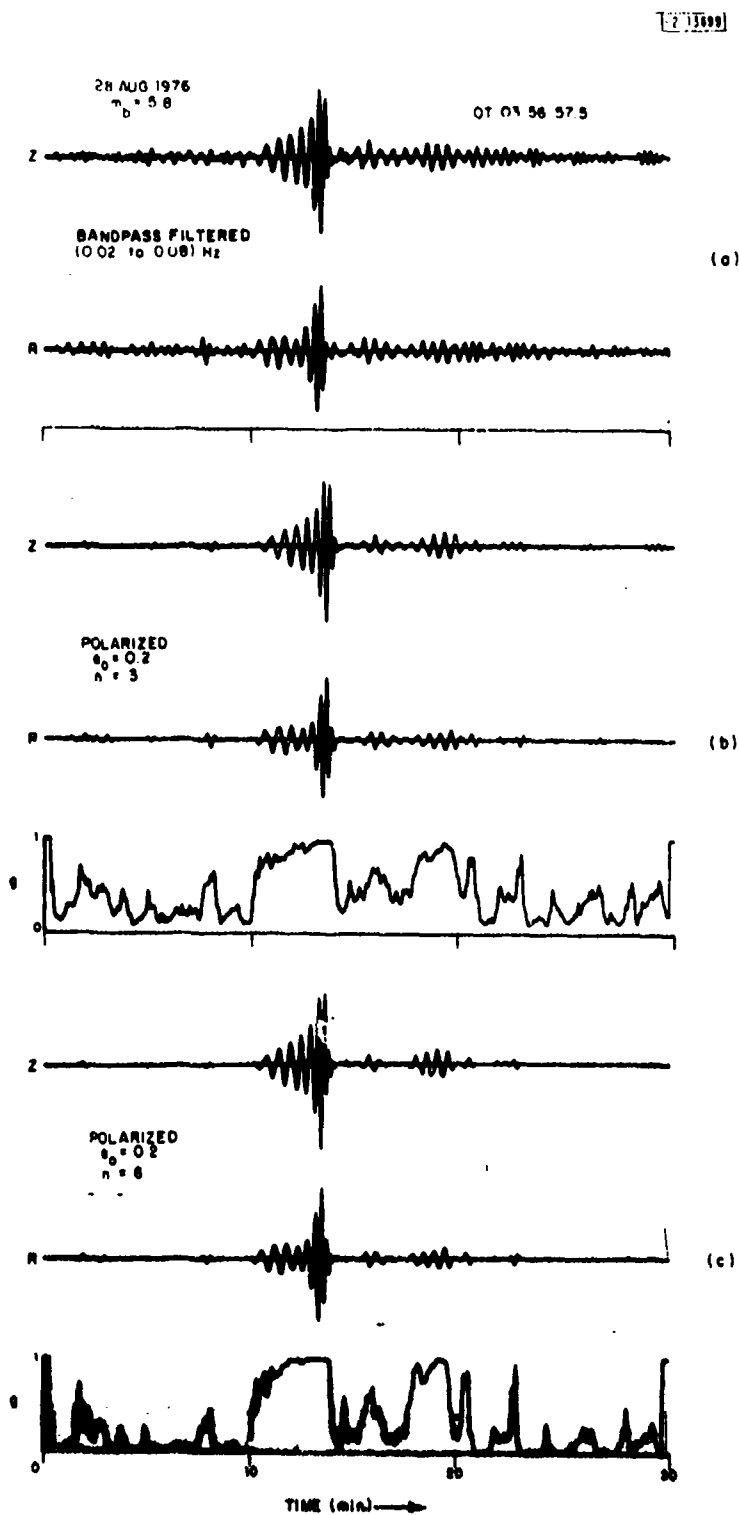


Fig. 1-2. (a) Rotated Z and R LP components from an Eastern Kazakh explosion  $m_b$  of 5.8 recorded at MAIO SRO. (b) Traces of (a) after polarization using a 3-pole ellipticity filter  $g$ . (c) Traces of (a) after using a 6-pole ellipticity filter  $g$ .

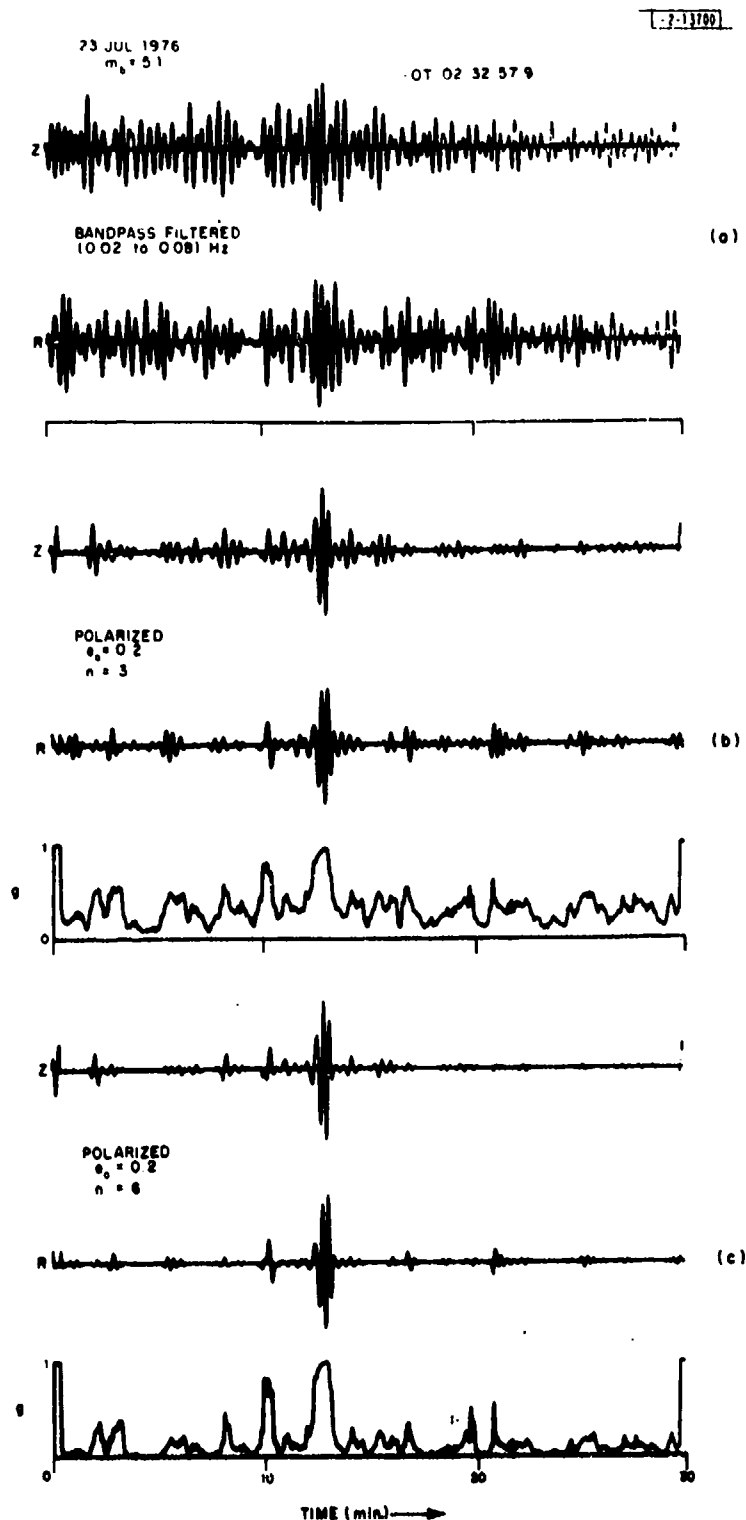


Fig.1-3. (a) Rotated Z and R LP components from an Eastern Kazakh explosion  $m_b$  of 5.1 obscured by an earthquake coda. (b) Traces of (a) after polarization using a 3-pole ellipticity filter  $g$ . (c) Traces of (a) after using a 6-pole ellipticity filter  $g$ .

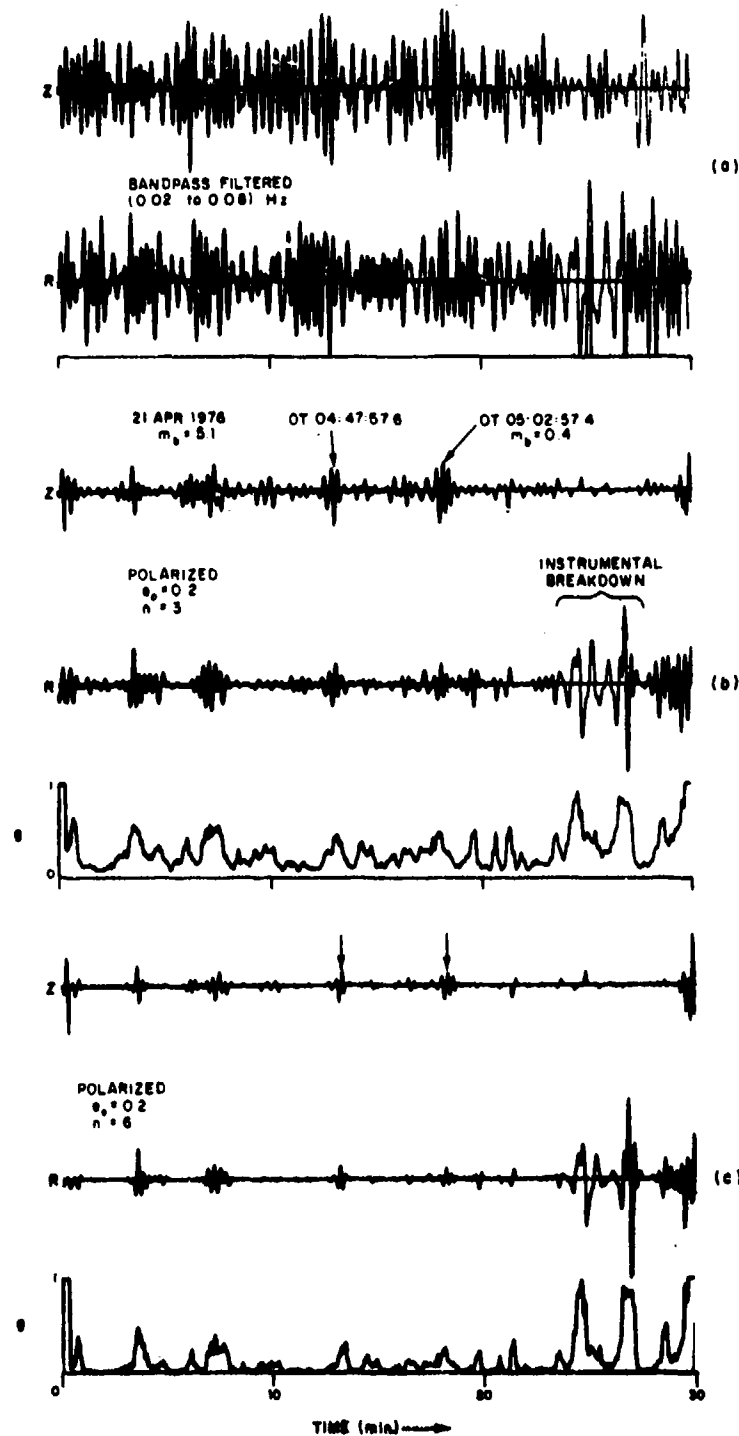


Fig. I-4. (a) Rotated Z and R LP components from two Eastern Kazakh explosions  $m_b$  of 5.1 and 5.3 which occurred 5 min. apart. They are obscured by an earthquake coda. (b) Traces of (a) after polarization using a 3-pole ellipticity filter  $g$ . (c) Traces of (a) after using a 6-pole ellipticity filter  $g$ .

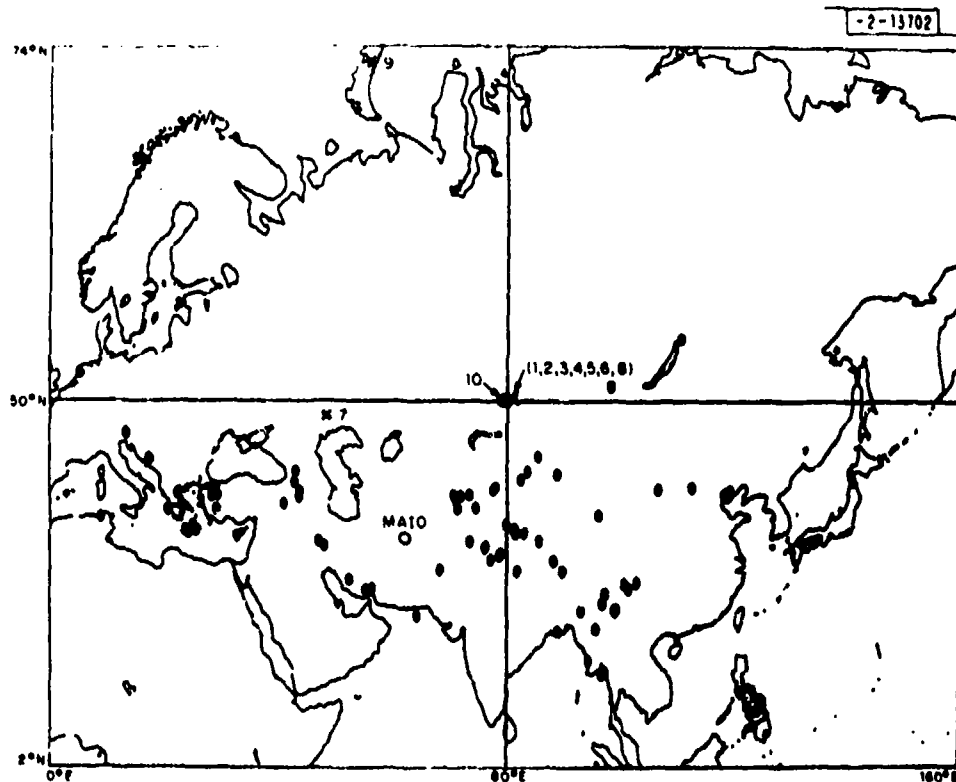


Fig. I-5. Locations of earthquake (O) and explosion (X) sources used in this study. Numbers correspond to those in Table I-1.

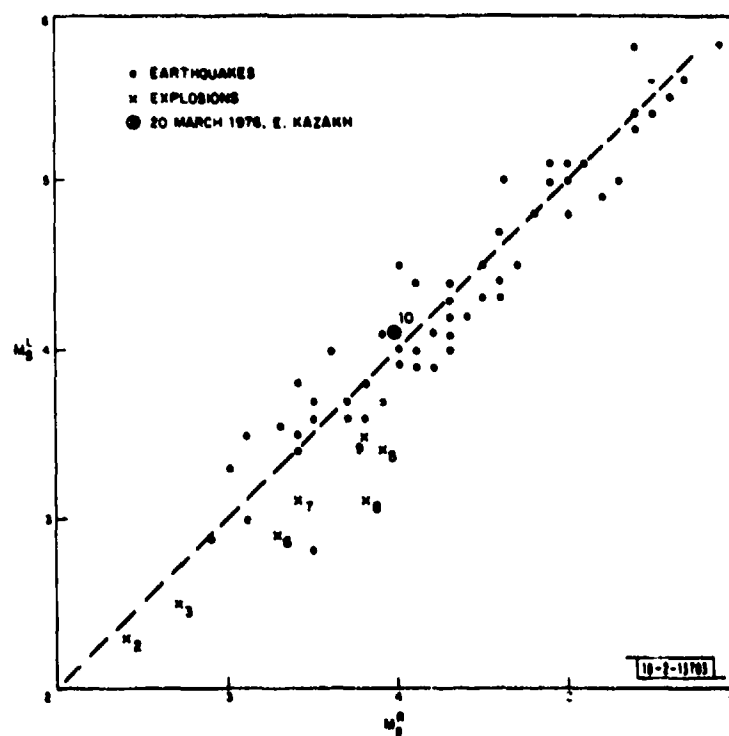


Fig. I-6.  $M_S$  measured from vertical Rayleigh waves ( $M_S^R$ ) vs that measured from Love waves ( $M_S^L$ ).

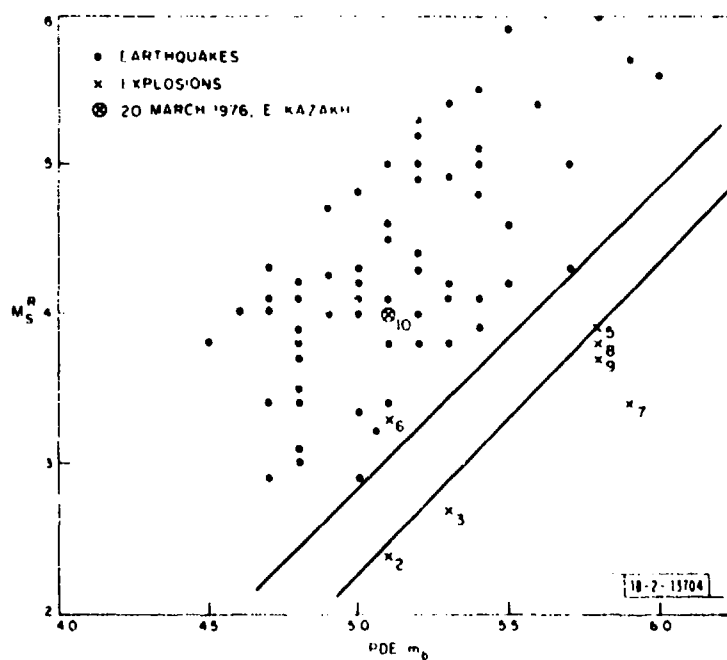


Fig. 1-7.  $M_S^R$  vs  $m_b$  for data of Fig. 1-6.

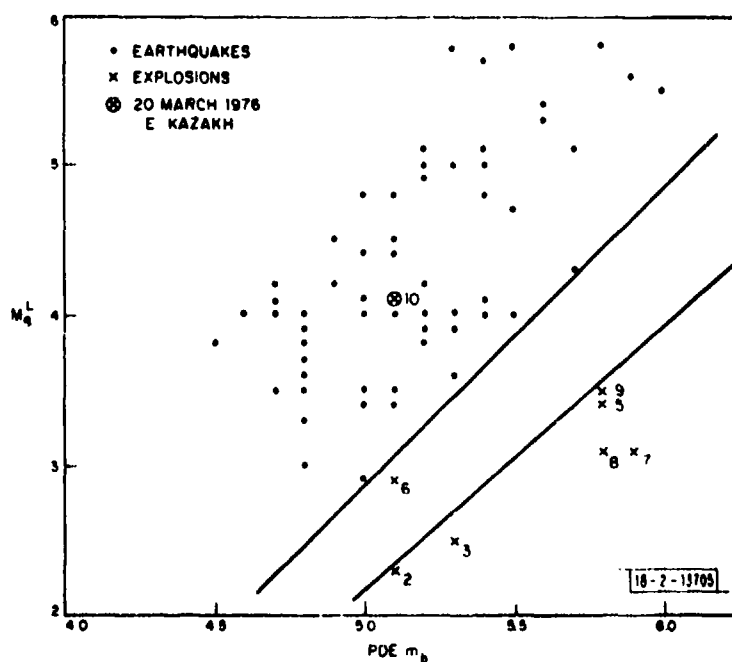


Fig. 1-8.  $M_S^L$  vs  $m_b$  for data of Fig. 1-6.



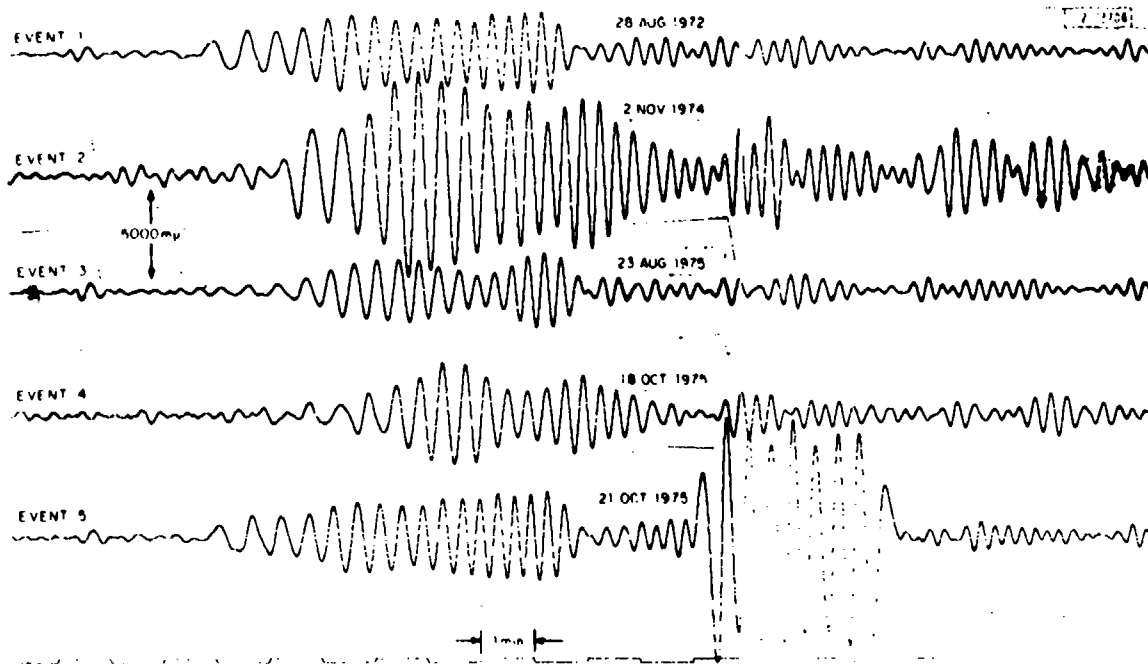


Fig. 1-9. ALPA center sensor seismograms from five events used in this investigation.

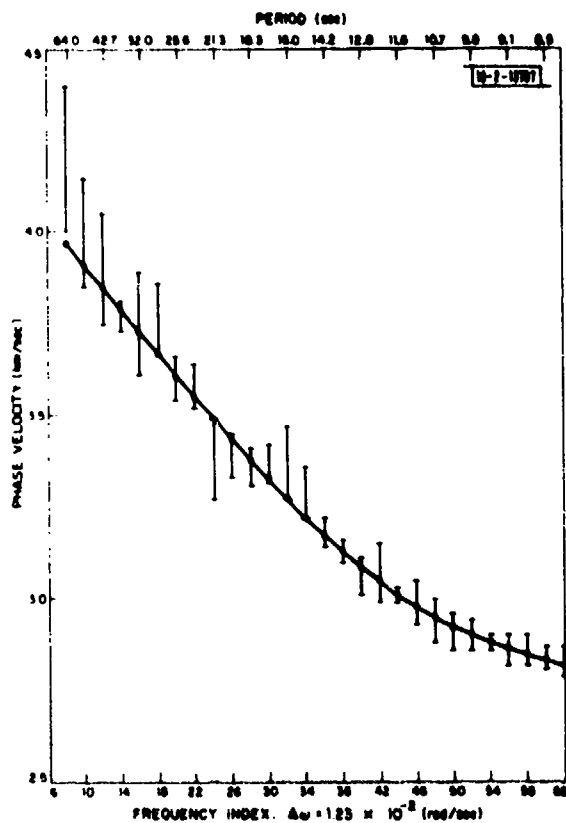


Fig. 1-10. Phase velocity dispersion data, estimated errors, and dispersion from best-fitting model.

Fig. 1-11. Best-fitting structural model for Novaya Zemlya.

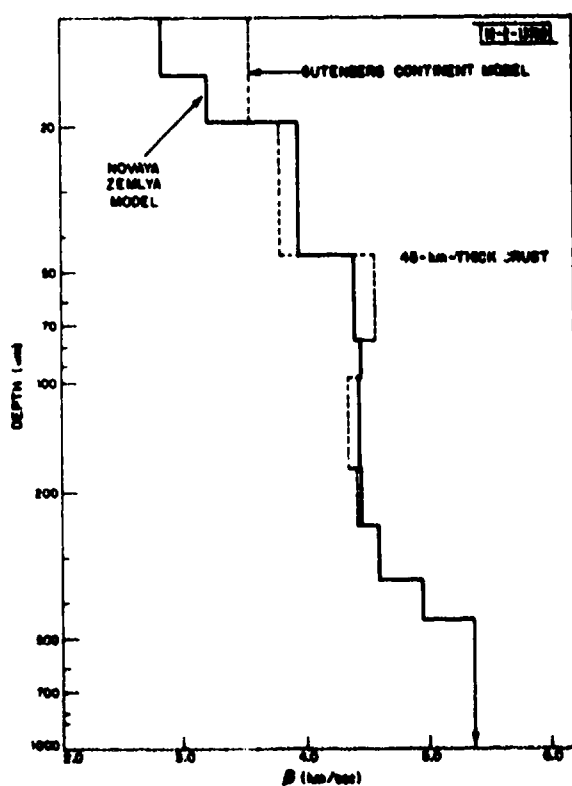
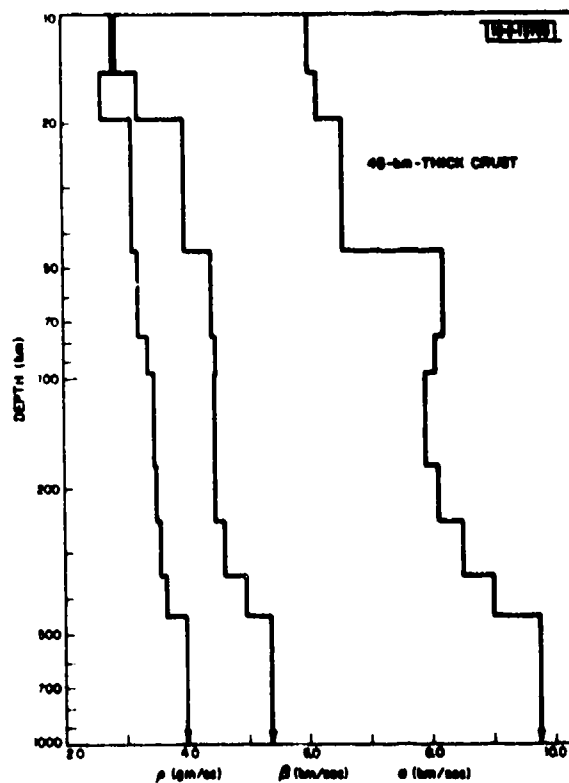


Fig. 1-12. Shear-wave-velocity profiles from Novaya Zemlya model and Gutenberg Continent starting model.

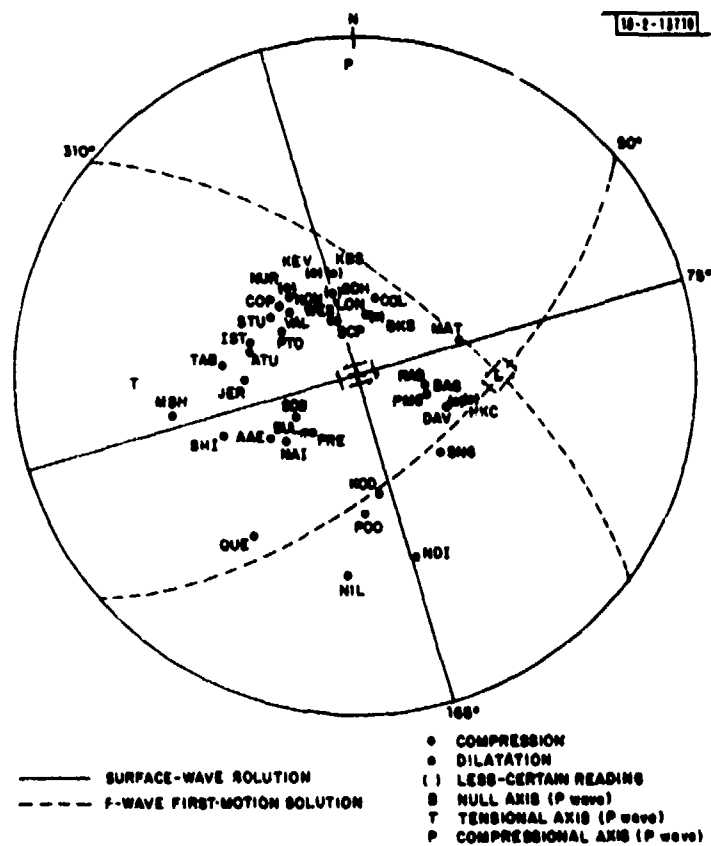


Fig. I-13. Comparison of surface-wave solution with P first-motion solution for event 1.



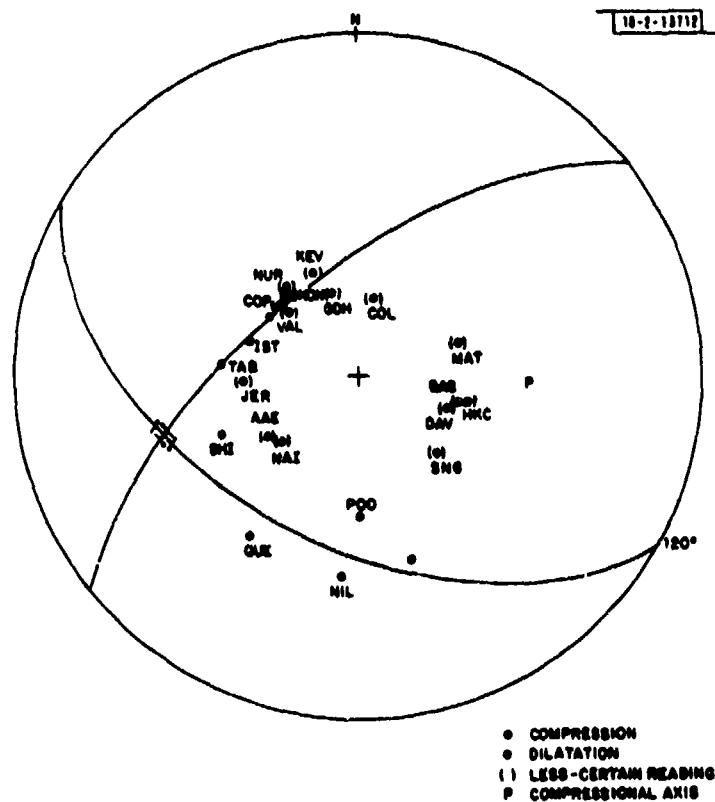


Fig. I-15. Comparison of surface-wave solution with P first-motion data for event 3.

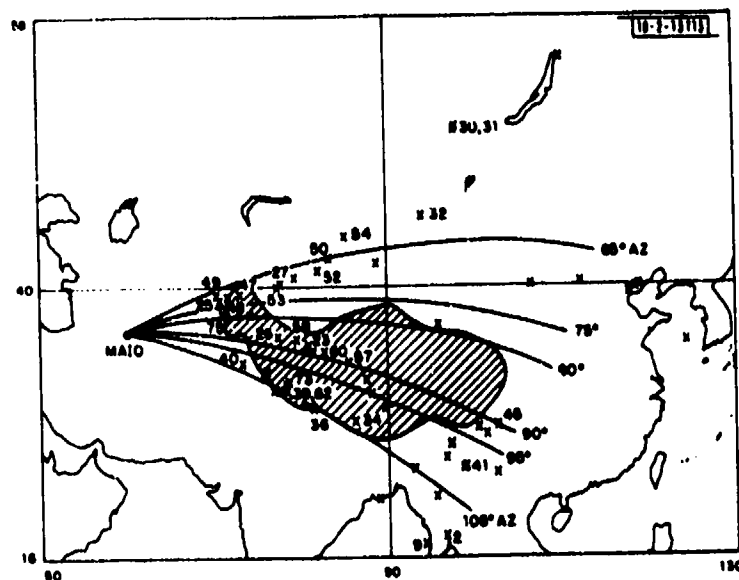


Fig.1-16. Locations of events recorded at MAIO. Great-circle paths and outline of high-altitude (>3000 m) region are shown.

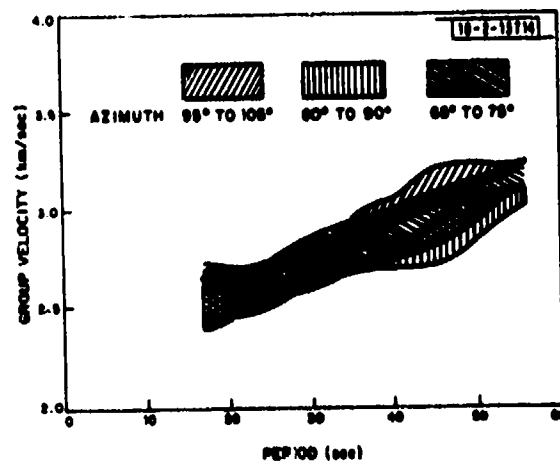


Fig.1-17. Envelopes of Rayleigh-wave group velocities for various azimuths.

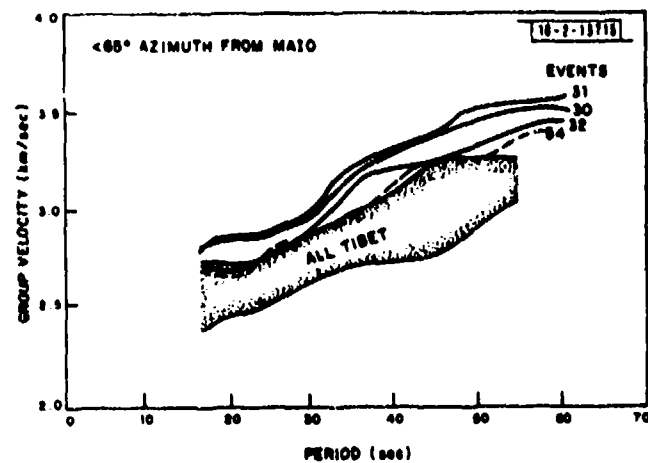


Fig.1-18. Group velocities to events at azimuths  $<65^\circ$  (Mongolia, N. Sinkiang). Also shown is a summary of Tibetan group velocities (from Fig.1-17).

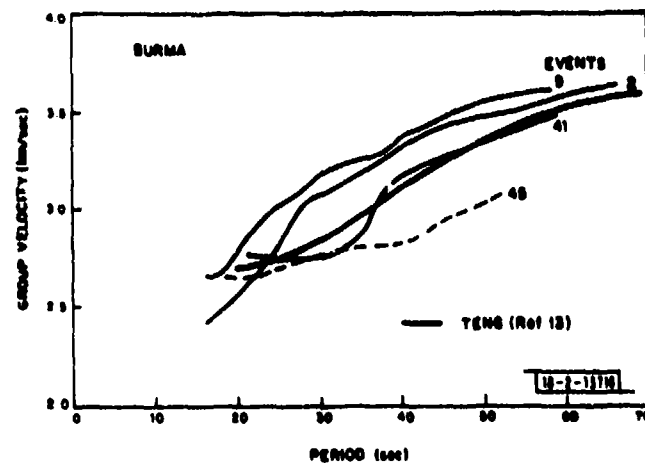


Fig.1-19. Group velocities to events in Burma and Szechwan, together with theoretical dispersion for Tibet given by Teng.

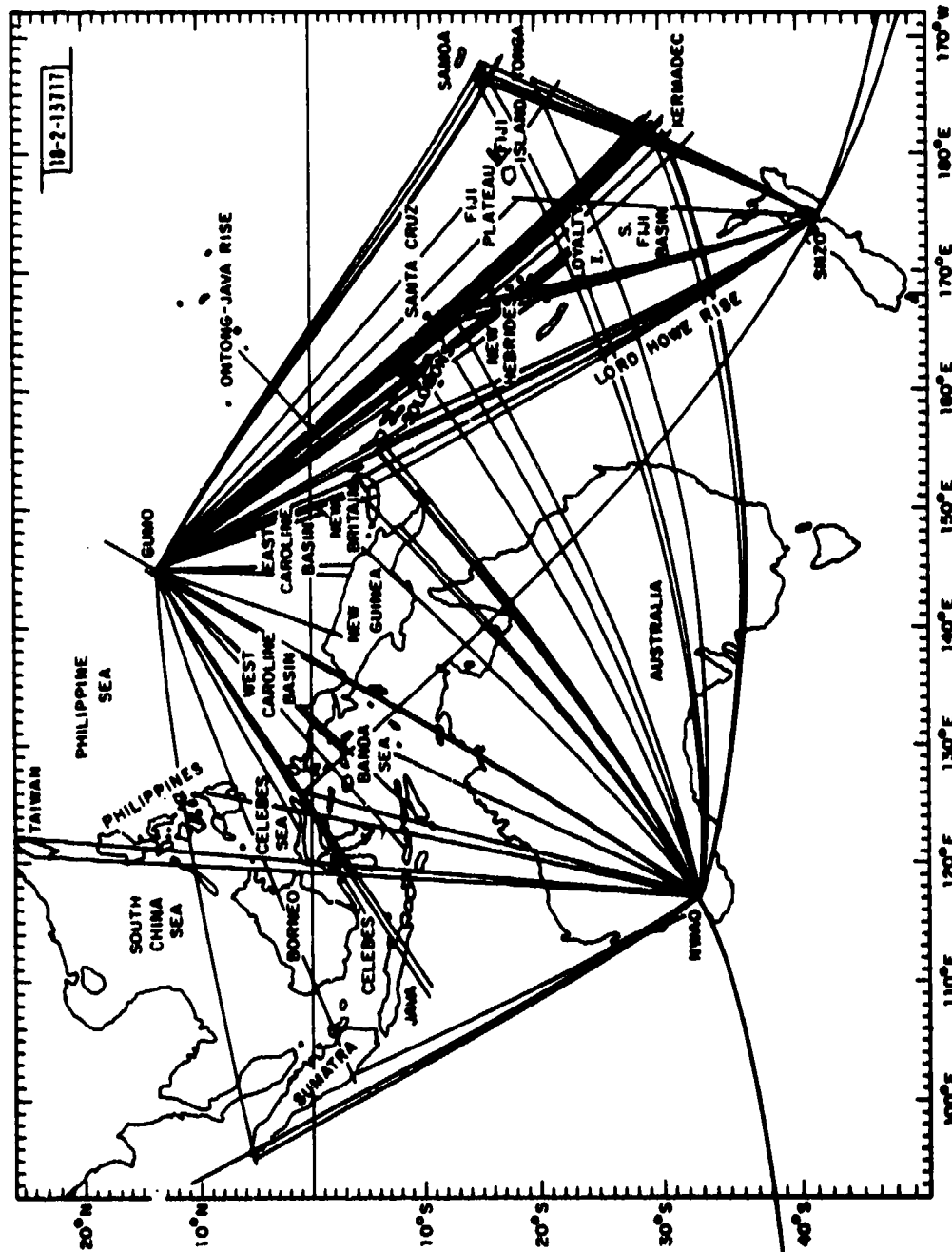


Fig. I-20. Paths for which surface-wave-dispersion characteristics have been obtained.



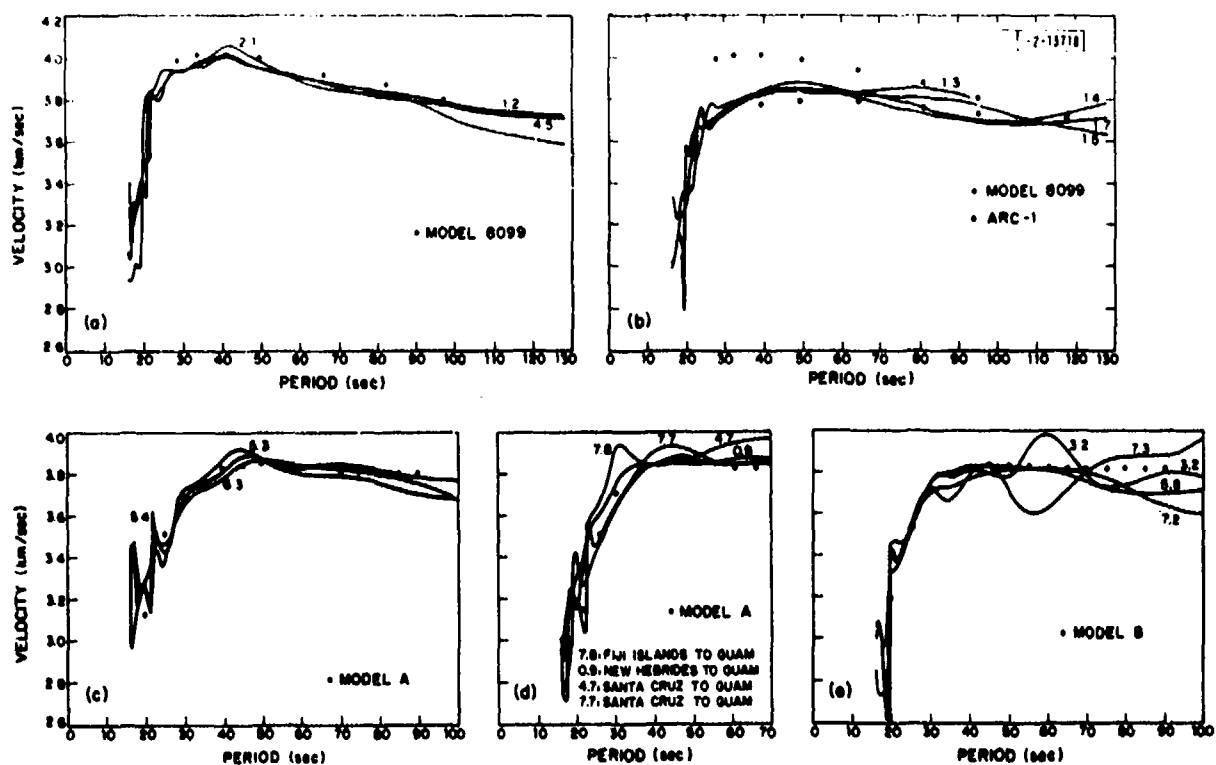


Fig. I-21. Dispersion curves for several paths to GUMO: (a) from Samoa, (b) from Kermadec, (c) from Loyalty Islands, (d) from Fiji Plateau, and (e) from Solomon Islands.

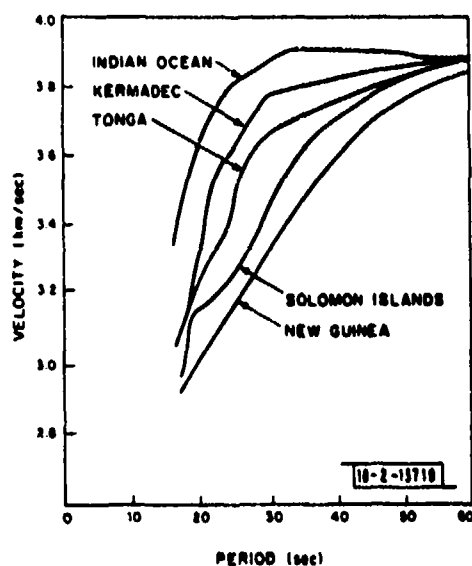


Fig. I-22. Averaged dispersion curves for paths from diverse regions to NWA0.

## II. SEISMIC SCALING AND BODY-WAVE MAGNITUDE $m_b$

### A. MOMENTS AND STRESS DROPS FOR THE RAT ISLAND SEQUENCE OF 1965

In a previous study of the Rat Island sequence of 1965 (Ref. 1), it was shown that the trend of  $\log(A/T)$  or  $m_b$  vs pulse-period  $T$ , reported by VELA stations, favored an  $\omega$ -cube displacement model suggested by Savage<sup>2</sup> rather than  $\omega$ -squared sources such as Brune's model<sup>3,4</sup> if geometrical similarity was assumed for all earthquakes. This implied constant stress for all earthquakes in the model with amplitude variations being controlled by the DC spectral level which was set equal to  $f_0^{-3}$ , the inverse corner frequency cubed.

We have now used the empirical scaling of the synthetic data to estimate DC level of the source spectra, and from that the moment and stress drop of the Rat Island data.

Figure II-1(a-b) shows the scatter of the Rat Island data used to define the trend of  $m_b$  vs period  $T$ . Of the 868 aftershocks selected, a subset of 245 events was reported at all five VELA stations. The mean and standard deviation of both  $m_b$  and  $T$  for each event are shown in Fig. II-1(a). We see that the trend of  $m_b$  vs  $T$  is well defined for the shorter periods, but seems to deteriorate for periods greater than 1.2 sec.

To quantify this trend, a weighted linear regression line was fit to the data using an iterative technique described by York.<sup>5</sup> This method allows individual weighting of every data point in both coordinates. Following York's suggestion, we chose weights which are reciprocals of the data variance in each coordinate. The resulting least-squares line is

$$m_b = (3.24 \pm 0.08) + (1.32 \pm 0.09)T$$

which is shown in Fig. II-1(a).

Figure II-1(b) contains a histogram of average periods for this data set grouped in bins 0.1 sec wide. The distribution of periods is asymmetric, peaked at 0.8 sec with 90 percent of the data falling in the range 0.6 to 1.3 sec.

Figure II-2 shows the synthetic curves of  $m_b$  vs  $T$  for the  $\omega$ -cube model of Savage<sup>2</sup> as a function of corner frequency  $f_0$  and attenuation parameter  $t^*$ . The regression line of Fig. II-1(a) is displayed as a pair of solid lines shifted by 0.5  $m_b$  unit to show the effect of shifting the theoretical curves by the same amount. The data and synthetic trends are not perfectly matched, but are much more similar than when  $\omega$ -square source models are used.<sup>1</sup> The variation in  $t^*$  for this empirical fit of model to data is from  $\sim 0.25 \lesssim t^* \lesssim 0.75$ .

We shall pick a tabulated point on the synthetic  $m_b$  curves in Fig. II-2 and first obtain the DC spectral level, from which moment can be estimated. Under the assumptions of our model, the stress drop is constant for all points along each solid curve as  $f_0$  varies.

The synthetic point in Fig. II-2 with a corner frequency  $f_0 = 1$  and  $t^* = 0.5$  has an empirical  $m_b$  of 4.6 on the left-hand scale and an observed pulse period  $T = 0.90$  sec. This point is a little above the lower Rat Island data trend. Using the Gutenberg  $Q$  factor for a distance of  $60^\circ$ , which is about the average VELA station distance, we obtain  $\log(A/T) \approx 1.0$  or

$$A/T \approx 10 \text{ m}\mu/\text{sec}.$$

This value is 86 times the unscaled synthetic  $A/T$  value which had a DC level set equal to  $f_0^{-3} = 1$ . Thus, the DC spectral level of the empirically scaled displacement source in Fig. II-2 is

$$\Omega_0 = 86 \times 10^{-7} \text{ cm-sec}.$$

Hanks and Wyss<sup>6</sup> proposed an adaptation for P waves of Keilis-Borok's formula for seismic moment which is

$$M_0 = \rho_0 2\pi \alpha^3 R/r$$

where  $\rho$  = density,  $\alpha$  = P-wave velocity in the source region,  $R$  is the geometric divergence correction, and  $r$  is the radiation pattern. This includes a factor of 0.5 to account for the free surface reflection at the seismometer. Hanks and Wyss note that SP amplitudes are not well correlated with radiation patterns based on LP P waves, and we have no fault-plane solutions for these small events. Under this circumstance, we set  $r = 1$  although  $r$  is probably  $< 1$  based on the fault-plane solutions for large shocks of the Rat Island sequence obtained by Stauder.<sup>7</sup>

Taking as typical values  $\rho = 3.0 \text{ g/cm}^3$ ,  $\alpha = 6.0 \text{ km/sec}$ , and  $R = 1.9 \times 10^4 \text{ km}$  at  $60^\circ$  (Ref. 8), we obtain for the moment

$$M_0 = 6.65 \times 10^{22} \text{ dyn-cm} \quad (\text{II-1})$$

Using this moment and the corner frequency  $f_0 = 1$ , we can evaluate the stress drop  $\Delta\sigma$  for this family of curves by Brune's formula,<sup>6</sup> i.e.,

$$\Delta\sigma = \frac{7}{16} \frac{M_0}{a^3} \text{ dyn-cm}^{-2} \quad (\text{II-2})$$

where  $a$  is the radius of the circular source area given by

$$a = \frac{2.34\alpha}{2\pi f_0} \text{ km} \quad (\text{II-3})$$

Substituting Eqs. (II-3) and (II-1) into (II-2), we obtain the stress drop

$$\Delta\sigma = 25.4 \text{ bars} \quad (\text{II-4})$$

This value of stress drop inferred for the Rat Island earthquakes with  $4 \lesssim m_b \lesssim 5$  agrees with stress drops estimated for larger Aleutian earthquakes using spectral techniques. Wyss *et al.*<sup>9</sup> used LP P-wave spectra to calculate stress drops of 10 to 47 bars for three Aleutian earthquakes,  $m_b > 6.0$  near Amchitka Islands. The moment value in Eq. (II-1) is quite reasonable for  $m_b \sim 4.6$  earthquakes as extrapolated down from moments of larger  $m_b$  earthquakes,<sup>8</sup> or inferred from moment vs  $m_L$  curves for local earthquakes.<sup>6</sup>

Therefore, it appears that the use of simple time-domain models can yield reasonable moments and stress drops for moderate-sized teleseismic earthquakes, without resorting to LP spectral analysis. It is fortunate that DC levels inferred from SP amplitudes seem to agree with actual LP measurements. However, excellent bulletin data are required for many events from a single-source region, in order to define a reliable trend of amplitudes vs periods. Statistically, any single earthquake may, in fact, not fit the average trend at all.

C. W. Frasier  
R. G. North

## B. INCORRECT SEISMIC SCALING FROM $m_b$

Body-wave magnitude ( $m_b$ ) is often used to indicate the spectral level of earthquake sources at 1 Hz (Refs. 11 and 12). The basic assumption is that an  $m_b$  difference of 1.0 unit implies a factor of 10 between the spectral levels of two similar earthquakes at a 1-sec period.

For stochastic source models,<sup>11</sup> this assumption is probably wrong because the power level at a single frequency cannot be calculated from a single amplitude measurement of a complex seismogram. For deterministic source models, we can clearly demonstrate that  $m_b$  is not a measurement of 1-Hz energy and that a significant error, which depends on the earthquake source function and attenuation, results from such an interpretation.

To demonstrate this, synthetic records for two seismic source models were calculated as recorded by four SP recording systems. Figure II-3 shows the displacement response, normalized to 1 at 1 Hz, of four SP recording systems - WWSSN, VELA, SRO, and LASA. The SRO response was calculated from the system response described in Sec. IV-A of this SATS. Both SRO and LASA systems are digitally recorded with anti-alias filters and no galvanometer, whereas the VELA and WWSSN systems have coupled seismometer and galvanometer combinations.<sup>13,14</sup>

Figure II-4 displays the impulse displacement response of the four systems, including a small amount of causal earth attenuation<sup>15</sup>  $t^* = T/\bar{Q} = 0.1$ , where  $T$  equals the travel time and  $\bar{Q}$  the average quality factor for the teleseismic path. The ripple in the coda of LASA and SRO responses is due to the sharp cutoff of the anti-alias filter in each system, the SRO filter being especially sharp. One also sees a large group delay for the SRO response (see Sec. IV-A).

The impulse responses in Fig. II-4 were further attenuated and convolved with an  $\omega$ -square source by Brune<sup>1</sup> and an  $\omega$ -cube source by Savage<sup>1</sup> to produce a suite of synthetic records for each recording system. Figure II-5 displays synthetic records for the  $\omega$ -square source with a corner frequency of  $f_0 = 0.5$  Hz and  $t^* = 0.5$ . Although the system characteristics in Figs. II-3 and II-4 vary considerably, the overwhelming effect of earth attenuation and source decay above the corner frequency produces similar-looking records for all four seismometer systems.

Synthetic records were calculated for a range of corner frequencies  $f_0$  from  $2^3 = 8$  Hz to  $2^{-9} = 0.00391$  Hz for each source model assuming two  $t^*$  values, 0.5 and 1.0. Relative magnitudes were computed for each seismogram by calculating  $\log(A/T)$  where  $A$  is peak amplitude and  $T$  is peak period, and  $A$  is corrected for seismometer response at period  $T$ . Due to observed dispersion in the waveforms and ambiguities in the choice of peaks used for  $A$  and  $T$  by an analyst,  $A$  was measured as the peak value of the envelope of the trace, and  $T$  was calculated from the instantaneous frequency  $f = 1/T$  at that envelope peak. This method produces magnitudes very close to the values obtained by an analyst, and produces more continuous  $T$  measurements.

In Fig. II-6(a), the difference between  $\log(A/T)$  and  $\log$  of the source at 1 Hz is displayed for the Brune source as a function of corner frequency  $f_0$ . The  $\log(A/T)$  values are averages of all four recording systems. The standard deviations of the  $\log(A/T)$  distribution is very small ( $\leq 0.03$ ) for all corner frequencies, so that relative magnitudes are practically identical for all four recording systems in spite of the variations in displacement response. Figure II-6(b) shows similar plots for the  $\omega$ -cube Savage source.

Although the extremes of corner frequencies are outside the range expected for teleseismic data, the region of most rapid change in the curves is between 2.0 and 0.0625 Hz, which includes most teleseismically recorded magnitudes. Bars in Figs. II-6(a) and (b) indicate the range of corner frequencies expected for  $m_b$  4.5 and 6.0 as the stress drop varies from 1 to 100 bars for each magnitude, calculated by North and Frasier (see Sec. C below). Thus, the rapid change in bias of  $\log(A/T)$  about  $\log$  of the source at 1 Hz cannot be adequately removed by a constant shift of  $\log(A/T)$  such as the Gutenberg  $Q$  factor.

The basic cause of this non-constant bias is the variation in observed periods as a function of corner frequency. Figures II-7(a) and (b) show the average pulse period for each source for the two  $t^*$  values. The periods are averaged over the four recording systems, and the period distributions have standard deviations of  $\lesssim 0.08$  sec for the Brune source at all corner frequencies. For the Savage source, the period distributions have standard deviations  $\leq 0.13$  sec for  $t^* = 0.5$ , and  $\leq 0.20$  sec for  $t^* = 1.0$ , the largest deviations occurring at corner frequencies  $\leq 0.0625$ .

Using the observed period, we can calculate the expected frequency-domain amplitude at that period by taking the product of source function and attenuation and dividing by  $T$ . A comparison of this frequency-domain estimate of  $\log(A/T)$  with the observed  $\log(A/T)$  on the synthetics is shown in Figs. II-8(a) and (b). The agreement is nearly perfect and indicates that observed time-domain magnitudes for deterministic sources predict almost exactly the expected spectral amplitudes at the pulse period if the source function and attenuation are included.

From this synthetic record experiment, it is clear that  $m_b$  variations cannot be used to infer seismic source scaling at 1 Hz without detailed knowledge of the source model, including corner frequency and earth attenuation along the teleseismic path.

C. W. Frasier

### C. $m_b$ -FREQUENCY RELATIONS FROM SEISMIC SCALING LAWS

In an earlier attempt<sup>1</sup> to reproduce a linear trend of  $\log(A/T)$  vs  $T$  (where  $A$  is the maximum peak-to-peak amplitude, and  $T$  the dominant period) of  $P$  waves observed for aftershocks of the Rat Island's earthquake of 1965 we have generated synthetic seismograms for a range of corner frequencies  $f_0$  for the Brune ( $\omega^2$  far-field spectral decay below the corner frequency) and Savage ( $\omega^3$ ) source models. We found that the data trend of  $\log(A/T)$  vs  $T$  was best fitted by the  $\omega^3$  model with  $t^* = 0.5$ . An inherent assumption in the generation of the synthetic seismograms was that of geometrical similarity, implying constant stress drop, i.e.,

$$\log M_0 = -3 \log f_0 + C \quad (M_0 = \text{seismic moment}) \quad (\text{II-5})$$

where the constant  $C$  depends upon the stress drop  $\Delta\sigma$ .

Figure II-9 shows the variation of  $m_b$  with  $\log(f_0)$  for the  $\omega^2$  and  $\omega^3$  source models, for  $t^* = 0.5$  and  $1.0$ . For a given corner frequency  $f_0$ , the difference in  $m_b$  given by the two values of  $t^*$  is  $\sim 0.7$  unit at  $f_0 = 8$  Hz, decreasing to  $< 0.2$  unit at the highest values of  $f_0$ . This variation is caused by the increase in dominant period of the  $P$  wave as  $f_0$  decreases. It can be seen, as remarked previously,<sup>1</sup> that the  $\omega^2$  model predicts higher values of  $m_b$  for a given  $f_0$  than the  $\omega^3$  model for  $f_0 < 0.5$  Hz.

We show elsewhere (see Sec. B above) that the stress drop implied by the fit of the Rat Island data to the  $\omega^2$  model is 25 bars, derived by correcting the spectrum for a source with  $f_0 = 1$  Hz back to the source to obtain a moment of  $6.7 \times 10^{22}$  dyn-cm. Using this result, we may compute the precise form of  $C(\Delta\sigma)$  in Eq. (II-5).

By combining Fig. II-9 and relation (II-5), we may obtain the variation of  $\log(M_0)$  with  $m_b$  for the  $\omega^2$  and  $\omega^3$  models for any particular values of  $\Delta\sigma$  and  $t^*$ . Figure II-10 shows moment as a function of  $m_b$  for  $\Delta\sigma = 10$  bars and  $t^* = 0.5$ . Different values of stress drop  $\Delta\sigma$  merely shift the curves up or down; changes in  $t^*$  cause variations in  $m_b$  for a given  $M_0$  which are small for  $m_b > 5.0$ .

It can be seen from Fig. II-10 that the most striking difference between the  $\omega^2$  and  $\omega^3$  model is that the latter predicts an upper limit to  $m_b \sim 6.0$ , whereas the former predicts that  $m_b$  will increase with moment without limit. For the smallest stress drop we have considered (1 bar), the  $\omega^2$  model predicts an  $m_b \sim 7.6$  for  $M_0 = 10^{29}$  dyn-cm. Such large values of  $m_b$  have never been observed, even though events of this moment appear to occur about once every 1 to 2 years.<sup>16</sup>

A considerably more-sophisticated source model than the simple ones we have considered, incorporating not only the effects of source dimension but also fault width and rise time, has been described by Geller.<sup>17</sup> The high-frequency asymptote of far-field spectrum produced by this model is  $\omega^{-3}$  decay, but it also includes regions of  $\omega^{-2}$  and  $\omega^{-1}$  decay. From the relations given by Geller between  $M_0$  and  $M_s$ , and  $M_s$  and  $m_b$ , we may deduce the variation of  $M_0$  with  $m_b$ , and this also is shown in Fig. II-10. Geller assumed that  $m_b$  is directly related to the spectral density at 1 Hz; this is not strictly correct, as he mentions and as is also shown elsewhere in this report (Sec. B above). However, it can be seen that the variation of  $\log(M_0)$  with  $m_b$  that he obtains is very similar to that produced by the much simpler  $\omega^3$  model we have considered, and also implies an upper limit to  $m_b$  of  $\sim 6.0$ .

We have no data on the variation of  $M_0$  with  $m_b$  against which to test the model predictions, but there does exist a large amount of data on the rate of occurrence of events of a particular  $m_b$  (known as the  $m_b$ -frequency curve). It has also been shown<sup>16</sup> that for  $\log M_0 > 25$ , the  $M_0$ -frequency curve is remarkably linear and given by

$$\log N = 17.47 - 0.61 \log M_0 \quad . \quad (II-6)$$

Evidence that this linear relation persists for smaller events is provided by data from Southern California<sup>18</sup> where

$$\log M_0 = 1.5 M_L + 16.0 \quad , \quad \text{for } 20 < \log M_0 < 25$$

( $M_L$  = local magnitude) and the  $M_L$ -frequency curve is remarkably linear for  $1 < M_L < 7$  with a slope very close to unity.<sup>19</sup> Thus, for Southern California, at least,

$$\log N = \text{constant} - 0.67 \log M_0 \quad . \quad (II-7)$$

The slopes of Eqs. (II-6) and (II-7) are very close, and we therefore assume that Eq. (II-7) holds for  $20 < \log(M_0) < 31$ .

By combining Fig. II-10 with relation (II-6), we may obtain  $m_b$ -frequency curves for the source models we have considered. Those for  $\Delta\sigma = 50$  bars and  $t^* = 0.5$  are shown in Fig. II-11. Changes in  $\Delta\sigma$  will shift the curves up or down; changes in  $t^*$  produce appreciable differences only for  $m_b < 5.0$ . Also shown on this figure is an  $m_b$ -frequency curve derived from the ISC dataset<sup>20</sup> for 1964 to 1973. Below  $m_b \sim 5$ , the shape of this curve is primarily dictated by network detection characteristics and bears no known relation to the actual occurrence of events with a particular  $m_b$ . It can be seen that the data lie between the curves produced by the  $\omega^3$  and  $\omega^2$  models. No possible combinations of stress drop and/or  $t^*$  can reproduce the ISC data curve. Our theoretical curves are, of course, critically dependent upon the slope of Eq. (II-6), but unreasonably large changes in the slope are required to make either model match the data. It is interesting to note that an  $\omega^{5/2}$  scaling law would produce an  $m_b$ -frequency curve lying between those for  $\omega^2$  and  $\omega^3$ ; such a scaling law has, in fact, been suggested in the literature.<sup>21,22</sup>

It can be seen that, provided a linear relationship of the form Eq. (II-6) holds, none of the scaling laws mentioned here ( $\omega^2$ ,  $\omega^3$ ,  $\omega^{5/2}$ , or Geller's model) predicts that the  $m_b$ -frequency

curve is linear except at very small magnitudes. Thus, "b-values" are essentially meaningless except over very limited magnitude ranges. M. Wyss has claimed<sup>23</sup> that low b-values indicate high stress in the source region and vice versa, assuming a relation of the form of Eq. (II-6). Our results show that the only effect of changing stress drop is to move the  $m_b$ -frequency curve up or down; for any one of the source models postulated, the shape of the curve is completely independent of stress drop.

R. G. North  
C. W. Frasier

#### D. SATURATION OF THE $m_b$ SCALE

The study described above demonstrates that information about the seismic source can be obtained from data on the saturation of the  $m_b$  scale at large magnitudes. The only empirical data of this kind that are available are contained in global earthquake catalogs such as the Bulletin of the International Seismological Center (ISC), and it is well known that there are problems in assigning  $m_b$  values to large events.

The investigation of saturation of the  $m_b$  scale involves estimating the shape of the frequency magnitude relationship for large events. Previous studies<sup>1</sup> indicated that network estimates of  $m_b$  for large events will be affected by the detection probability curves for individual stations in the network, which will fall off due to instrument saturation or clipping. The result of clipping will be to introduce a negative bias into network  $m_b$  estimates for large events, in exactly the same way that detection thresholds introduce positive biases at low  $m_b$  values. The effect of clipping is therefore in the same direction as  $m_b$  saturation due to the seismic source, and it is not easy to separate these two effects.

If the  $m_b$  values listed in the ISC Bulletin are taken at face value, saturation appears to occur in the vicinity of  $m_b = 6.5$ . Figure II-12(a) shows the frequency- $m_b$  values for 1966-70, for all regions of the world. Notice the large apparent "b-value," which is somewhat subjective but which might be as large as 1.5. Selection of a smaller, more well-controlled network of 28 stations with good reporting characteristics leads to essentially the same result [Fig. II-12(b)]. Inclusion of station biases, as determined by North,<sup>20</sup> does not change the curve significantly.

A very substantial change is observed, however, if the VELA arrays located in the Western U. S. are used alone. Figure II-13 shows frequency- $m_b$  plots for the four arrays BMO, TFO, UBO, and WMO, with the station biases included. The agreement between stations is excellent, and the mean frequency- $m_b$  curve appears to have a shallow slope (0.93) at low magnitudes which begins to depart from linearity at about  $m_b = 5.7$ , and saturation is indicated at  $m_b > 7.0$ .

Clearly, either the  $m_b$  values for large events reported by the VELA arrays are overestimated, or the network average  $m_b$  values listed by the ISC are subject to a severe negative bias for large events. All evidence obtained to date suggests that the latter is the case. The VELA arrays were operated by trained personnel, and the instruments were carefully calibrated. More importantly, they were equipped with a low gain channel which gave them a wide dynamic range. Also, the form of the seismicity curve in Fig. II-13 is what one might expect, since it is almost identical to the shape of the frequency- $M_s$  curve discussed by Chinnery and North.<sup>16</sup>

Following the arguments given in Ref. 16, and assuming that the VELA seismicity curve is correct, we can make a first empirical estimate of the shape of the  $m_b$ -moment relationship. This is shown in Fig. II-14. The data are consistent with a linear relation between  $M_s$  and  $m_b$ .

for  $m_b$  less than 5.7 or 5.8. The constant in this relationship is not well known, and we have used  $m_b - M_s = 0.5$  in constructing Fig. 11-14. Changing the constant will move the  $m_b$ -moment curve parallel to the log (moment) axis by a small amount.

The  $m_b$ -moment relation shown lies between the  $\omega^2$  and  $\omega^3$  models discussed in the preceding contribution of this report, but there is a suggestion that it is somewhat closer to the  $\omega^2$  model.

M. A. Chinnery  
J. C. Johnston

#### REFERENCES

1. Seismic Discrimination Semiannual Technical Summary, Lincoln Laboratory, M.I.T. (30 June 1976), DDC AD-A032754/4.
2. J. C. Savage, "Relation of Corner Frequency to Fault Dimensions," J. Geophys. Res. 77, 3788-3795 (1972).
3. J. N. Brune, "Tectonic Stress and the Spectra of Seismic Shear Waves from Earthquakes," J. Geophys. Res. 75, 4997-5009 (1970).
4. ———, "Correction," J. Geophys. Res. 76, 5002 (1971).
5. D. York, "Least Squares Fitting of a Straight Line," Can. J. Phys. 44, 1079-1086 (1966).
6. T. C. Hanks and M. Wyss, "The Use of Body-wave Spectra in the Determination of Seismic Source Parameters," Bull. Seismol. Soc. Am. 62, 561-589 (1972).
7. W. Stauder, "Mechanism of the Rat Island Earthquake Sequence of February 4, 1965, with Relation to Island Arcs and Sea Floor Spreading," J. Geophys. Res. 73, 3847-3858 (1968).
8. H. Berckhemer and K. H. Jacob, "Investigation of the Dynamical Process in Earthquake Foci by Analyzing the Pulse Shape of Body Waves," Final Report, Contract AF61(052)-801, Institute of Meteorology and Geophysics, University of Frankfurt, Germany (1968), 85 pp.
9. M. Wyss, T. C. Hanks, and R. C. Lieberman, "Comparison of P-wave Spectra of Underground Explosions and Earthquakes," J. Geophys. Res. 76, 2716-2729 (1971).
10. P. D. Marshall, personal communication from unpublished report (1976).
11. K. Aki, "Scaling Law of Seismic Spectrum," J. Geophys. Res. 72, 1217-1231 (1967).
12. R. J. Geller, "Scaling Relations for Earthquake Source Parameters and Magnitudes," Bull. Seismol. Soc. Am. 66, 1501-1523 (1976).
13. Anonymous, "Operation of Two Observatories," Technical Report No. 66-54, Final Report, Project VT/5054, Teledyne Industries, Geotech Division (1 June 1966), 100 pp.
14. L. Burdick and G. Mellman, "The Response of the WWSSN Short Period Seismometer," Contribution No. 2628, Division of Geological and Planetary Sciences, California Institute of Technology (unpublished paper).
15. E. W. Carpenter, "Absorption of Elastic Waves - An Operator for a Constant Q Mechanism," United Kingdom Atomic Energy Authority, AWRE Report No. 0-43/66 (1966), 16 pp.
16. M. A. Chinnery and R. G. North, "The Frequency of Very Large Earthquakes," Science 190, 1197-1198 (1975), DDC AD-A024236/2.
17. R. J. Geller, "Scaling Relations for Earthquake Source Parameters and Magnitudes," Bull. Seismol. Soc. Am. 66, 1501-1523 (1976).



18. W. Thatcher and T. C. Hanks, "Source Parameters of Southern California Earthquakes," *J. Geophys. Res.* 78, 8547-8576 (1973).
19. "Seismicity of the Southern California Region," Seismological Laboratory, California Institute of Technology (1973).
20. R. G. North, "Station Magnitude Bias -- Its Determination, Causes, and Effects," Technical Note 1977-24, Lincoln Laboratory, M.I.T. (29 April 1977), DDC AD-A041643.
21. R. Madariaga, "Dynamics of an Expanding Circular Fault," *Bull. Seismol. Soc. Am.* 66, 639-652 (1976).
22. J. C. Savage, "Relation Between P- and S-Wave Corner Frequencies in the Seismic Spectrum," *Bull. Seismol. Soc. Am.* 64, 1621-1638 (1974).
23. M. Wyss, "Towards a Physical Understanding of the Earthquake Frequency Distribution," *Geophys. J.* 31, 341-360 (1973).

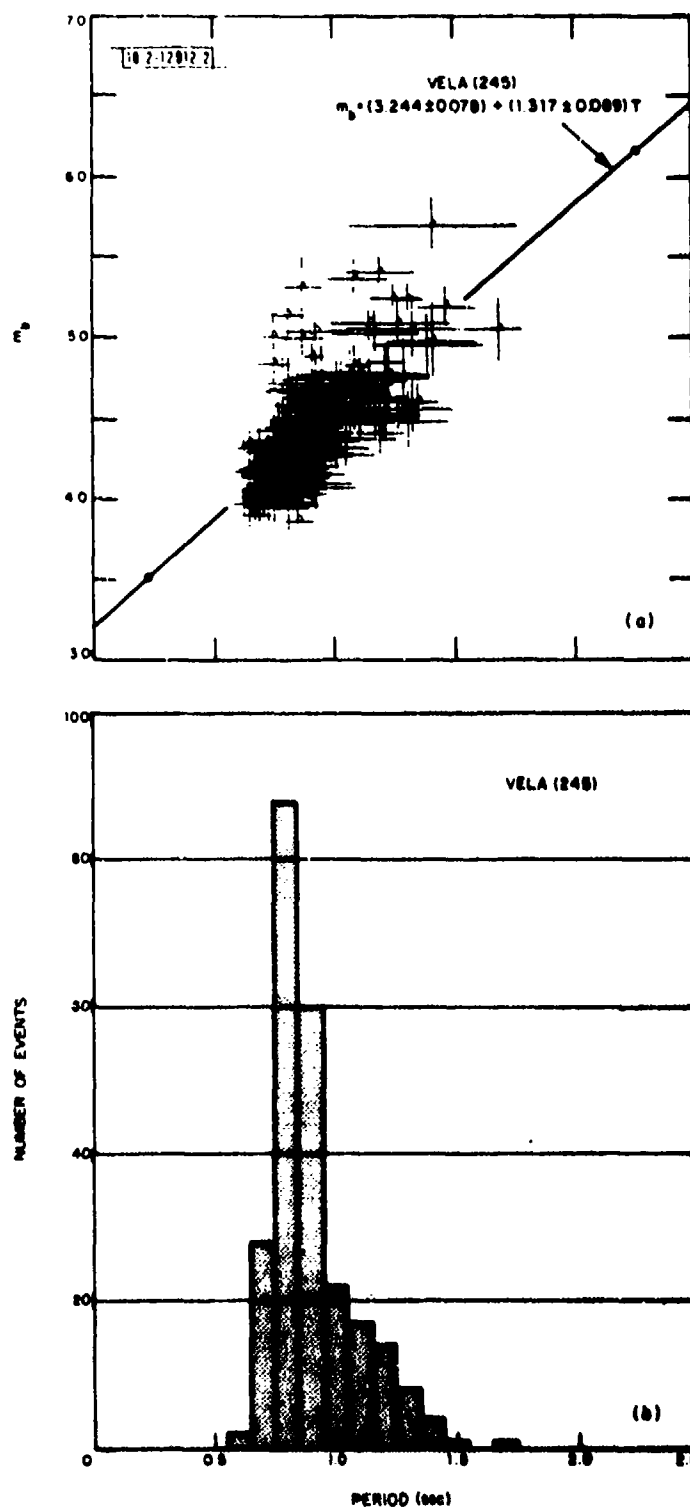


Fig.II-1. (a) Average magnitude  $m_b$  vs average period  $T$  for 245 events commonly recorded at five VELA stations. Error bars indicate standard deviations of  $m_b$  and  $T$  populations about average values. Least-squares line through mean values is shown. (b) Histogram of average periods in (a) grouped in bins 0.4 sec wide.

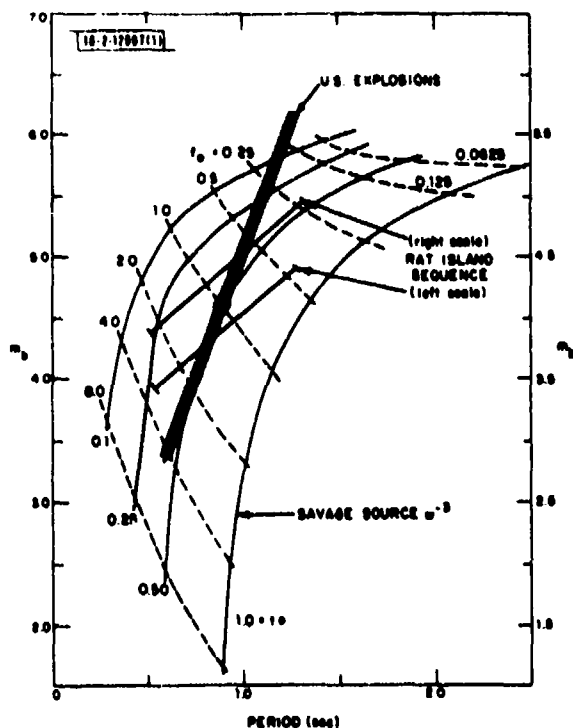
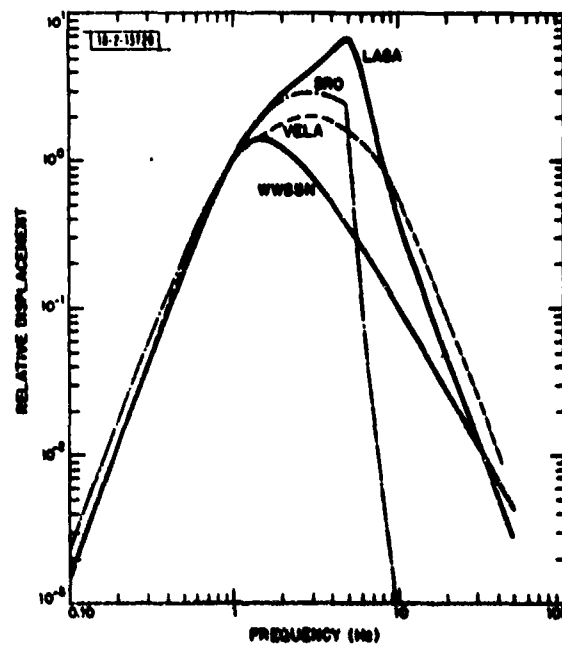


Fig. 11-2. Family of synthetic record amplitudes predicted by Savage source model, shifted to fit trend of Rat Island data. Right-hand  $m_b$  scale refers to upper heavy Rat Island trend line; left  $m_b$  scale refers to lower Rat Island trend line. Hatchured line is  $m_b$  vs  $T$  for U.S. explosions (Marshall<sup>10</sup>), left-hand  $m_b$  scale. Synthetic amplitudes are calculated for corner frequencies 0.0625 to 8 Hz, and  $t^* = 0.1$  to 1.0.

Fig. 11-3. Displacement response of four seismometer systems - WWSN, VELA, SRO, and LASA.



$t^* = T/\bar{Q} = 0.1$

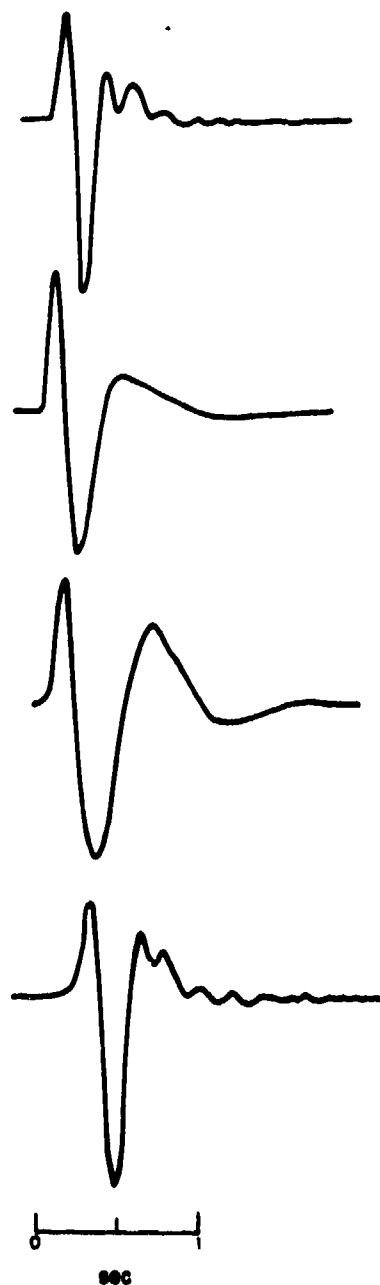


Fig. 11-4. Impulsive displacement response of four seismometer systems, with a small amount of earth attenuation included ( $t^* = 0.1$ ).

10-2-18721

$t^* = T/\bar{Q} = 0.5$   
 $f_0 = 0.5 \text{ Hz (Brune source)}$

10-2-18722

LASA

VELA

WSSN

SRO

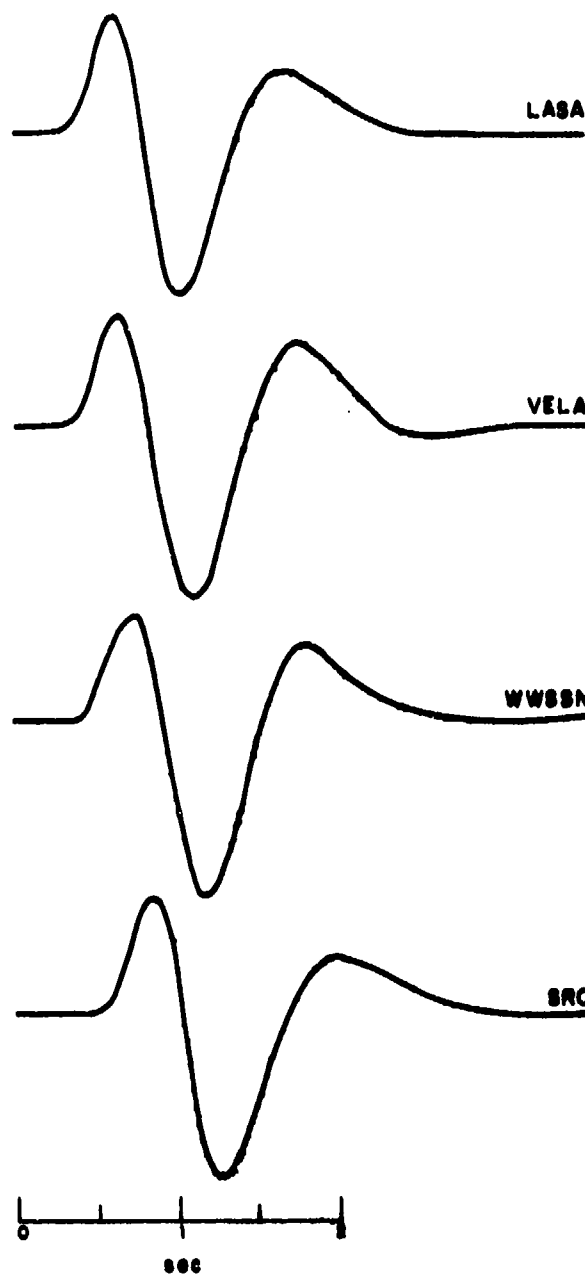


Fig. 11-5. Synthetic records of four seismometer systems using a Brune source model with corner frequency  $f_0 = 0.5 \text{ Hz}$ , and earth attenuation parameter  $t^* = 0.5$ .

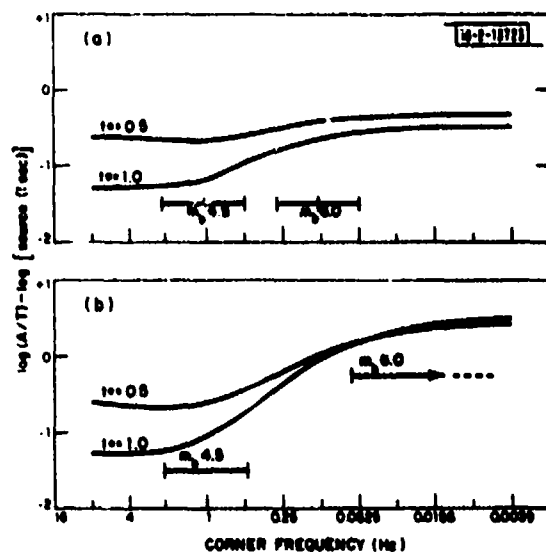


Fig.11-6. Plots of average  $[\log(A/T) - \log \text{ source at 1 sec}]$  for two source models and two attenuation parameters. Log(A/T) values are averaged for four recording systems. (a) Brune source ( $\omega^{-2}$ ); (b) Savage source ( $\omega^{-3}$ ).

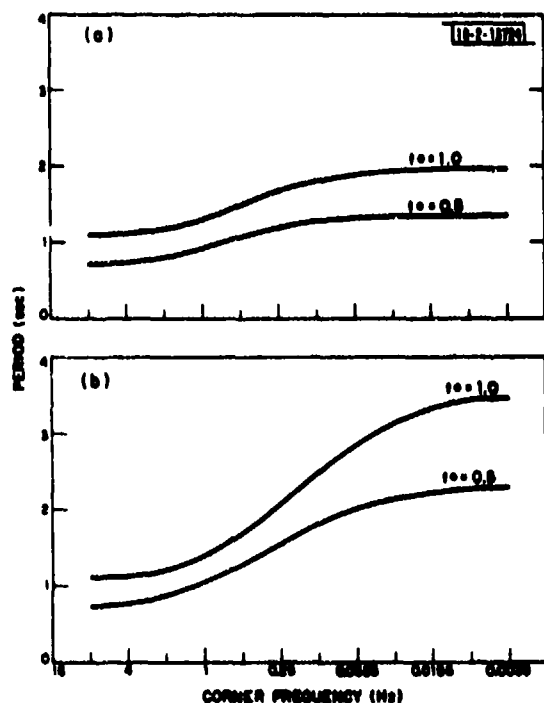


Fig.11-7. Average pulse period  $T$  on synthetic records for two source models and two attenuation parameters.  $T$  values are averaged for four recording systems. (a) Brune source ( $\omega^{-2}$ ); (b) Savage source ( $\omega^{-3}$ ).

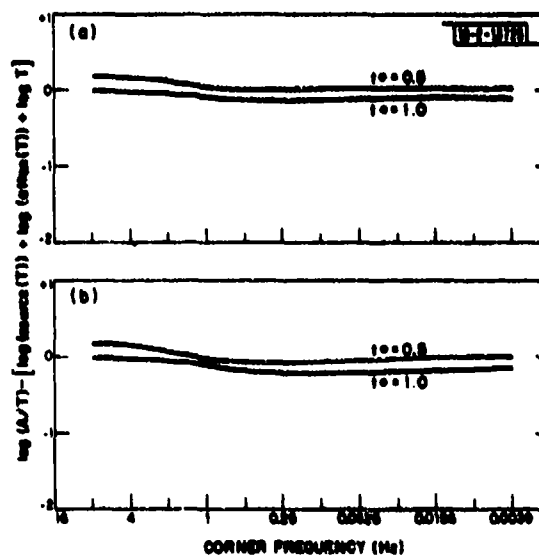


Fig.11-8. Plots of average  $[\log(A/T) - (\log \text{ source at } T \text{ sec} + \log \text{ atten at } T - \log T)]$  for two source models and two attenuation parameters. (a) Brune source ( $\omega^{-2}$ ); (b) Savage source ( $\omega^{-3}$ ).

Fig. II-9. Variation of  $m_b$  with corner frequency for  $\omega^2$  and  $\omega^3$  models, for two different values of  $t^*$ .

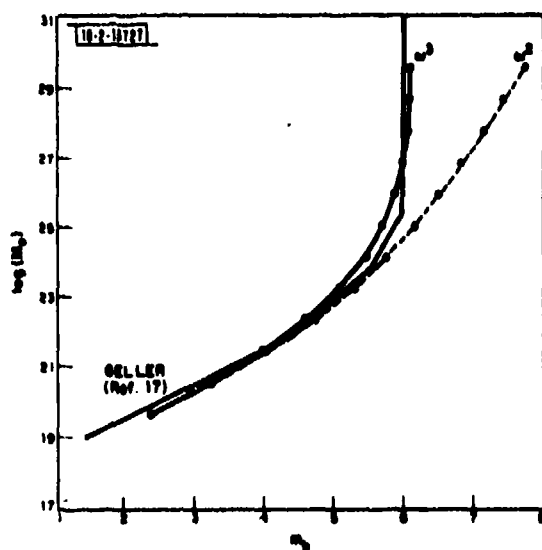
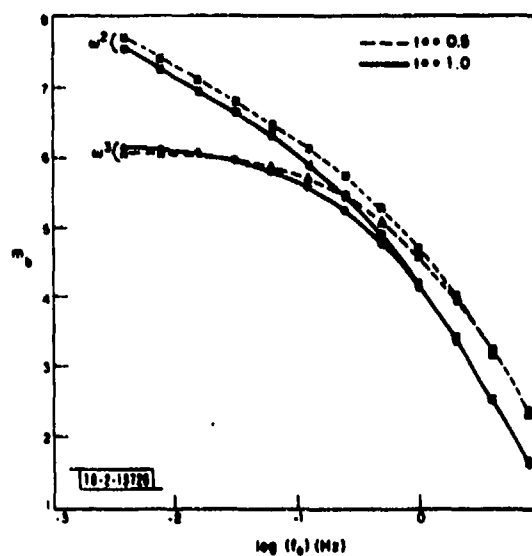


Fig. II-10. Seismic moment as a function of  $m_b$  for source models of Brune ( $\omega^2$ ), Savage ( $\omega^3$ ), and Geller, for  $\Delta\sigma = 10$  bars and  $t^* = 0.5$ .

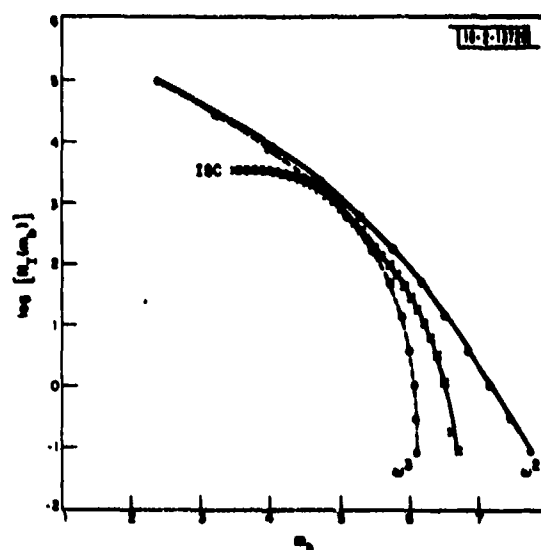


Fig. II-11.  $m_b$ -frequency curves for  $\omega^2$  and  $\omega^3$  models with  $\Delta\sigma = 50$  bars and  $t^* = 0.5$ . Also shown is curve for ISC dataset, 1964 to 1973. All curves reduced to annual occurrence rates.

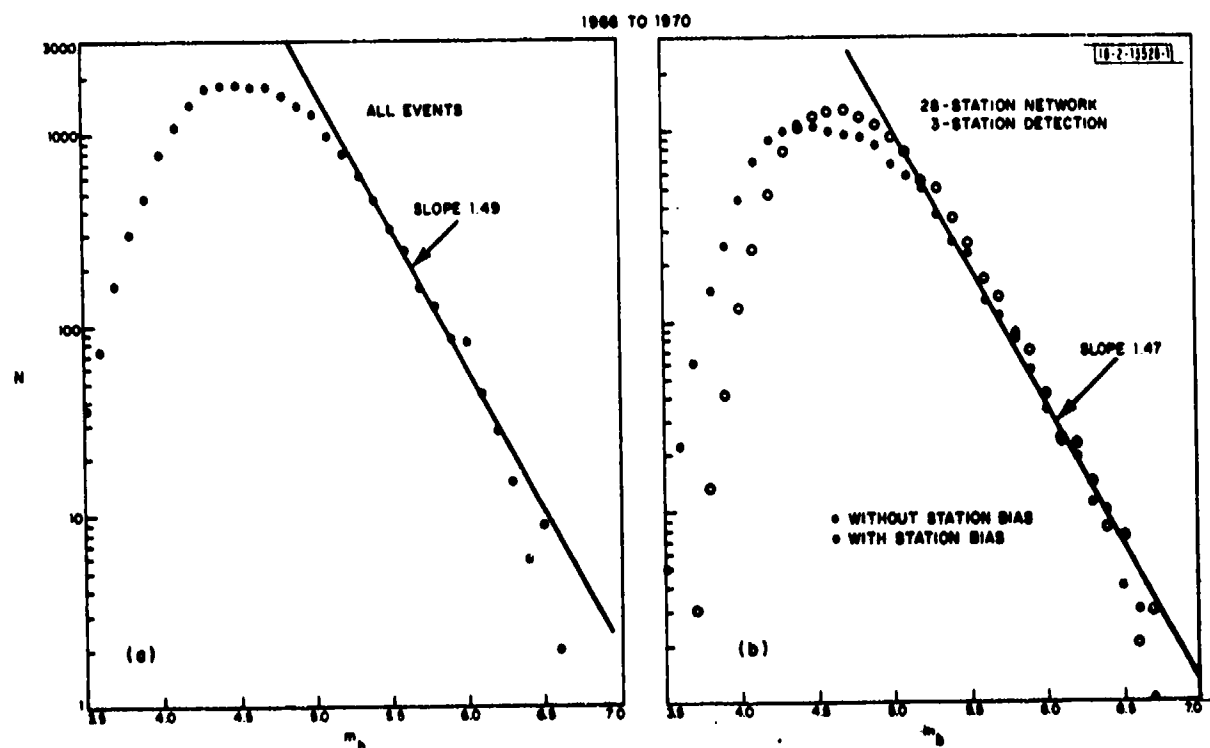


Fig. II-12. (a) Frequency- $m_b$  data for all events in ISC Bulletin for 1966 to 1970. (b)  $m_b$  values recomputed using a 28-station network, and requiring detection by at least three stations. Open circles show changes that result when station biases<sup>20</sup> are included.

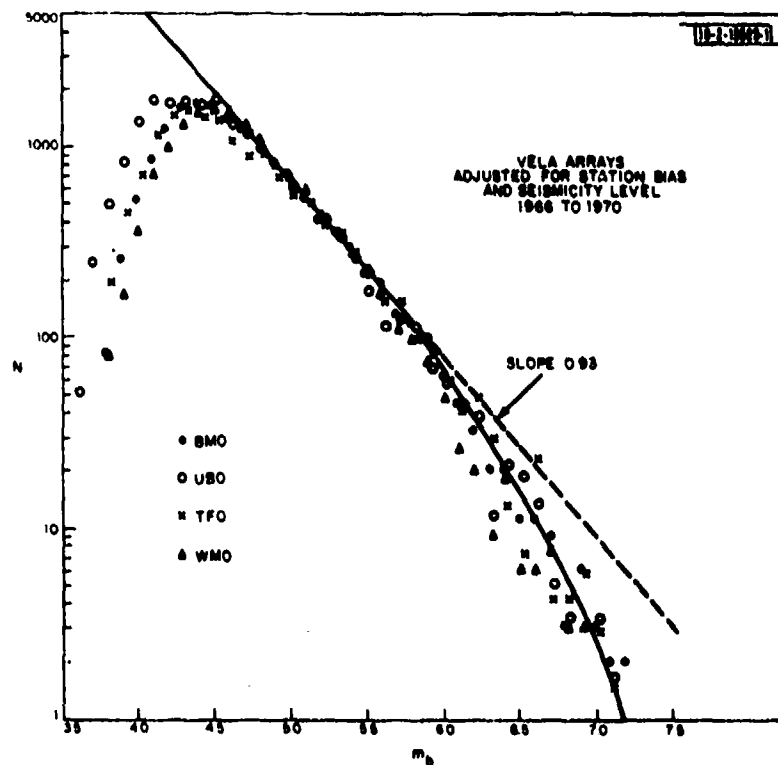
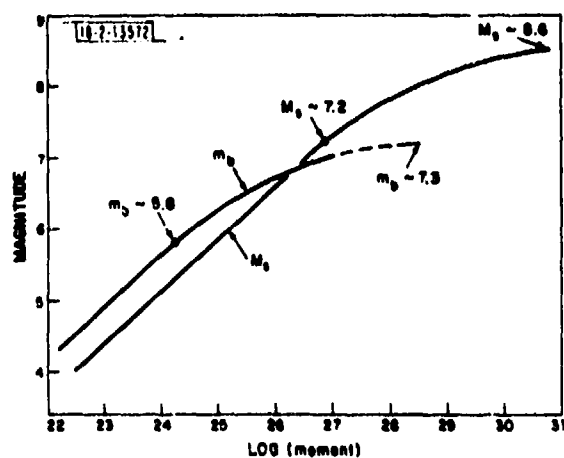


Fig. 11-13. Seismicity for 1966 to 1970 observed by four VELA arrays in Western U.S. Station biases<sup>20</sup> have been included.

Fig. 11-14.  $m_b$ -moment relationship deduced from seismicity curve in Fig. 11-13, assuming moment-frequency curve quoted by Chinnery and North<sup>16</sup> is correct. Empirical  $M_s$ -moment relationship from same study<sup>16</sup> is shown for comparison.





### III. MISCELLANEOUS STUDIES

#### A. AN ANALYSIS OF THE MAIO RECORDING OF THE 20 MARCH 1976 EASTERN KAZAKH EVENT

The multiple event discussed in the previous SATS<sup>1</sup> was analyzed by deconvolution and maximum entropy cepstral analysis. We used the SP SRO recording made at MAIO. Although SRO data are the very best available for digital analysis in terms of their dynamic range and SNR, the choice of the MAIO recording led to two immediate problems. The first concerns the SRO SP recording system response which is discussed in Sec. IV of this report. Due to the extreme anti-alias filter, the SRO SP response is characterized by substantial group delay and 5-Hz ringing. Clearly, any attempt to understand SRO SP recordings should take this effect into account. The second difficulty is due to propagation. Eastern Kazakh, being about 20° away from MAIO, radiates energy through one of the principle discontinuities in the upper mantle. The result is artificial echoes in the wavetrain.

Our approach to the first difficulty, that due to the SRO SP recording system response, was to design an optimum least-squares inverse filter which deconvolves the recording system impulse response out of our seismogram. This filter was computed by a program due to Robinson<sup>2</sup> which also optimizes the time delay of the resulting filter output. Our filter was 41 points (2 sec) long and was computed in the presence of 5-percent additive white noise. The optimum delay time was 1.4 sec. Figure III-1 shows the result of convolving this filter with the SRO SP impulse response. As can be seen, the inverse filter "spikes" the input impulse response sharply at 1.4 sec delay. The other smaller disturbance at approximately 4 sec delay is due to the filter seeing the offset at the end of the impulse response.

The results of applying this inverse filter to the MAIO recording of the 20 March 1976 event are shown as the first four traces in Fig. III-2. Trace 1 is the original recording. Trace 2 is the original recording filtered with a 3-pole Butterworth bandpass filter with low and high -3-dB points at 0.5 and 4.0 Hz, respectively. Trace 3 is the original recording deconvolved with the inverse filter described above. The fourth trace is trace 3 filtered with the same bandpass filter used to produce trace 2.

Looking at trace 3, one can easily see that the inverse filter removes the group delay in the SRO SP response. The filter delay of 1.4 sec has been removed by shifting the trace. The effect of the filter on noise outside the signal band can also be seen. This noise is removed in trace 4 by bandpass filtering; however, the phase of the bandpass filter is introduced. So, trace 4 can be thought of as the original recording equalized in amplitude from 0.5 to 4.0 Hz with a 3-pole Butterworth phase response.

In the first 20 sec of the deconvolved seismogram (trace 3), four primary phases, two depth phases, and three echoes can be identified. The first arrival and its associated depth phase and echo are very faint. Its pP delay is somewhere in the 3 to 5 sec range. The second arrival exhibits a very clear pP phase with a delay of 2.4 sec, and an echo with a delay of 8.8 sec and relative amplitude of 0.833. The third arrival has no apparent pP phase, and its associated echo is mixed in with the fourth arrival. This last arrival has a clear echo, but its pP phase is lost in the increasing coda.

The results of anti-echo filtering the deconvolved seismogram are shown as trace 5. The procedure consisted of computing the inverse z-transform of the echo; i.e.:

$$(1 + az^b)^{-1} = 1 - az^b + a^2 z^{2b} - a^3 z^{3b} + \dots$$

and convolving with the echoed seismogram. The echoes  $E_1$ ,  $E_2$ , and  $E_4$  are removed from the trace. This, then, is the final "cleaned-up" seismogram. Here, the first motions of  $P_2$ ,  $P_3$ , and  $P_4$  can easily be seen to be upward. The first motion of  $P_1$  cannot be identified.

A maximum entropy cepstrum of the deconvolved seismogram, trace 4 in Fig. III-2, is shown in Fig. III-3. The three most prominent peaks occur at 2.6, 4.7, and 8.9 sec, respectively. The last can be identified as the travel-time curve echo delay. The first two are possibly pP times of the primary arrivals. In particular, 4.7 sec may correspond to the pP delay of  $P_4$  which cannot be identified in the seismogram.

On the basis of this analysis we conclude that, in the first 20 sec of the MAIO recording, only one arrival appears to be definitely lacking a pP phase. That arrival was  $P_3$  which arrived at approximately 04:08:08.5 on the original seismogram.

D. W. McCowan  
T. E. Landers

#### B. CRUSTAL-PHASE TRAVEL TIMES FROM NTS EXPLOSIONS: PRELIMINARY RESULTS

We have compiled an extensive data set of travel times from NTS explosions recorded mainly at Long Range Seismic Measurements (LRSM) stations in the Western U.S. It was our original intention to rely on the Geotech shot reports for tabulated observations. However, we found that there were no S-phase times and very few P\* times in these reports. So, in order to acquire more data, we reread the original 35-mm LRSM film recordings. A side benefit of this procedure was observational uniformity, since all the data were read by one analyst. We arbitrarily limited ourselves to explosions for which there were announced yields, giving us data from 25 events. A map of the stations is included as Fig. III-4. Unfortunately, because the LRSM sites continually changed location during the recording period, there were few common stations.

These travel-time observations were checked for errors and erroneous readings. They were then placed in our Data Analysis and Display System (DADS) for analysis and display. Altogether, we had 171, 76, 54, 47, 183, and 85 Pg, Sg, P\*, S\*, Pn, and Sn observations, respectively. As can be seen, there were fewer S-phase observations than corresponding P-phase observations and, in both cases, more n-phase observations than either g or \* observations. This is not unusual and, most likely, is due to the variability of the crust over the station coverage.

Plots of residuals for all six phases as compared with those from a Jeffreys-Bullen (J-B) crustal model are shown in Figs. III-5 to III-7. The model is a two-layer crust over a mantle halfspace with values chosen to fit the J-B crustal-phase tables. Layer parameters are given in Table III-1. Least-squares lines fitted to the corresponding residuals are also shown in Figs. III-5 to III-7.

Two sources of error can be easily seen in these figures. The first is a random observational error which is independent of distance. Comparing Figs. III-5(a), III-6(a), and III-7(a) with Figs. III-5(b), III-6(b), and III-7(b), one can see that the random error component is at least twice as great for S phases as for corresponding P phases. We feel that this error is due to inaccurate time picks. The S phases, coming later in the P coda, are harder to pick and are therefore less-accurately read.

TABLE III-1 CRUSTAL MODEL FOR THE WESTERN UNITED STATES					
Layer	Thickness (km)	J-B P (km/sec)	J-B S (km/sec)	P (km/sec)	S (km/sec)
1	15	5.57	3.37	6.03	3.50
2	18	6.50	3.74	6.73	3.80
3	$\infty$	7.85	4.42	7.88	3.97

The second error component is a trend which clearly depends on distance. It can be seen best in Fig. III-7(a) for the Pn phase. After removing the random error due to observation, we estimate that the absolute value of the remaining error in the Pn residual is approximately 0.4 sec/deg. We feel that this error component is due to the effects of crustal heterogeneity in the Western U.S. For example, stations near the NTS will only see the Basin and Range crustal structure because that is where the NTS is located. Stations further away will see other crustal structures, depending on how far away they are from the NTS and along which azimuth. It is one of our objectives to sort the travel times by azimuths and attempt to identify the effects of varying crustal structures.

The data shown in Figs. III-5 to III-7 can be used to perform a refraction survey of the Western U.S. The procedure is the same as that commonly used in petroleum exploration (for example, see Dobrin<sup>3</sup>). The P- and S-wave-velocity results are given in Table III-1. Our model favors higher P and S velocities in both crustal layers, a Pn velocity very close to the J-B value, and a lower Sn velocity than predicted by the J-B tables. The most accurate velocities are Pg and Pn. P\* appears to be variable between sites, and all the S phases show considerable scatter.

Our data were not accurate enough, before sorting into azimuths, to resolve the layer thicknesses. The P\* and S\* times indicate a first-layer thickness of 27 and 14 km, respectively. We do not consider either value significant. On the other hand, the very small intercept on the Pn residual plot [Fig. III-7(a)] implied a Moho depth close to the J-B value of 33 km. Since these are the data with the least scatter, we do consider this value significant. To summarize, our preliminary analysis of this crustal-phase data indicates that the J-B crustal thickness and Pn velocity are good approximations to the Western U.S. The J-B crustal layers have lower P- and S-wave velocities than our data suggest.

These preliminary results generally agree with those from other investigations. Our crustal thickness, 33 km, agrees with Glover and Alexander's<sup>4</sup> crustal thickness for the NTS as well as with Warren and Healy's<sup>5</sup> contour map of Moho depth in the Western U.S. Our Pn velocity, 7.88 km/sec, is the same as that determined by long-profile refraction surveying reported by Eaton.<sup>6</sup> In short, these data support the substantial tectonic research done on the Basin and Range province.

We intend to use these data in an experiment to determine how much crustal-phase travel-time observations improve teleseismic hypocenter locations. After fixing a structure for the Western U.S. on the basis of these data, we will start relocating NTS explosions and earthquakes

in the general source region. We expect that these results will aid in evaluating the location capabilities of the near-in networks.

D. W. McCowan  
R. E. Needham

### C. THE DEPTH OF SEISMICITY IN AN IRANIAN AFTERSHOCK SEQUENCE

The lack of nearby stations and poorly known velocity structure of parts of Asia causes the teleseismically found focal depths of earthquakes in these regions to be badly controlled — an effect seen clearly in the Zagros mountains of Iran, where the reported deep events are nearly all poorly recorded (Fig. III-8).

The Gir (1972) aftershock sequence in Southern Iran was relocated by the master-event technique<sup>7</sup> using ISC Bulletin data, to try and precisely determine depths relative to the master; the advantage of this method is that the dependence of computed depths on the assumed earth model is reduced.

The main destructive event (magnitude 6.0) was a thrust preceded by a small foreshock, making onsets difficult to read; but in the absence of a large event as an alternative, it was retained as the master. The relocations are shown in Figs. III-9(a) and (b) and have the same strike as the fault-plane solution for the master; they also define a plane dipping NE at 60° to 70° — an effect dramatically seen when their position vectors are plotted on a stereographic projection centered on the master [Fig. III-9(c)]. Locations are all relative to the master event, whose initially chosen position determines the absolute locations. Great care was taken to exclude bad data from the relocations; all records from WWSSN stations closer than 30° were reread and poor onsets were discarded from the dataset, along with those events too poorly recorded for an adequate station distribution in the relocation. That the average absolute rms residuals drop from ~1.25 to ~0.53 sec is a measure of the success of this technique, and suggests that about half the uncertainty in the absolute locations in this region derives from the assumed earth model. Ten other events were found on this fault trace, including one of 14 September 1968, magnitude 5.8, which had a mechanism almost identical to the master, and are included in Fig. III-9(c). These results strongly indicate that the NE dipping plane of the focal mechanism is the fault plane and that the relative depths obtained are meaningful. It is interesting to note that the main shock is at the top of the sequence which extends downward some 40 km. Vast salt deposits are known in this part of the Zagros, perhaps preventing, with their ductility, any rupture from reaching the surface (no surface break was found). Another apparent anomaly is that the dip of the aftershock zone (60° to 70°) is considerably steeper than that of the fault-plane solution (36°) with a focal velocity of 6.8 km/sec. The dip of this fault plane in the focal mechanism increases as the focal velocity decreases, but even at  $V_p = 6.0$  km/sec (the minimum likely at shallow depths) the dip increases to only 43°. If the depths found here are real, it would suggest that either the fault is steeper at depth than at the initial break, or that the main shock occurred in a limited region of anomalously low velocity.

The effectiveness of this technique with crustal earthquakes lends it to several applications. As well as the obvious possibilities of resolving fault-plane ambiguities in focal mechanisms, fault-plane areas may be estimated and are, in general, better defined than is possible with either geographic or conventional joint epicenter determinations which use residuals in the master-event location as station corrections in relocating aftershocks. If aftershock zones are more condensed and shallower than conventional relocations show, the corresponding stress

drops and seismic displacements increase, decreasing the discrepancy between seismic and plate motions in Asia<sup>8,9</sup> though probably not removing it entirely. This work has been continued with other Iranian aftershock sequences, and may be extended to Central Asia in the future.

T. J. Fitch,  
J. Jackson†

#### D. TWO-DIMENSIONALIZED VELOCITY ANOMALIES

Lateral heterogeneity in the crust and upper mantle limits the accuracy of earthquake locations and magnitude determinations. It is common practice to add station corrections to standard travel times to compensate for disparities between the real transmission paths and paths inferred from a standard earth model, thereby achieving more accurate locations. Similarly, estimates of  $M_s$  and  $m_b$  can be corrected for station amplitude biases. Both corrections are statistical in nature and thus ignore the underlying physics of seismic transmission in the real earth.

Here we present a scheme for the conversion of differential arrival times to velocity anomaly patterns pertinent to near-source regions. With teleseismic data, only the velocity anomalies seen by diving rays are resolved. In principle, the anomaly patterns can be used to compute near-source corrections to magnitude and moment as well as to travel times.

The analysis begins by locating a group of events relative to a master.<sup>7,10</sup> Residuals at each station are averaged, and the mean residuals are projected onto a vertical plane normal to the trend of the seismic zone. This is carried out by projecting the tangents to the ray paths from the master into the appropriate vertical plane. Angles of incidence were computed from Herrin and J-B earth models for P and PKP phases, respectively. The azimuths of the ray paths are taken from absolute locations.

The velocity anomalies are linearly related to the mean projected residuals through velocity partial derivatives. The assumption is made that classical ray parameters computed from the assumed earth models are, at least on the average, unchanged by lateral heterogeneity in the source region. In the results presented here, the relative locations are not adjusted for the nonuniformity of the source velocity. Consequently, the anomaly patterns may contain significant bias.

Datasets were compiled from P and PKP arrivals listed in the ISC Bulletins. Records from WWSSN stations in the region of the activity were reread if the reported times yielded travel-time residuals greater than 4 to 5 sec.

Anomaly patterns for compressional velocity in the near-downward vertical direction are presented for two groups of earthquakes: deep focus activity within 130 km of a master at a depth of 650 km in the Tonga seismic zone [Figs. III-10(a) and (b)], and intermediate depth activity between 38° and 40°N beneath Northern Honshu [Figs. III-11(a) and (b)]. Figure III-10(b) shows a broad velocity anomaly of about 0.3 km/sec in the down-dip direction of the seismic zone. The anomaly pattern for the Northern Honshu earthquakes [Fig. III-11(b)] shows a sharp minimum and maximum, each with a magnitude of about 0.5 km/sec. The minimum is nearer the down-dip direction. For this region no ray paths to teleseismic stations leave the source region in the down-dip direction, about 36° toward the west.

The statistical significance of the anomaly patterns in Figs. III-10 and III-11 is tested in Figs. III-12 and III-13. By definition, a least-squares solution yields residuals with a zero

† Cambridge University, Cambridge, England.

mean. Consequently, the mean of any subset of these residuals will tend to zero as the size of the subset increases, if the residuals are random variables. This trend is represented by the curves in Figs. III-12 and III-13. Data points above these curves have a significant nonrandom component. In Fig. III-12, mean projected residuals from the Tonga dataset are compared with residuals from a synthetic dataset which has the gross statistical properties of the real data. In addition, the synthetic data were computed from station and source distributions that are identical to the real ones. Clearly, the synthetic residuals show a higher degree of randomness; however, several synthetic data points fail the test for randomness, probably because of nonuniformity in the spatial distribution of sources and receivers.

The two-dimensionality of the Honshu seismic zone is tested in Fig. III-13. The data points that lie above the  $2\sigma$  curve correspond to the maximum and minimum in the anomaly pattern in Fig. III-11. The residuals are almost completely randomized by projecting the mean residuals onto a plane  $45^\circ$  to the trend of the zone. However, to some extent this effect may be encouraged by the teleseismic station distribution which is grossly nonuniform in azimuthal coverage.

More datasets will have to be processed to establish features of these anomaly patterns that can be considered characteristic of mantle seismic zones in different depth ranges and crustal activity of various kinds. Once the credibility of these patterns is established, then amplitude effects can be modeled.

T. J. Fitch  
J. Jackson†

#### E. PRECISE LOCATION OF OCEANIC RIDGE EARTHQUAKES

The world's oceanic ridge system is characterized by shallow-depth (<5- to 10-km) earthquakes of intermediate magnitude ( $m_b$  4 to 6). Detailed knowledge of the location of epicenters relative to each other and to the ridge's islands, bathymetric features, and magnetic/gravity fields would be useful for geophysical studies as well as nuclear monitoring activities. Unfortunately, conventional methods for determining earthquake epicenter locations may not be adequate to attain the required precision and accuracy, in that relatively simple Jeffreys-Bullen<sup>11</sup> or Herrin<sup>12</sup> earth-velocity models are used to calculate epicentral distances. These models, which generally show a thick low velocity (6.0 km/sec) continental crust overlying a higher velocity (7.8 km/sec) mantle, are clearly not applicable to oceanic ridges. Here, high-velocity mantle material probably extends to within 3 to 5 km of the seafloor. Also, significant velocity inversion may exist at depth.<sup>13,14</sup>

The computation of the location of earthquakes which are recorded by many observatories distributed in an azimuthally uniform pattern around the epicenter is, of course, insensitive to the errors of any radially symmetric earth-velocity model, in that the distance error along one ray-path azimuth is compensated by equal error in the opposite direction along the reciprocal ray-path azimuth. By simply averaging many ray paths, a good estimate of the epicenter location is possible. Unfortunately, few earthquakes are ever recorded by such an ideal station distribution. Thus, epicenter-location errors can be expected to be biased in the general direction toward the greatest number of recording stations.

This biasing effect is well exhibited by the earthquake epicenters which have been located along the central mid-Atlantic ridge by the ISC for the years 1964 to 1973 and the USGS since 1973. Here, the relatively small ridge-crest events are primarily recorded by North American observatories ( $n \sim 50$ ), since there are few North African observatories ( $n \sim 5$ ).

† Cambridge University, Cambridge, England.

Figure III-14 shows the ISC computed epicenter locations relative to the topographically defined median-rift valley and the transform fault tectonic axis between 15° and 29°N latitudes. The topography information was taken from recently compiled detailed U.S. Navy bathymetry contour charts (Naval Research Laboratory). The positional accuracy of the axial tectonic loci is estimated to be on the order of  $\pm 4$  km. For this study, the tectonic axis, as defined by the bathymetric data, has been digitized for incorporation into a variety of plotting and analysis programs. The digitization process was applied over small individual segments of the ridge, whose size depended on the detail of the bathymetric charts available. When completed, the mid-Atlantic ridge axis will have been continuously digitized between 5° and 65°N latitudes. The total digital length of the ridge is expected to produce a data base of over 30,000 points, or about 2 points each kilometer of median valley and transform fault length. While this degree of resolution may not be necessary in the initial stages of the study reported here, it will be required later for developing detailed, local ridge axis, crustal/upper-mantle models.

Careful inspection of Fig. III-14 reveals that the epicenters are rather widely scattered, but most are clearly clustered west of the northerly trending median valley segments or north of the easterly trending transform faults. One might have expected the epicenters to have been normally distributed about the tectonically active median valley and transform fault axes. In fact, detailed microearthquake studies on the mid-Atlantic ridge using local ocean-bottom seismometers and sonobuoys show all seismicity to be confined to within 5 km of the median valley and transform fault axes.<sup>15-18</sup> This systematic location offset discrepancy of about 15 to 20 km, which is best seen in the vicinity of the Kane Transform Fault at 24°N latitude (Fig. III-15), probably reflects the simple fact that most of the recording stations are indeed located to the north and west of the ridge in North America. Thus, use of the relatively "slow" J-B earth-velocity model by the ISC rather than a more-appropriate "fast" oceanic ridge axis model would be expected to "pull" the epicenters toward the biasing North American stations. An increase in the average crustal velocity beneath the ridge axis by about 20 percent is implied.

The large scatter in the epicenter locations, especially along the transform faults, as compared with the narrow tectonic activity zone inferred by the local microearthquake studies, is also noteworthy. The scatter may be real, which would suggest a fundamental difference between small microearthquake and large, teleseismically recorded earthquake mechanisms. This is undoubtedly true for some of the large teleseismic events located well off the ridge axis (> 50 to 100 km) which show thrust mechanisms.<sup>19</sup> Alternatively, the scatter could simply result from the same station-biasing effect which has offset the entire epicenter pattern from the ridge axis. It may be that relocation of the ISC and USGS epicenters with an improved "oceanic ridge" velocity model, which translates the epicenter pattern onto the median valley and transform fault axes, will also reduce the near-axis scatter.

J. D. Phillips  
R. M. Sheppard

## REFERENCES

1. Seismic Discrimination SA 11, Lincoln Laboratory, M.I.T. (31 March 1977), DDC AD-A045453.
2. E. A. Robinson, Multichannel Time Series Analysis with Digital Computer Programs (Holden-Day, San Francisco, 1967).
3. M. B. Dobrin, Introduction to Geophysical Prospecting (McGraw-Hill, New York, 1960).
4. P. Glover and S. S. Alexander, "A Comparison of the Lake Superior and Nevada Test Site Source Region," Geotech Report No. 243, Alexandria, VA (1970).
5. D. H. Warren and J. H. Healy, "Structure of the Crust in the Conterminous United States," *Tectonophysics* **20**, 203-213 (1973).
6. J. P. Eaton, "Crustal Structure from San Francisco, California, to Eureka, Nevada, from Seismic Refraction Measurements," *J. Geophys. Res.* **68**, 5777-5787 (1963).
7. T. J. Fitch and K. J. Muirhead, "Depths to Larger Earthquakes Associated with Crustal Loading," *Geophys. J. R. Astr. Soc.* **37**, 285-296 (1974).
8. R. G. North, "Seismic Slip Rates in the Mediterranean and Middle East," *Nature* **252**, 560-563 (1974).
9. W. P. Chen and P. Molnar, "Seismic Moments of Major Earthquakes and the Average Rate of Slip in Central Asia," *J. Geophys. Res.* **82**, 2945-2969 (1977).
10. Y. Fukao, "Source Process of a Large Deep-focus Earthquake and its Tectonic Implications - the Western Brazil Earthquake of 1963," *Phys. Earth Planet. Int.* **5**, 61-76 (1972).
11. H. Jeffreys and K. Bullen, "Seismological Tables," British Association, Gray-Milne Trust (1940).
12. E. Herrin, "1968 Seismological Tables for P Phases," *Bull. Seismol. Soc. Am.* **58**, 1193 (1968).
13. L. Steinmetz, R. B. Whitmarsh, and V. S. Morsira, "Upper Mantle Structure Beneath the Mid-Atlantic Ridge North of the Azores Based on Observations of Compressional Waves," *Geophys. J. R. Astr. Soc.* **50**, 353-380 (1977).
14. S. C. Solomon and B. R. Julian, "Seismic Constraints on Ocean-Ridge Mantle Structure: Anomalous Fault-Plane Solutions from First Motions," *Geophys. J. R. Astr. Soc.* **38**, 265-285 (1974).
15. T. J. G. Francis and I. T. Porter, "Median Valley Seismology: The Mid-Atlantic Ridge Near 45°N," *Geophys. J. R. Astr. Soc.* **34**, 279-311 (1973).
16. T. Francis, I. Porter, and J. McGrath, "Ocean-bottom Seismograph Observations on the Mid-Atlantic Ridge Near Latitude 37°N," *Geol. Soc. Amer. Bull.* **88**, 664-677 (1977).
17. R. C. Spindel, S. B. Davis, K. C. Macdonald, R. P. Porter, and J. D. Phillips, "Microearthquake Survey of Median Valley of the Mid-Atlantic Ridge at 36°30'N," *Nature* **248**, 577-579 (1974).
18. I. Reid and K. Macdonald, "Microearthquake Study of the Mid-Atlantic Ridge Near 37°N, Using Sonobuoys," *Nature* **246**, 88-90 (1973).
19. L. R. Sykes and M. L. Sbar, "Intraplate Earthquakes, Lithospheric Stresses and the Driving Mechanism of Plate Tectonics," *Nature* **245**, 298-302 (1973).



Fig. III-1. Result of convolving least-squares inverse filter with SRO SP impulse response. Filter is 2.0 sec long and was designed with 5-percent additive white noise. Output occurs with delay of 1.4 sec.

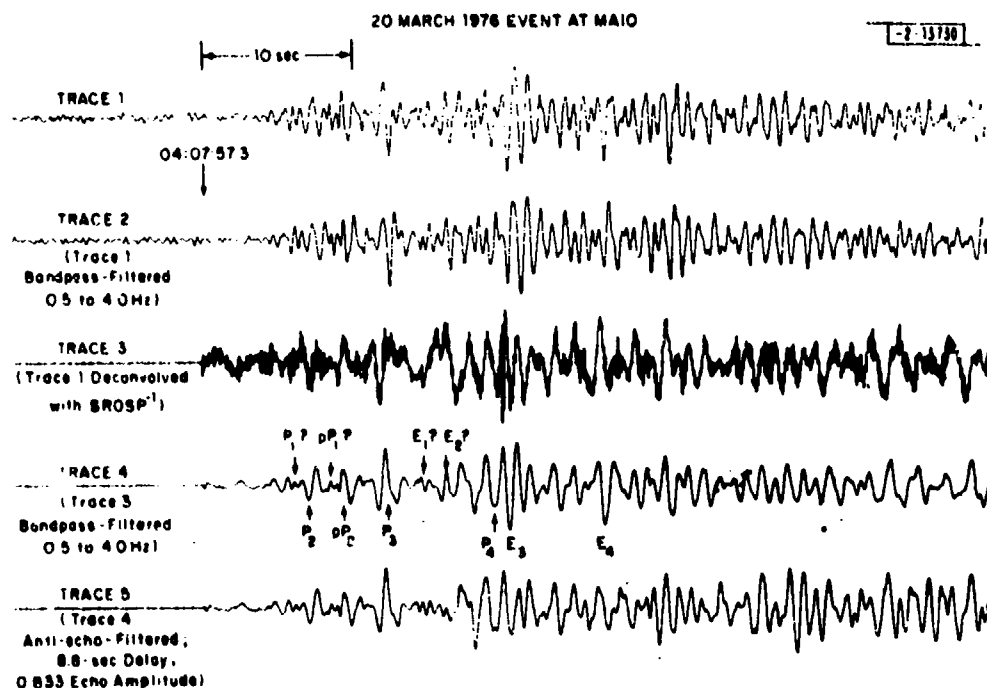
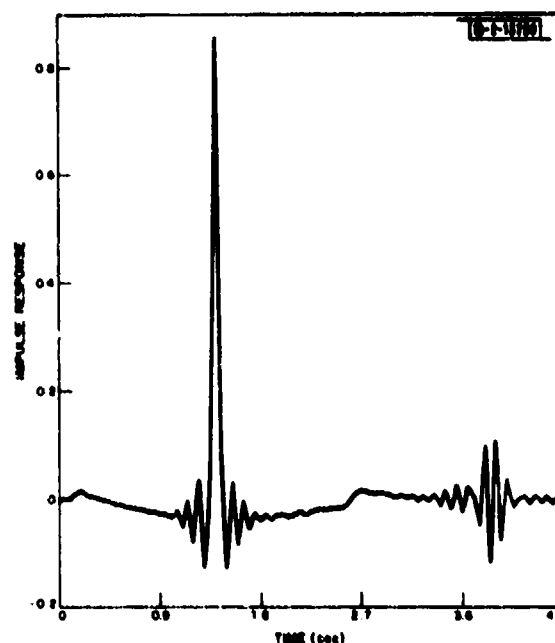


Fig. III-2. Results of deconvolving and anti-echo filtering MAIO recording of 20 March 1976 E. Kazakh event.

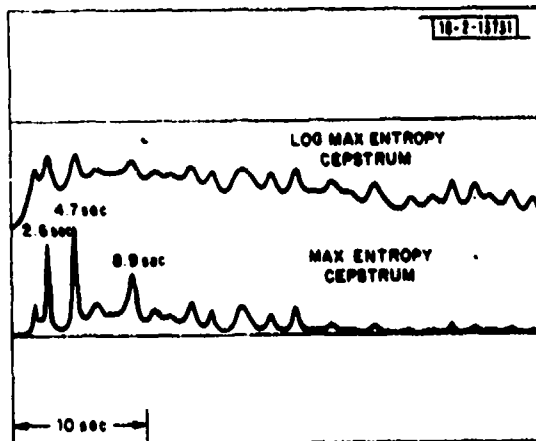


Fig. III-3. Maximum entropy cepstrum of deconvolved seismogram.

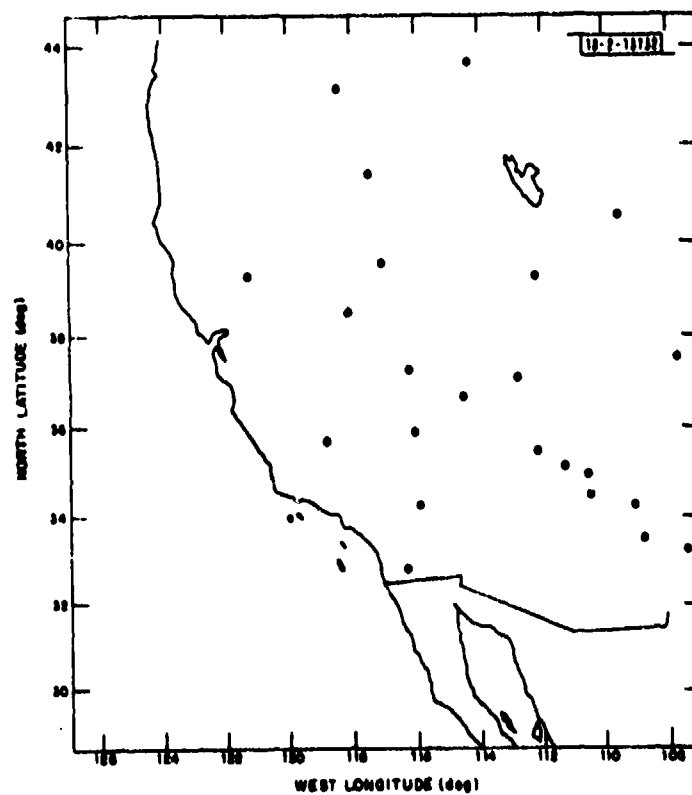


Fig. III-4. Map of stations used in crustal-phase travel-time study.

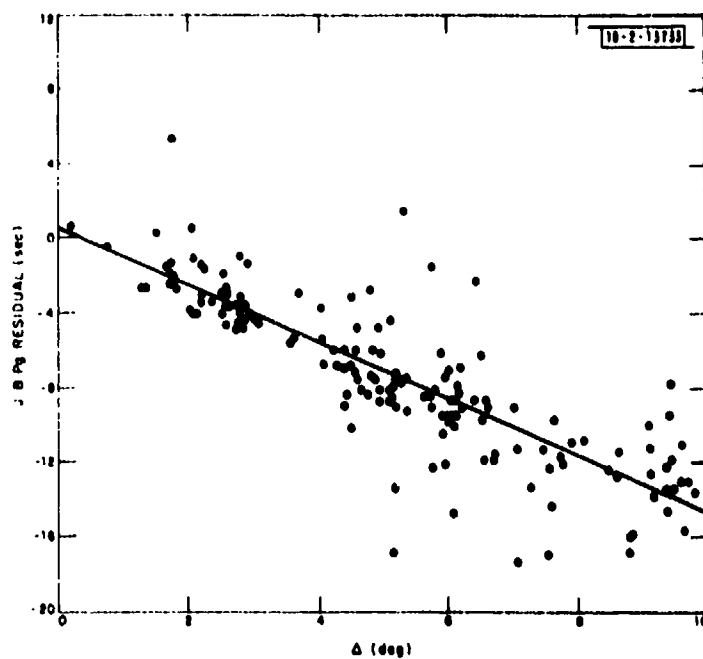


Fig. III-5(a). J-B Pg residual plot. Line equation is:  
 $R = -1.53 \Delta + 0.517 \text{ sec.}$

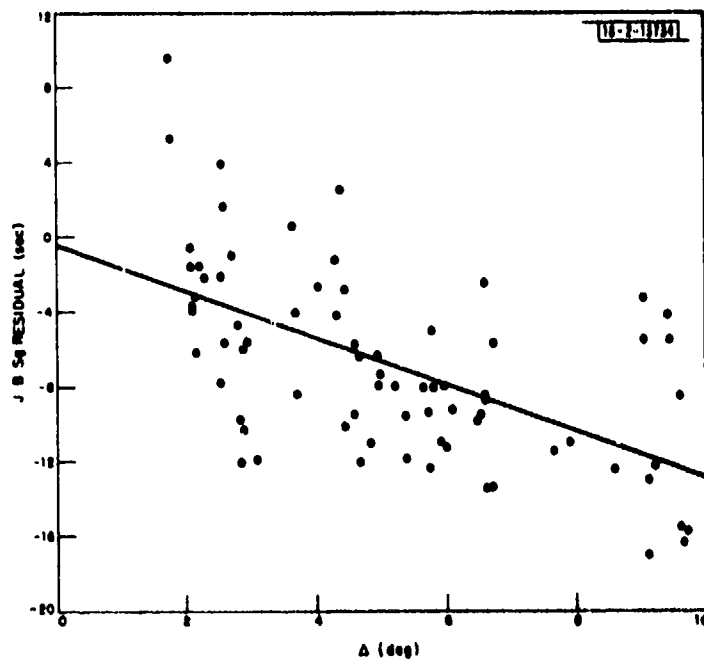


Fig. III-5(b). J-B Sg residual plot. Line equation is:  
 $R = -1.25 \Delta - 0.401 \text{ sec.}$

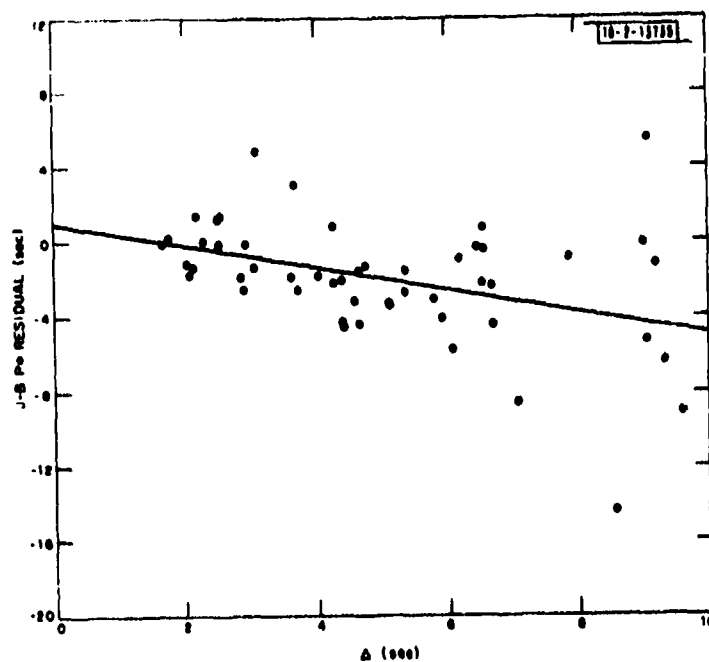


Fig.III-6(a). J-B P\* residual plot. Line equation is:  
 $R = -0.593 \Delta + 0.971 \text{ sec.}$

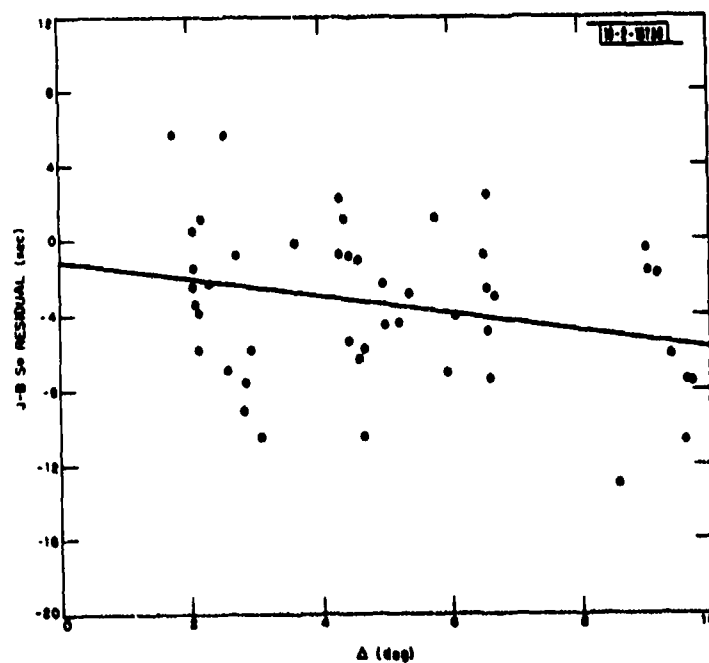


Fig.III-6(b). J-B S\* residual plot. Line equation is:  
 $R = -0.475 \Delta - 1.13 \text{ sec.}$

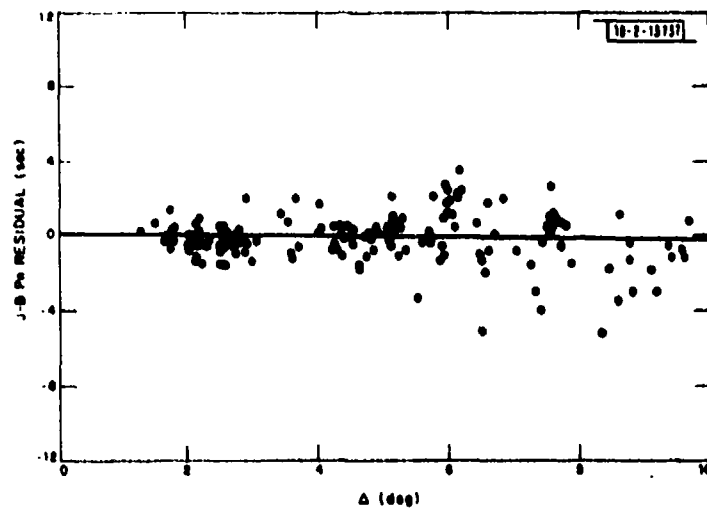


Fig. III-7(a). J-B Pn residual plot. Line equation is:  
 $R = -0.0586 \Delta + 0.127 \text{ sec.}$

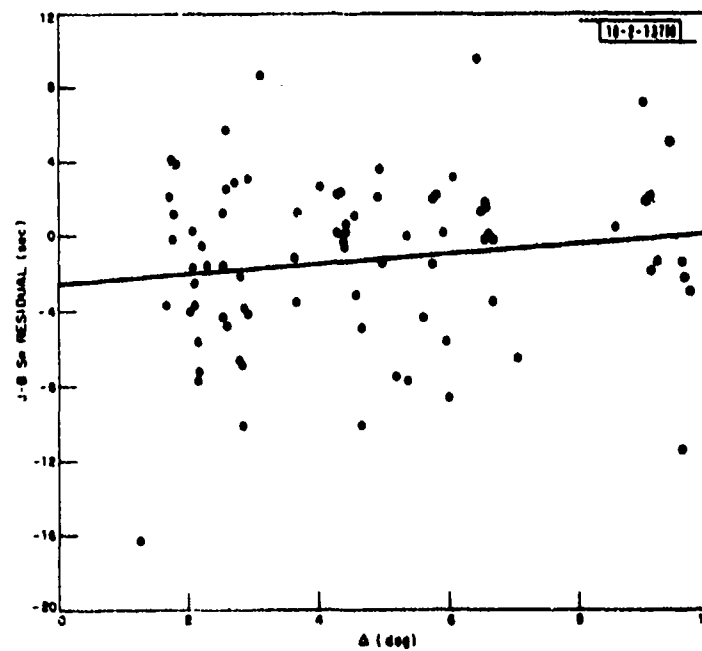


Fig. III-7(b). J-B Sn residual plot. Line equation is:  
 $R = +0.288 \Delta - 2.55 \text{ sec.}$

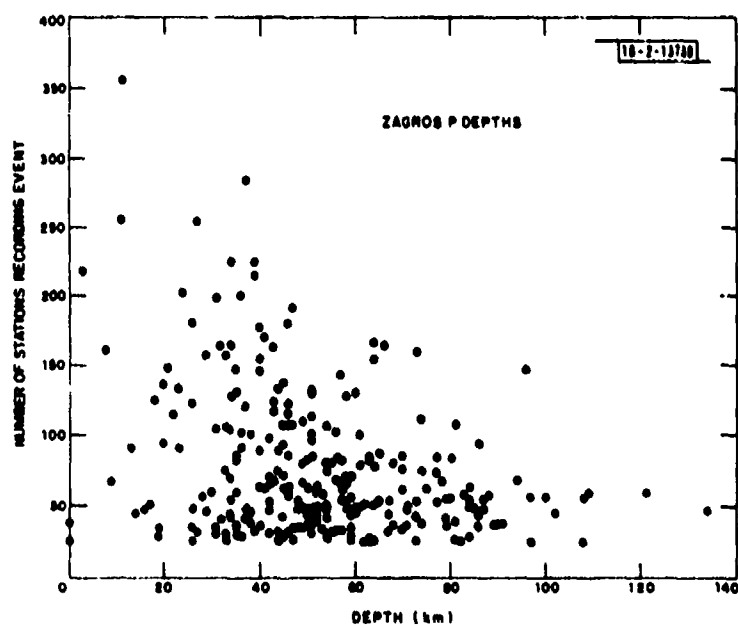


Fig. III-8. Plot of reported depth (ISC) against number of stations recording event. Note that few deeper events are well recorded.

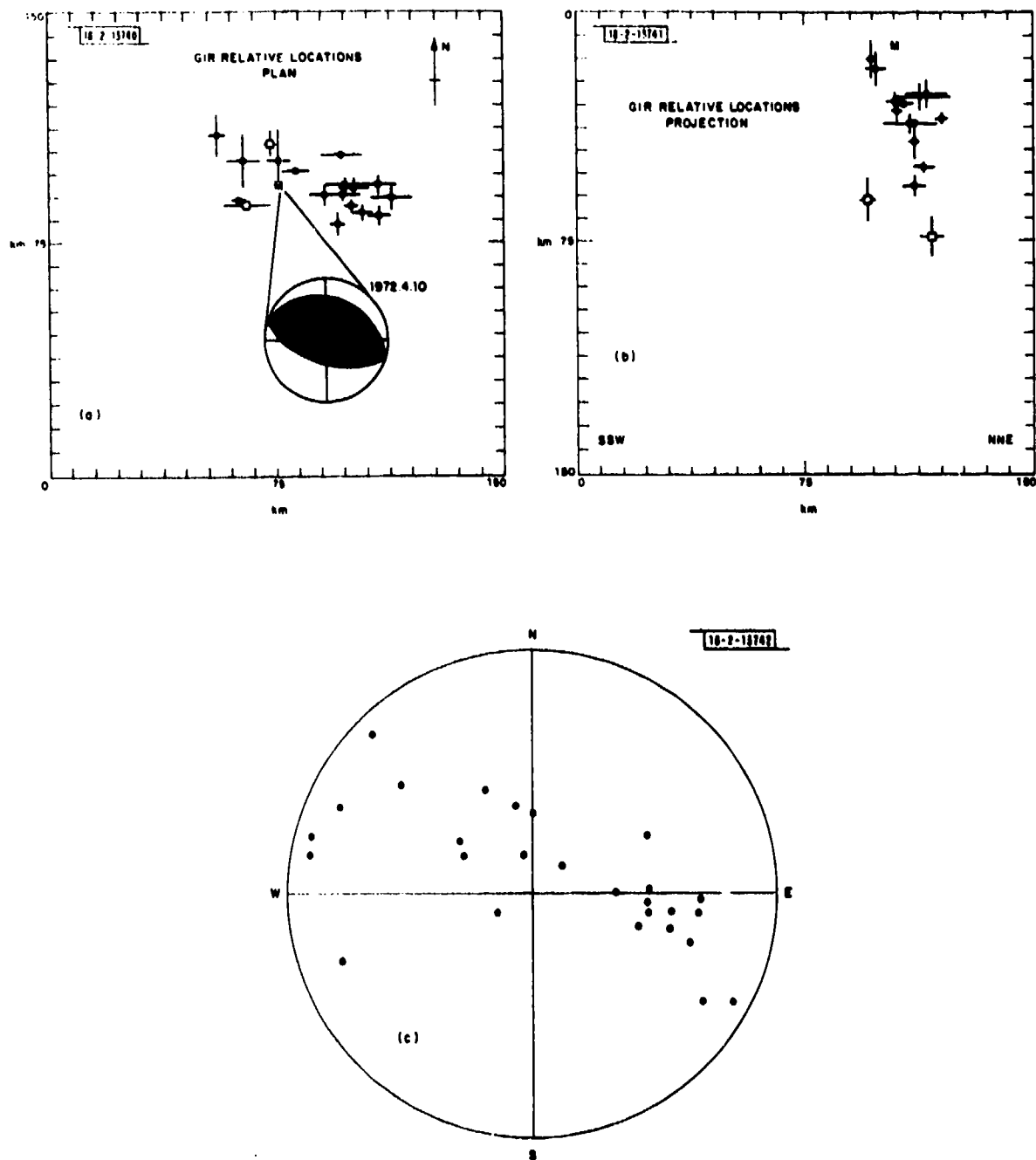


Fig. III-9. (a, b) Relocation of 1972 GIR sequence. Error bars are standard errors checked by  $\chi^2$  tests. Master event, labeled M, is at 28.39°N, 52.78°E, 11 km. Those events with poor station distributions are labeled □. (c) Equal-area plot of position vectors to aftershocks on focal net of master event. Compare trend with mechanism in (a). This is plot of all located activity on fault trend.

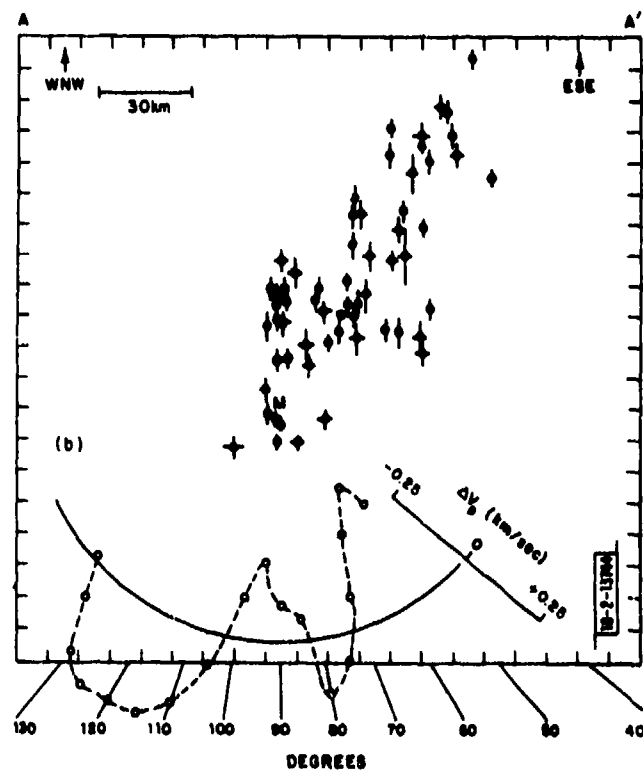
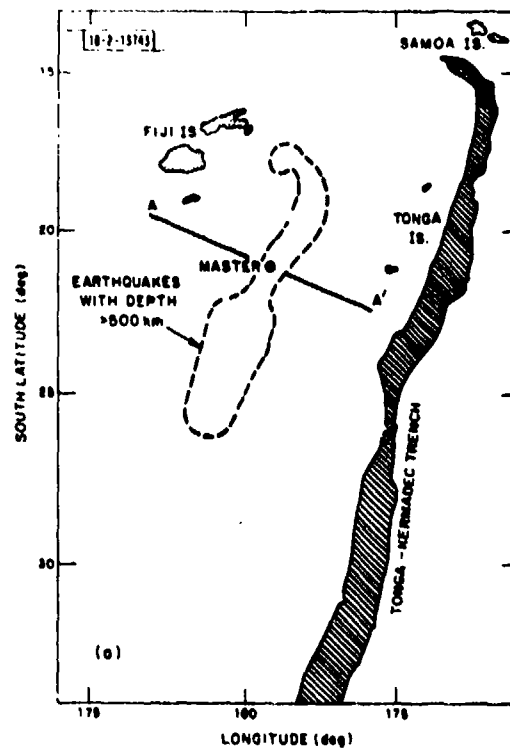
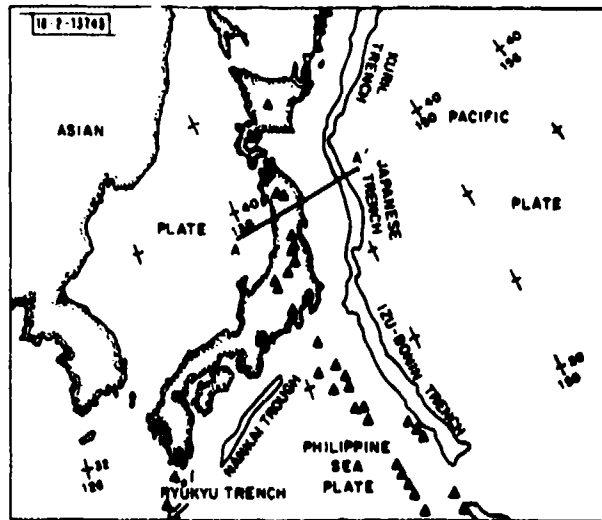


Fig. III-10. (a) Tonga deep seismic zone - a map view. (b) Velocity anomaly pattern.





(a)

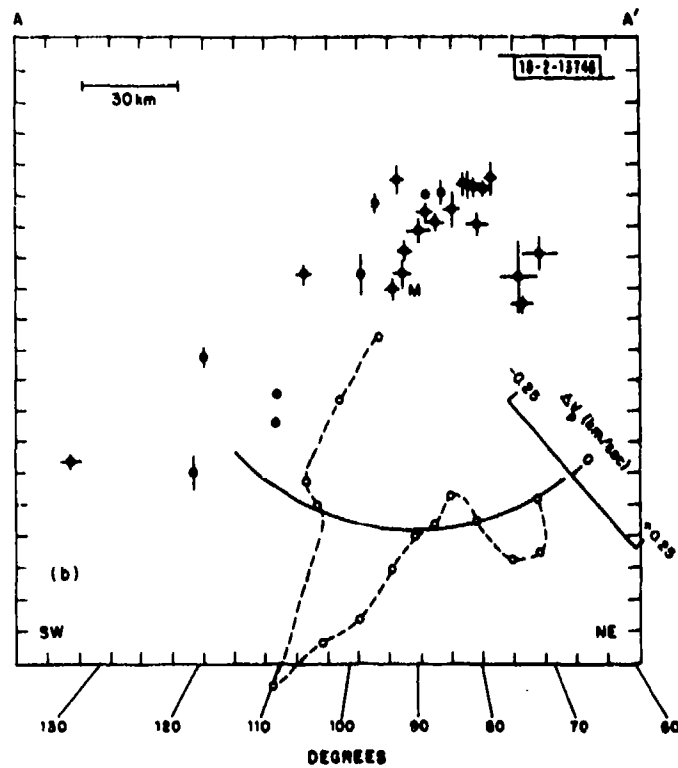


Fig. III-14. (a) Japanese region. (b) Velocity anomaly pattern normal to Honshu intermediate-depth earthquake zone.

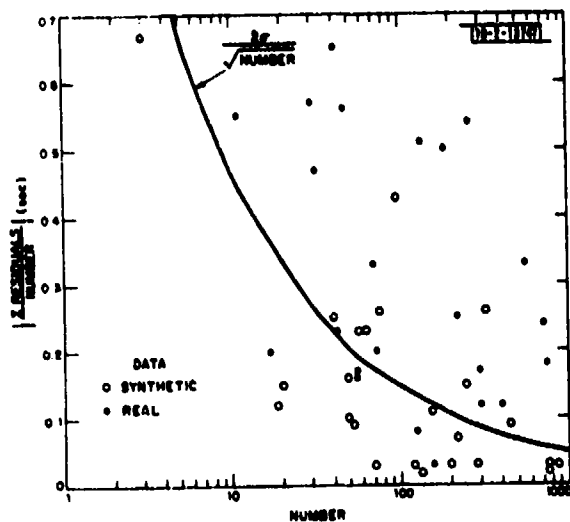
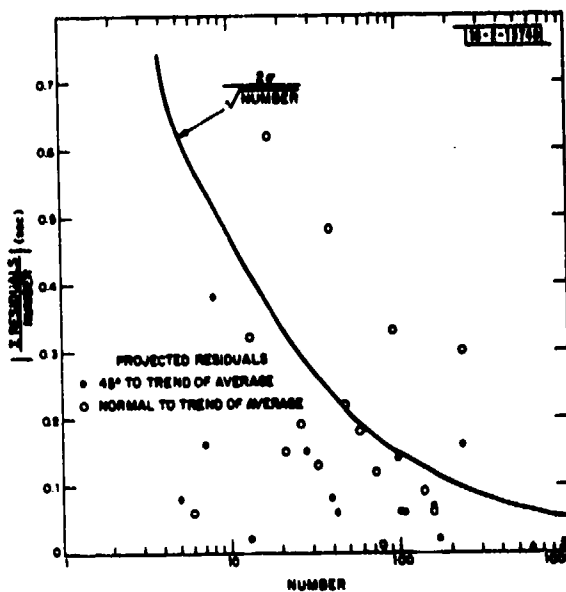


Fig. III-12. Test for randomness: Tonga data.

Fig. III-13. Test for two-dimensionality: Honshu, Japan data.



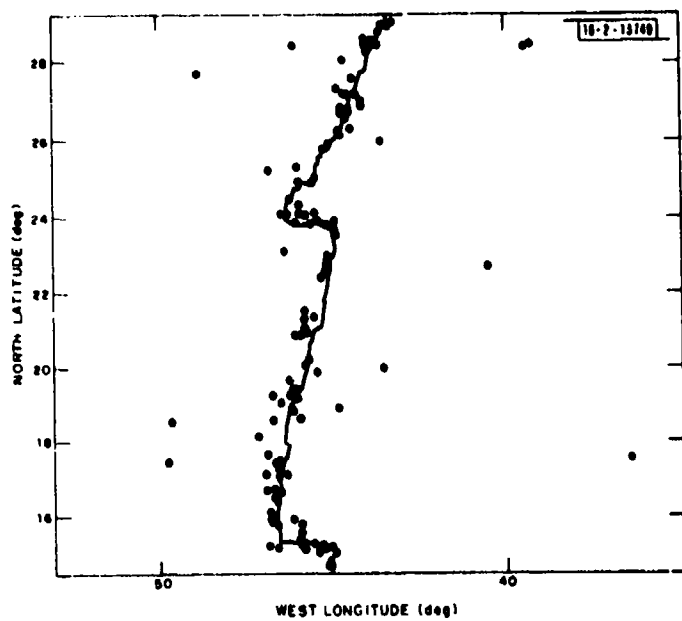


Fig.III-14. Earthquake distribution along a portion of mid-Atlantic ridge.

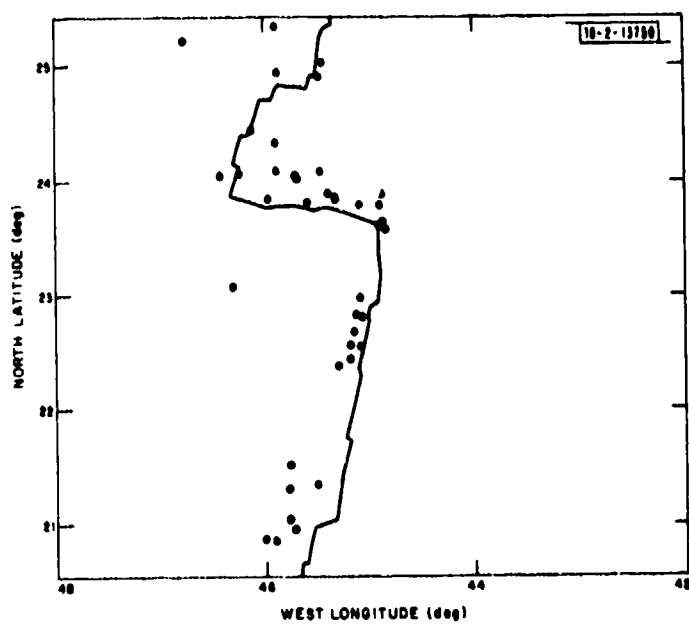


Fig.III-15. Earthquake distribution along Kane Fracture Zone.

#### IV. DATA ANALYSIS AND COMPUTER SYSTEMS

##### A. TRANSFER FUNCTIONS FOR THE SEISMIC RESEARCH OBSERVATORY SEISMOGRAPH SYSTEM

The Seismic Research Observatories (SROs) can produce long-period (LP), short-period (SP), or broadband 3-component data which can be either analog or digital. It is likely that the data, particularly the digital data, will be widely used for seismic research; therefore, it is important that response characteristics be well known and understood. This is particularly important because these seismographs are quite different from classical seismic instrument systems.<sup>1,2</sup>

It is our objective to present here all important dynamic systems' response information which may be needed to understand or interpret SRO data. Our approach is basically that used to design the system. We derive our results, as the designing engineer did, from either circuit diagrams or mathematical specifications. While more involved than approximate methods,<sup>3,4</sup> this procedure allows the overall system response to be divided into individual components. No distinction is made between vertical and horizontal instruments because they have the same response functions.

The models we have constructed are based on information in SRO manuals. In addition, a number of individuals and companies have been very helpful to us in obtaining the SRO information we needed. We particularly want to thank: the White Instrument Company of Houston, Texas for information about the anti-alias filters; the Teledyne-Geotech Company of Garland, Texas for details of the seismometer and shaping filters; Mr. Howard Durham of Sandia Laboratories, Albuquerque, New Mexico for additional inputs covering the seismometer; and Mr. Gary Holcomb of the USGS Albuquerque Seismological Center who has been very cooperative and helpful in obtaining information as we required it.

It is important to note that our models are general, but the SRO SP systems now operate without an anti-alias filter. It appears that the anti-alias filter was removed at all operating sites during the first half of 1976, but at different times. The correct SRO SP response may or may not include the anti-alias filter, depending on what date the recording was made.

##### 1. The Seismometer

The basic SRO seismometer is a Teledyne-Geotech Model 36000 which includes a very lightly damped accelerometer with a natural frequency of approximately 0.2 Hz. A capacitance displacement measurement generates a feedback signal which is, in turn, used to maintain null position. This instrument is therefore similar in design to the lunar seismometer analyzed by Sutton and Latham.<sup>5</sup>

The seismometer has two basic outputs. One,  $v_{bb}$ , is a broadband output which is essentially flat to acceleration inputs from DC to 1.0 Hz. Above 1.0 Hz, the response drops at 12 dB/octave. The other,  $v_f$ , is a filtered response which is similar except that additional filtering causes the response to drop at 6 dB/octave at frequencies below 0.02 Hz. More exactly, the acceleration to broadband output transfer function is

$$\frac{v_{bb}(s)}{a(s)} = H_{bba}(s) = \frac{-197(s + 0.125)(s + 50)}{(s + 0.130)(s + 6.02)(s + 8.66)(s + 35.2)} \quad (IV-1)$$

and the filtered transfer function is

$$\frac{v_f(s)}{a(s)} = i_{fa}(s) = \frac{39,400s(s+50)}{(s+0.130)(s+6.02)(s+8.66)(s+35.2)} \quad (IV-2)$$

where output is measured in volts, and acceleration is in  $\text{cm/sec}^2$ . In both cases, the transfer function for displacement input is obtained by multiplying the above by  $s^2$ .

Figure IV-1(a-b) shows the broadband system response to acceleration inputs. As noted above, the amplitude response is flat from DC to approximately 1.0 Hz. The phase delay is shown assuming that the  $-1$  in  $H_{bba}$  corresponds to a phase shift of  $+\pi$  radians. Figure IV-2(a-b) shows the corresponding filtered response to displacement inputs.

## 2. Response-Shaping Filters

The SRO system produces both LP and SP outputs by further filtering of the filtered output  $v_f$  of the basic seismometer.

### a. LP Response Shaping

The LP shaping filters have been selected to yield a system response to earth displacement having a peak response at a 28-sec period, a 1.25-dB octave separation of  $-3$ -dB points, a 24-dB/octave roll-off at high and low frequencies, and a 6-sec notch to remove microseisms. This has been done by cascading the first four filters with the transfer functions shown in Table IV-1. The fifth filter is also in the system to block DC offsets; it, in fact, increases the roll-off to 30 dB/octave at very long periods. The overall shaping filter transfer function is just the product of the transfer functions in Table IV-1.

### b. SP Response Shaping

The SP shaping filters have been selected to yield a system response to earth displacement having a peak response at a 0.35-sec period (2.86 Hz), a 1.8-dB/octave separation of  $-3$ -dB points, and an 18-dB roll-off toward lower frequencies in the microseism band. The filters applied to the basic seismometer filtered output to achieve this are given in Table IV-2. Note that for frequencies much below 10 Hz, the 10-Hz bandpass filter might as well be a simple differentiator giving 6-dB/octave loss toward lower frequencies.

## 3. Anti-alias Filters

Anti-alias filters were originally applied to both LP and SP analog outputs prior to sampling and digital recording. These filters are introduced to be certain that there is no significant energy remaining above the Nyquist frequency. The anti-alias filters further modify the instrument response, particularly close to and above the Nyquist frequency. As noted above, the SP system now operates with no anti-alias filter and depends upon nature to produce a signal with no energy above 10 Hz (sampling rate is 20 Hz).

### a. LP Anti-alias

The LP anti-alias filter is a 4-pole Butterworth low-pass filter. The response varies smoothly from 0 dB at DC to  $-3$  dB at 0.1 Hz, and then drops to  $-60$  dB at the 0.5-Hz Nyquist frequency.

TABLE IV-1 LONG-PERIOD SHAPING FILTERS	
Description	Transfer Function H(s)
0.166-Hz (6-sec) twin-T notch filter	$\frac{(s + 1.05i)(s - 1.05i)}{(s + 3.93)(s + 0.282)}$
2-pole low-pass filter with undamped natural frequency of 0.05 Hz (20 sec) and relative damping of 0.64	$\frac{0.0986}{(s + 0.201 + 0.241i)(s + 0.201 - 0.241i)}$
2-pole low-pass filter with undamped natural frequency of 0.0266 Hz (37.6 sec) and relative damping of 0.80	$\frac{0.0279}{(s + 0.134 + 0.100i)(s + 0.134 - 0.100i)}$
Single-pole high-pass filter with 0.004-Hz (250-sec) corner	$\frac{s}{s + 0.0251}$
Single-pole high-pass filter with 0.00147-Hz (670-sec) corner	$\frac{s}{s + 0.00942}$

TABLE IV-2 SHORT-PERIOD SHAPING FILTERS	
Description	Transfer Function H(s)
2-pole low-pass filter with corner frequency of 2.86 Hz (0.35 sec) and relative damping of 1.0	$\frac{322.0}{(s + 17.97)^2}$
2-pole bandpass filter with center frequency of 10 Hz and relative damping of 1.0	$\frac{4006.0s}{(s + 63.29)^2}$

The form of the filter transfer function is

$$H_b = \frac{\omega_0^4}{4 \prod_{k=1}^4 (s + s_k)} \quad (\text{IV-3})$$

where  $\omega_0$  is the natural (3-dB) frequency of the filter, and the  $-s_k$  are the poles of the filter. The values for the LP anti-alias filter constants are:

$$\omega_0 = 0.1(2\pi) = 0.628$$

$$s_1 = 0.240 - 0.580i$$

$$s_2 = 0.580 - 0.240i$$

$$s_3 = 0.580 + 0.240i$$

$$s_4 = 0.240 + 0.580i$$

#### b. SP Anti-alias

The original SP anti-alias filter was a 7-pole Tchebychev low-pass filter. It had 0.25-dB ripple, was down 3 dB at 5.0 Hz, and down more than 60 dB at 10.0 Hz. The small ripple and larger number of poles compared with the LP anti-alias filter were required because of the specification of almost 60-dB drop in the single octave from 5.0 to 10.0 Hz.

The form of the filter was

$$H_t = \frac{\sqrt{\prod_{k=1}^7 s_k s_{k*}}}{\prod_{k=1}^7 (s + s_k)} \quad (\text{IV-4})$$

where the  $-s_k$  are the poles of the filter. The numerical values for these were:

$$s_1 = 2.055 - 30.63i$$

$$s_2 = 5.759 - 24.56i$$

$$s_3 = 8.321 - 13.63i$$

$$s_4 = 9.236 - 0.01i$$

$$s_5 = 8.321 + 13.63i$$

$$s_6 = 5.759 + 24.56i$$

$$s_7 = 2.055 + 30.63i$$

The resulting numerator constant in  $H_t$ , selected to give unity gain at DC, was  $1.413 \times 10^9$ .

#### 4. Overall Response Characteristics

The transfer functions in the previous section are complete linear descriptions of the LP and SP responses of the SRO seismic system. We can now consider the overall response characteristics. Figure IV-3(a-b) shows the SRO LP response to displacement, and Fig. IV-4(a-b)

shows the SP response to displacement with and without the anti-alias filters. In both cases, it is clear that the anti-alias filters significantly modify the high-frequency amplitude responses and that there are substantial phase contributions well into the usual frequency bands of interest. Figures IV-6 and IV-8(a-c) show the corresponding system impulse responses.

An important characteristic of seismograph systems is the group delay they introduce. This is the negative of the derivative of the transfer function phase:

$$t_g(\omega) = - \frac{d\phi(\omega)}{d\omega} \quad (\text{IV-5})$$

where  $\phi(\omega)$  is the phase response. We have calculated  $t_g$  for the SRO LP transfer function by numerically differentiating  $\phi(\omega)$ . The resulting group delay curve, computed with and without the anti-alias filter for purposes of comparison, is shown in Fig. IV-5. Since the LP group delay is of interest for a number of applications, we have derived a simple parametric representation. This approximation, which includes the effect of the anti-alias filter, is

$$t_g(\omega) = \frac{1}{(1.551 \times 10^{-2}) + (1.968 \times 10^{-1}\omega) - (3.866 \times 10^{-4}\omega^2) + (9.988 \times 10^{-7}\omega^3) - (8.518 \times 10^{-10}\omega^4)}$$

It gives a root-mean-square error of less than 0.5 sec between a 10- and 150-sec period. The worst fits are at the longer periods, and are as large as 1.25 sec.

Part of the group delay of the LP instrument is due to the anti-alias filter. For example, there is an apparent pure delay of a few seconds on the impulse response shown in Fig. IV-6. That is primarily due to the anti-alias filter. In general, the LP anti-alias filter does little more than introduce that delay and slightly smooth the impulse response. We will see below that this is not the case for the SP system.

It is not customary to calculate or discuss group-delay curves for SP instruments. However, the SRO SP is special and worth considering. Figure IV-7 shows the SP group delay for the SRO and WWSSN SP instruments. The transfer function for the WWSSN is given by Chakrabarty et al.<sup>2</sup> Except near 1 Hz, the SRO with an anti-alias filter clearly introduces more delay. Moreover, the SRO actually has a group delay minimum which corresponds to a buildup of 3-Hz energy with a delay of some 0.35 sec. The WWSSN has small high-frequency delays giving a sharp onset, while the SRO with anti-alias filters has large high-frequency delays giving an emergent onset. The impulse responses shown in Fig. IV-8(a) (SRO with anti-alias filter), IV-8(b) (WWSSN), and IV-8(c) (SRO without anti-alias filter) can be interpreted in terms of the group-delay curves. In particular, the maximum at 0.35 sec and the 5-Hz ringing which comes in later when the system includes an anti-alias filter are clearly visible. Users of very early SP SRO digital data should be aware of these artifacts in the instrument response in order to properly interpret their data.

It should be noted that the current configuration (no anti-alias filter) for the SRO SP system can cause some difficulties. Background noise and most teleseismic signals have relatively little energy at frequencies above a few Hertz. There is usually little energy above 10 Hz to be aliased, so most teleseisms should be faithfully recorded. However, the instrument response is not down very much at 10 Hz, so local noise or events with much more high-frequency content might experience aliasing. It might be prudent to introduce some additional filtering into the SP system, but not a filter as extreme as the original anti-alias filter.

R. T. Lacoss  
D. W. McCowan



## B. DETECTION RESULTS FOR AN SRO NETWORK

The development and installation of a Seismic Research Observatory Network has proceeded to a point that now allows for some analysis of the event detection performance of the observatories. In the normal daily operations of the SROs, an event detector is attached to the output of the seismometer SP vertical channel. Events which are sufficiently large to activate the detector will cause the SP output of the seismometer to be recorded on magnetic tape. A complete list of the event detections and recorded time periods is then maintained in a detection log. About every two weeks, the data tapes are shipped to the USGS. Once the SRO data tapes arrive at Albuquerque Seismological Laboratory, they are processed and checked for data integrity. The detection logs and the actual SRO digital data are then transmitted over the ARPANET to the mass store Datacomputer. Within the Datacomputer, the detection logs are stored in monthly file summaries while the digital data are stored in individual day files. Also within the Datacomputer are monthly bulletin files which have been compiled from stations that rapidly report their arrival times to the USGS. The bulletin files, called PESF or Preliminary Event Summary Files, are meant to provide a very preliminary location only to indicate the time periods of SRO data that may be of further interest. It is the PESF and the SRO detection log files that form the basis of this study.

A comparison of the event detections of an SRO network of stations consisting of ANMO, CTAO, GUMO, MAIO, NWAQ, and ZOBO and the event bulletins in the PESFs of the Datacomputer reveal some interesting figures. There were only six SROs in operation during the 58-day study period, 1 April to 28 May 1977. The detection logs for the SROs were obtained from the detection log files in the Datacomputer. Event locations for the corresponding period were also extracted from the Datacomputer PESFs. A summary of the monthly event totals and SRO detections is given in Table IV-3 where the basic data as extracted from the Datacomputer files are collected and tabulated. During this time period, most of the SROs operated continuously, with two exceptions. The site GUMO was inoperative for the last half of April and the first 5 days of May. CTAO was inoperative during the entire month of May. For the remaining SROs there is a wide variation in the number of event detections reported during the study period. For example, MAIO reported 427 detections, while ZOBO reported 918 for the same time period. NWAQ reported 374, while ZOBO reported 1138 for the same 28-day period in May. Clearly, the event detection thresholds are not in agreement between various SROs. Even accounting for differences in background noise, the sites are not recording detections at consistent detection levels.

TABLE IV-3 NUMBER OF SRO DETECTIONS							
Month	Bulletin Events	ANMO	CTAO	GUMO	MAIO	NWAQ	ZOBO
April	326	532	457	80	427	176	918
May (1-28)	287	652	0	993	394	374	1138

TABLE IV-4 EVENTS DETECTED AS A PERCENT OF TOTAL BULLETIN EVENTS						
Month	ANMO	CTAO	GUMO	MAIO	NWAO	ZOBO
April	52%	30%	46%	45%	16%	50%
May (1-28)	56%	0%	44%	45%	21%	63%

During the 58-day study period, the performance of the SROs varied widely. Using the bulletin event parameters of location and depth, the arrival times were computed for each of the SRO sites. If an SRO detection fell within the computed event arrival time  $\pm 4$  min., the event was considered as being detected at that SRO. In Table IV-4 the events detected are expressed as a percent of the total events in the bulletin and are listed for each SRO for both months. From this table, it is clear that there are two good and two moderately good SROs, and one poor SRO. Because of the extensive down time, data for CTAO are insufficient to draw any conclusions. Both ANMO and ZOBO are operating with a good level of detections, and are recording over 50 percent of the bulletin events. GUMO, when operating, performs as well as MAIO, both detecting somewhat less than 50 percent of the bulletin events. The one site that is in need of improvement is NWAO, although increasing the number of detections at NWAO by lowering the detection threshold may not result in any great increase in real event detections. For example, comparing NWAO and MAIO during May indicates that both sites had about the same number of total detections, yet for NWAO the real events (bulletin events) detected are about half those of MAIO.

Based on the total number of detections listed for these two months, it appears that most of the SROs are operating with a detection threshold that is set too high. Lowering the threshold at NWAO, CTAO, GUMO, and MAIO would increase the total events detected by the network. A clear example of this is seen in the performance of ZOBO.

R. M. Sheppard

### C. AUTOMATIC PICKING OF FIRST ARRIVALS

A simple algorithm is being studied which identifies earthquakes and times first arrivals using data from a local network of single-component seismometers. The algorithm is simple enough that it could easily be implemented on a microprocessor monitoring a single station in real time.

A unique aspect of the algorithm is that it not only picks arrivals, but also objectively determines arrival-time accuracy after arrivals have been picked. Earthquakes are located by an iterative method. First, the most-accurate arrivals are used to locate the event. Then, arrivals which do not agree with this location are repicked using more-sensitive parameter settings. This process is repeated until a stable location is obtained. Using such an algorithm in routine processing of seismic data could require as little as 2 percent of the human effort now required by manual processing and could provide, for the first time, an accurate, objective data base for earthquake research.

The simplest algorithm that seemed to work reliably in most cases was developed. The idea behind this was that the analysis of bugs in this algorithm will show how the algorithm

could be improved. In fact, the bugs that were found are general enough that they must be contended with by any picking algorithm.<sup>6</sup>

There is always an ambiguity associated with measuring the first-arrival time. This is due to the fact that the signal is contaminated with noise, the shape of the arrival is unknown, and the arrival waveform varies from station to station. Thus, the methods of "beam forming" and "matched filtering" are unfortunately not applicable.

However, the first arrival does occur in a context, the features of which can be determined more reliably. These features can be used to suggest where the first arrival should be, and also increase the reliability of the pick. The algorithm uses a simple first-arrival detector followed by additional semantic checks to be sure that the pick is associated with a seismic event. The details of the algorithm are presented in Ref. 6. The algorithms of Stewart,<sup>7</sup> Stevenson,<sup>8</sup> and Allen<sup>9</sup> operate similarly.

The data used to test the algorithm are from a magnitude 3.5 earthquake recorded by the Central California seismic network; 47 seismic tracers were used. Examples of the arrival times determined by the algorithm are shown in Fig. IV-9. The vertical dotted line is the computed arrival time, and the number to the right of it is an estimate of the standard error of the arrival time in seconds. For each trace, 1 sec of noise before and 1 sec of signal after the arrival time are shown. The tick marks are 0.1 sec apart. The portions of the seismograms corresponding to large amplitudes have been removed to clarify the figure. The traces were chosen to show how the algorithm performed under various noise and signal conditions. Note the large variations in the first-arrival waveform.

Of the 47 seismic signals, 3 were correctly classified as telephone-line noise. The arrival times for sharp arrivals usually agreed to within a hundredth of a second of hand picks. For weaker, more ambiguous arrivals, computer picks and hand picks are always within the estimated error calculated by the algorithm.

The programming for a complete automated system has not been finished, but the analysis might proceed as follows. First, the picking algorithm would be operated on all the seismic channels. If the spatial and temporal distribution of arrivals over the network was such that an event was likely to have occurred,<sup>10</sup> the hypothesis that an event had occurred would be pursued. If there were enough accurate arrivals, an attempt would be made to locate the event. For the earthquake studied, 17 arrivals were given accuracies of at least 0.01 sec, and these were used to locate the event. The location found agreed well with that determined from hand-picked arrivals. The arrivals would then be re-examined with a more-sensitive algorithm to adjust the pick if necessary. Arrival-time residuals could provide some information to guide the processing at this point. For example, a positive residual indicates that the arrival is late compared with what the velocity model predicts. Thus, if the station is relatively far from the earthquake (greater than 70 km, say), this suggests that the algorithm should look for a weak longer-period arrival that might be a refracted arrival originally missed. A large negative residual means that the arrival is earlier than predicted, and might suggest that a glitch may precede the actual arrival.

However, one cannot rely on residuals too heavily since they can reflect more the inadequacies of the model than inaccuracy of the picks. For example, although 10 arrivals have residuals greater than 0.5 sec, Station RUS's are the only true gross errors. RUS is the farthest station reporting an arrival, and has a 2.13-sec residual suggesting that a refracted arrival was missed. RUS was repicked using a lower trigger threshold, and a residual of

0.13 sec was obtained. The initial and final picks are shown in Fig. IV-10. It should be noted that the algorithm does not operate reliably using such a reduced threshold.

Thus, the algorithm has the potential of using partial information (in this case, a tentative location) to operate on the data in a way that could not be used otherwise. Using multiple levels of information makes processing much more complicated. However, it provides constraints which are not available at the lower levels of the system. Using simple tests ("triggers") to suggest possibilities allows partial knowledge to be used to control the analysis in a manner which is not irrevocable. That is, an hypothesis can be suggested, and either accepted or rejected, and processing modified accordingly. Thus, the algorithm is truly data adaptive.

K. R. Anderson

#### D. PDP-11 SYSTEM SOFTWARE

During the last six months, we have continued to develop our PDP-11 UNIX software system to meet the needs of the Group. Three important developments have been the installation of a new magnetic-tape driver, the development of a new software maintenance system, and initial work on Multi-Computer UNIX.

The new magnetic-tape driver removes three major defects from the standard UNIX driver: inability to use two tapes simultaneously, inability to process multiple files on one tape, and inability to recover data from tapes with noise and errors.

PDP-11 software maintenance has become a difficulty, because a large volume of software hurriedly imported to get the system going did not have adequate source code or documentation, and because insufficient on-line storage resulted in poor organization of our rather extensive program source code and computer-readable manual libraries. We are now halfway through a project to put all source code and documentation on-line, and to be sure that the source code and documentation correspond to the running system programs. Several simple maintenance programs are being developed to make it possible to keep the system in a crisp, well-maintained state after this initial shakedown is completed. The shakedown and maintenance programs are to be finished by the end of 1977. This project, which requires a considerable effort on our part, is also important to others - such as the VELA Seismological Center, to whom we have promised our software.

The load on our PDP-11/50 running UNIX has become quite heavy, and it is clear that as more-and-more seismological algorithms are programmed for the computer, and as work is further transferred from our now antiquated PDP-7's, one PDP-11 will no longer be adequate. We are in the process of revising UNIX to run on two computers simultaneously, so that we can use our PDP-11/40 to lighten the UNIX load. The PDP-11/40 is the same size as the PDP-11/50, except that its CPU is half the speed; but should CPU speed become a problem, the PDP-11/40 can be easily and cheaply upgraded to a PDP-11/60 which is slightly faster than the PDP-11/50. The revised system, called Multi-Computer UNIX, must share disks and teletypes between the computers. Multi-Computer UNIX has gone through initial design and about half of initial coding since the last semiannual report.

R. L. Walton

#### E. UNIX SIGNAL DISPLAY PACKAGE

Work is being done to implement a general-purpose interactive seismic Signal Display Package (SDP) using storage scope displays to run on our PDP-11 UNIX operating system. To

facilitate this work, the graphics system described in the previous SATS<sup>11</sup> has been expanded to include a command to plot a waveform directly from a UNIX file. Originally, the data would have to have been read by the user program and then passed to the graphics routines. This change not only reduces the time necessary to plot the waveforms, it also saves the user from having to allocate space for the large data arrays.<sup>11</sup>

The current design of the SDP consists of four parts: (1) the seismic waveform database which must be in our standard UNIX waveform format; (2) the general display or interface program; (3) the display command file which is an alphanumeric file of applications-oriented primitive graphics commands describing the display; and (4) a graphics command interpreter which is a subroutine to translate the primitive commands into actual graphic commands.

The standard format for UNIX waveform data consists of an alphanumeric index file and a group of binary data files. The index file contains one line of formatted information describing each waveform, and the data files contain the actual seismograms. This database format is compatible with the SRO magnetic-tape format<sup>11</sup> and the format of the data received from the Datacomputer through the DCREAD program (see Sec. F below).

The general display program will either produce a display from an existing command file or create a default command file for the database. Once the initial display has been made, the program serves as an interface between the user and the display, allowing the user to type in a series of change commands. The program will create a temporary display command file from these changes and modify the display accordingly.

The change commands will allow the user to rescale the data in both x and y, move the waveform left, right, up, or down, change the separation of the waveforms, set up a cursor, align waveforms at the cursor location, and set up a marker at the cursor location. All changes will be plotted without clearing the screen, unless a clear command has been given. The old command file will then be saved in a temporary file and replaced by the modified command file. There will also be a change command which will allow the user to return the display to this previous file.

The input to the display subroutine will be the display command file which can have an unlimited number of lines of varying lengths. The commands are in a free format where the first three items must be the command, the waveform number the command applies to, and a flag which determines whether or not the item should be visible. The remaining parameters in each line of the command specify the details of the display. The display subroutine will evaluate each line of this command file and create graphics commands to produce a single picture. A large portion of the coding for this subroutine has been done. Figure IV-11 shows the display that is the result of processing the following command file:

```
waveform 01 1 0. -1500 1000 2 .5 2000 250
waveform 02 1 0. -1500 0 2 .5 2000 250
waveform 03 1 0. -1500 -1000 2 .5 2000 250
station all 1 -500 200
inst all 1 -500 120
date all 1 -500 40
time all 1 -500 -40
file all 1 -500 -120
comment 01 1 -500 -200
text none 1 -650 -1500 "TEST OF WAVEFORM DISPLAY PACKAGE"
```

The "waveform" command defines where a waveform will appear on the screen and sets up the graphic commands to actually plot the seismogram. There must be a "waveform" command for each waveform file that is to be displayed. The remaining commands in the display command file require an x and y offset from the waveform positions. The "station," "inst," "file," and "comment" commands will retrieve the station code, instrument response and component information, the gram file name, and the comment, respectively, from the index file for this database and plot them on the screen. If date and time commands are given, the display subroutine will calculate the date and time of the first data point in the display window by using the date, time, and sampling interval parameters from the index file. Since the text command is used for labeling and the information is not necessarily associated with one particular gram, "none" is used instead of a gram number.

M. F. Patton  
L. J. Turek

#### F. DATACOMPUTER-RELATED UNIX SOFTWARE

A number of tools have been developed to give us easy access to the seismic data on the Datacomputer. First, we now have a general Datacomputer subroutine package (DCS) which provides the basic Datacomputer functions to any C program. These functions include:

- dcinit -- open a Datacomputer connection
- dccl -- send datalanguage to the Datacomputer
- dcstart -- start a data transfer
- dcopen -- define a separate connection to the Datacomputer
- dcquit -- close the Datacomputer connection

Using the DCS package, we have written a program (DCREAD) to get SRO data from the Datacomputer and store them in the standard UNIX waveform database. A waveform database consists of an alphanumeric index file which contains one line describing each segment of data, and a series of binary files which contain the actual seismograms.

The format of a DCREAD request is the same as the format of the standard waveform index file. It contains a series of lines, each line describing a desired segment of data by its station code, start time, number of samples, SP or LP response, and component. DCREAD processes each line individually; if a data request cannot be satisfied, it gives an error message and moves on to the next line. LP requests will always result in a single output waveform, but SP requests will return a separate output waveform for each data segment found within the requested window.

Because DCREAD does not require any operator interaction, it is practical to construct quite large data requests and to let the program run as long as necessary to retrieve all the data.

There are a few inconveniences involved in using DCREAD for all of our data retrieval. First, DCREAD must access the raw NLPF and NSPF data files. With the current configuration of the Datacomputer, these files are on-line for only a very short time (usually less than a month). Second, since the data must be specified by station name and arrival time, the user has the responsibility of finding an event list and computing the arrival times to be used in the DCREAD request.

To circumvent these problems, we plan to create our own Datacomputer files which will contain event information from the PESF (Preliminary Event Summary File), the computed SRO arrival times, and the associated waveform segments. These files will stay on-line permanently, rather than being cycled off-line along with the raw data, and the waveform data can be accessed via searches directly on the event parameters.

The procedure for setting up these files will include several distinct steps:

- (1) Retrieve the PESF event information for a given time period from the Datacomputer to a local UNIX file.
- (2) Add to this list any additional events that we know about from other sources.
- (3) Retrieve the SP detection windows for the time period. (Start and stop times only.)
- (4) Compute arrival windows for each event at each SRO site for both SP and LP signals. (The SP window will match the SP detection starting nearest to the arrival time. The LP window will start with the origin time and vary in length depending on the site's distance from the event.)
- (5) Move data for those windows from the raw data files to a Lincoln Waveform File (LWF).
- (6) Add the event information and computed arrival times to the Lincoln Event Summary File (LESF).

The program that will carry out these steps is being designed with recovery procedures to insure easy restarting after network failures. Most of the design work for the program is complete, and software for steps (1) and (3) and part of steps (4) and (5) has been written.

L. J. Turek

#### REFERENCES

1. T. Hagiwara, "A Note on the Theory of the Electromagnetic Seismograph," Bull. Earthquake Res. Inst. Tokyo 36, 139-164 (1958).
2. S. K. Chakrabarty and S. N. Roy Choudhury, "Response Characteristics of Electromagnetic Seismographs," Bull. Seismol. Soc. Am. 54, 1445-1458 (1964).
3. B. J. Mitchell and M. Landisman, "Electromagnetic Seismograph Constants by Least-Squares Inversion," Bull. Seismol. Soc. Am. 59, 1335-1348 (1969).
4. P. C. Luh, "A Scheme for Expressing Instrumental Responses Parametrically," Bull. Seismol. Soc. Am. 67, 957-969 (1977).
5. G. H. Sutton and G. V. Latham, "Analysis of a Feedback-Controlled Seismometer," J. Geophys. Res. 69, 3865-3882 (1964).
6. K. R. Anderson, "Automatic Analysis of Microearthquake Data," Proc. Intl. Symp. on Computer Aided Seismic Analysis and Discrimination, Falmouth, Massachusetts, 40-51 (1977).
7. S. W. Stewart, "Real-Time Detection and Location of Local Seismic Events in Central California," Bull. Seismol. Soc. Am. (in press, 1977).
8. P. R. Stevenson, "Microearthquakes at Flathead Lake, Montana: A Study Using Automatic Earthquake Processing," Bull. Seismol. Soc. Am. 66, 61-80 (1976).
9. R. Allen, "Automatic Earthquake Recognition and Timing," paper presented at Workshop on Automatic and Interactive Processing of Network Data, NCER, Menlo Park, California, October 1976.
10. K. R. Anderson, "Automatic Analysis of Microearthquake Data," paper presented at Workshop on Automatic and Interactive Processing of Network Data, NCER, Menlo Park, California, October 1976.
11. Seismic Discrimination SATS, Lincoln Laboratory, M.I.T. (31 March 1977), DDC AD-A045453.

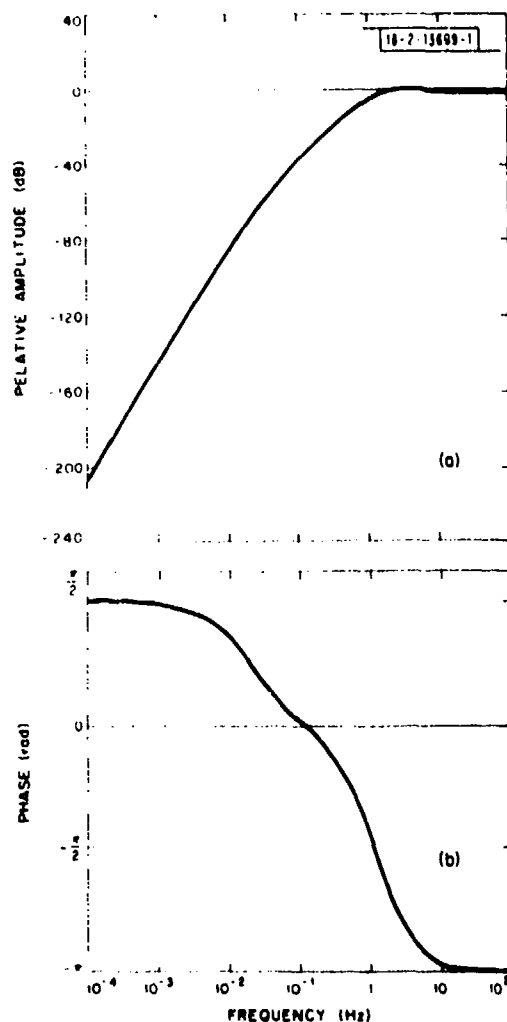


Fig. IV-1. Seismometer broadband response to acceleration input. (a) Amplitude response relative to DC response; (b) phase response. The  $-1$  factor in transfer function corresponds to  $+\pi$  radians phase shift.

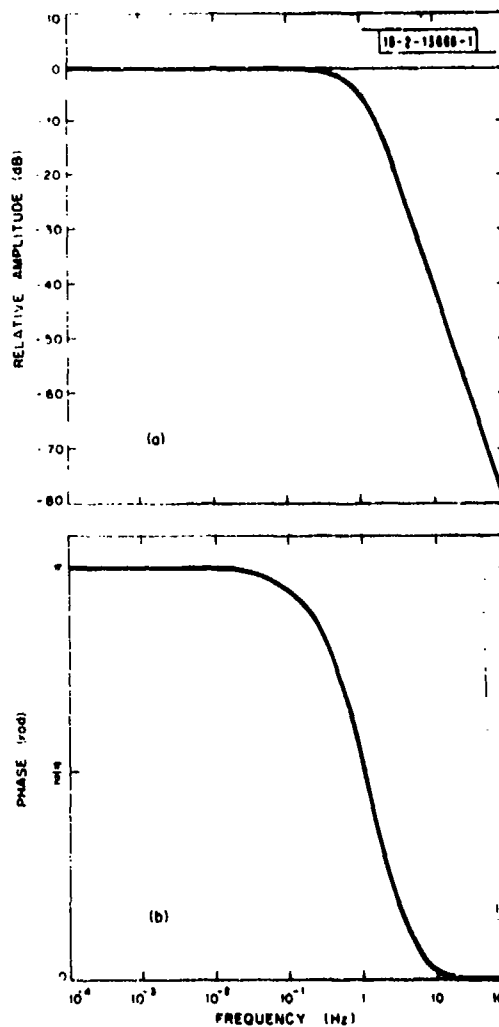


Fig. IV-2. Seismometer filtered response to displacement input. (a) Amplitude response relative to peak value; (b) phase response.



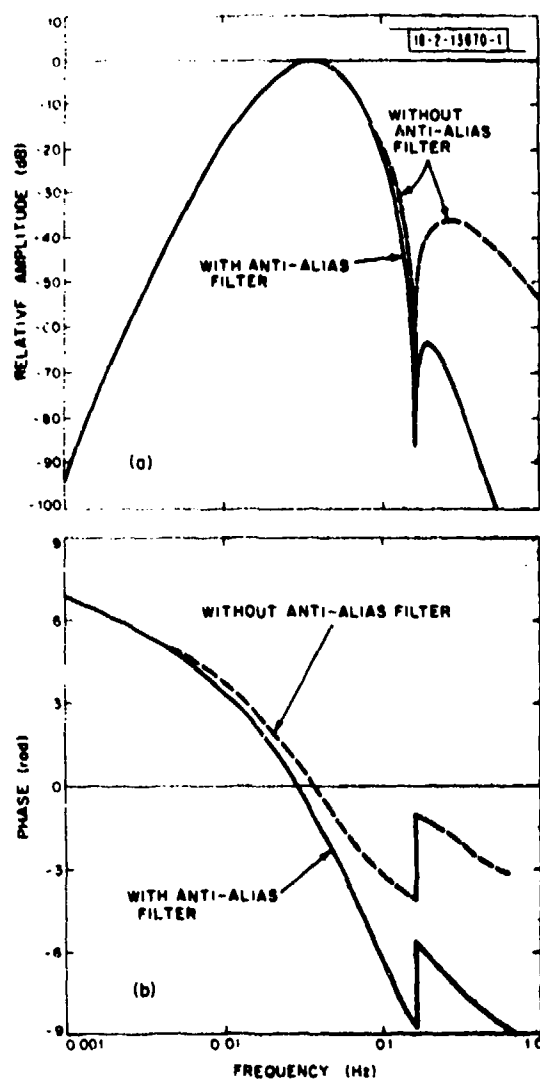


Fig. IV-3. Overall LP SRO response to ground displacement with and without anti-alias filter. (a) Amplitude response; (b) phase response.

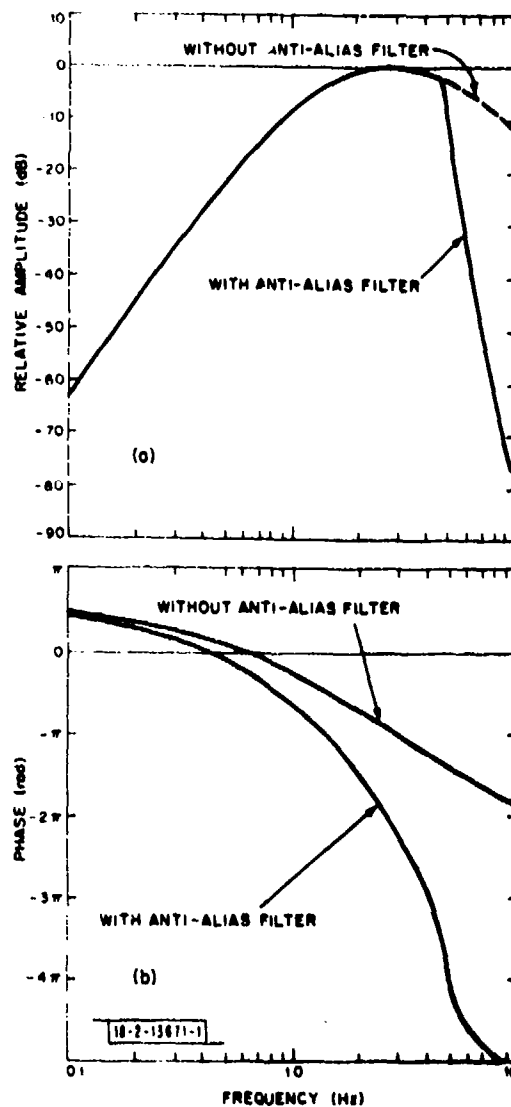


Fig. IV-4. Overall SP SRO response to ground displacement with and without anti-alias filter. (a) Amplitude response; (b) phase response.

Fig. IV-5. Group delay as a function of frequency for the LP SRO instrument.

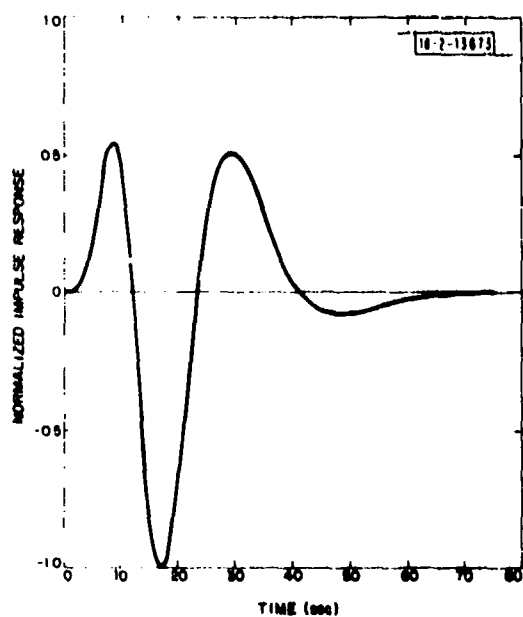
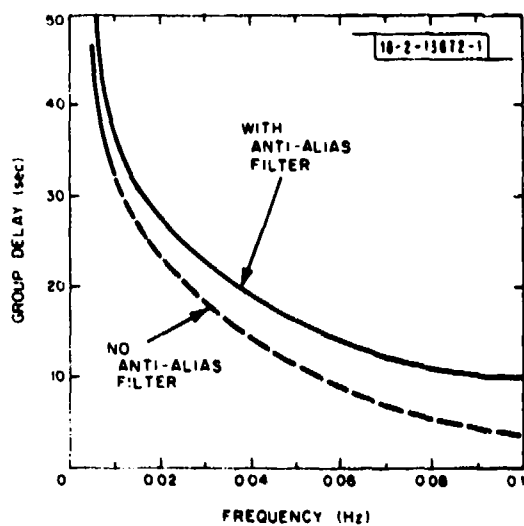


Fig. IV-6. LP SRO response to an impulse of displacement.

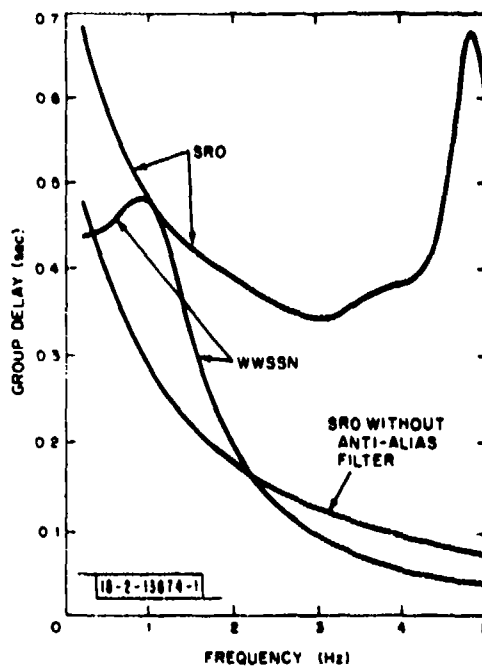


Fig. IV-7. Group-delay curves for SRO and WWSSN SP instruments.

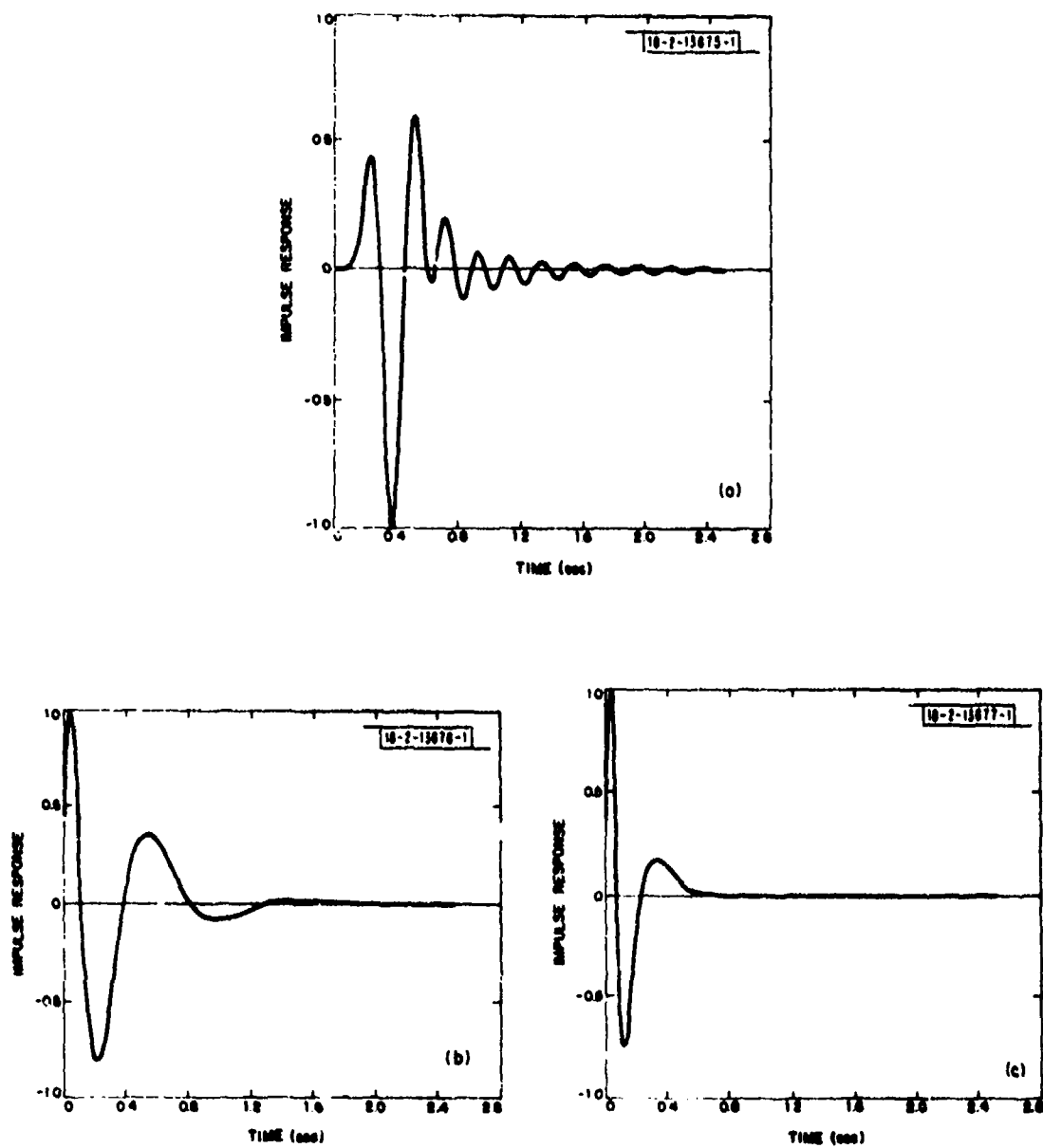


Fig. IV-8. SP responses to an impulse of displacement. (a) SRO including anti-alias filter; (b) WWSSN; and (c) SRO without anti-alias filter.

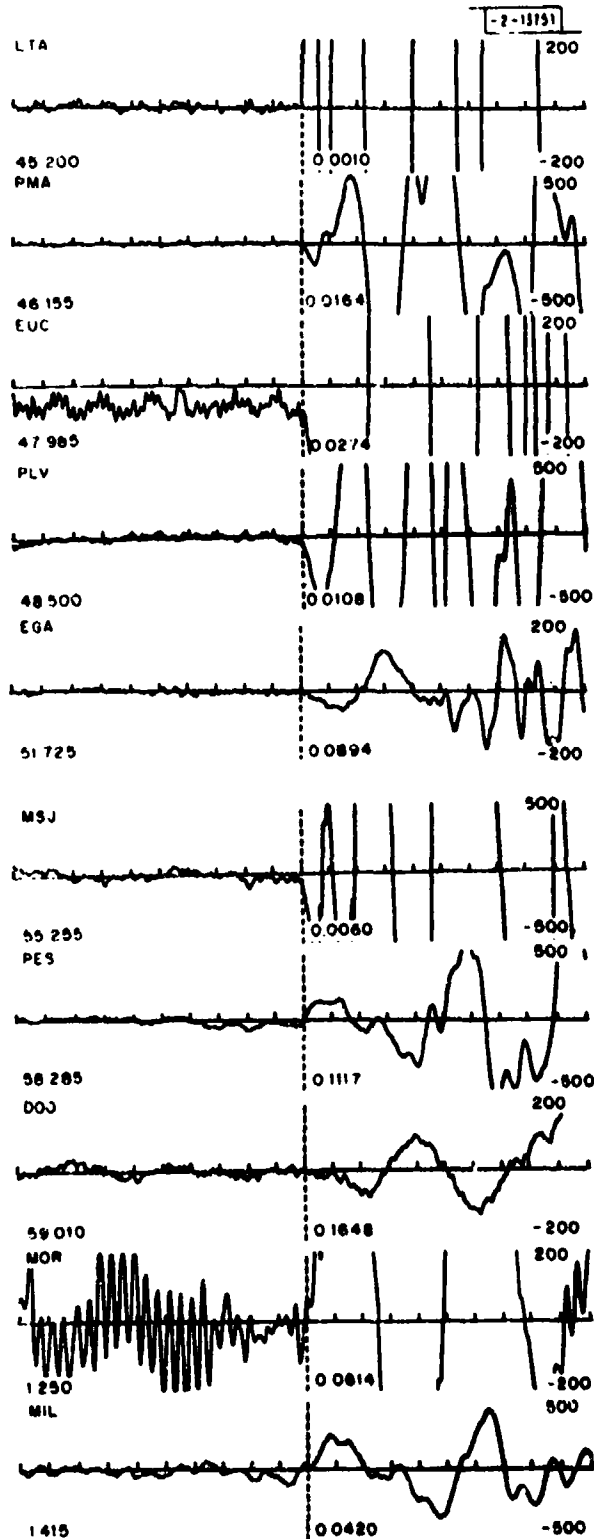


Fig. IV-9. First arrivals determined by computer. Vertical dotted line is computed arrival time, and number to right of it is estimate of standard error of arrival in seconds. For each trace, 1 sec of noise before and 1 sec of signal after arrival time is shown. Tick marks are 0.1 sec apart.

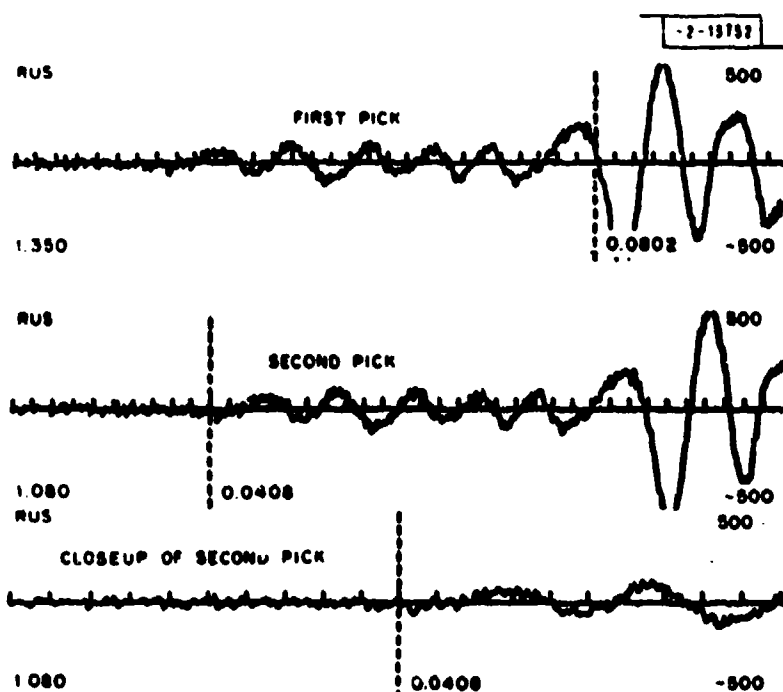
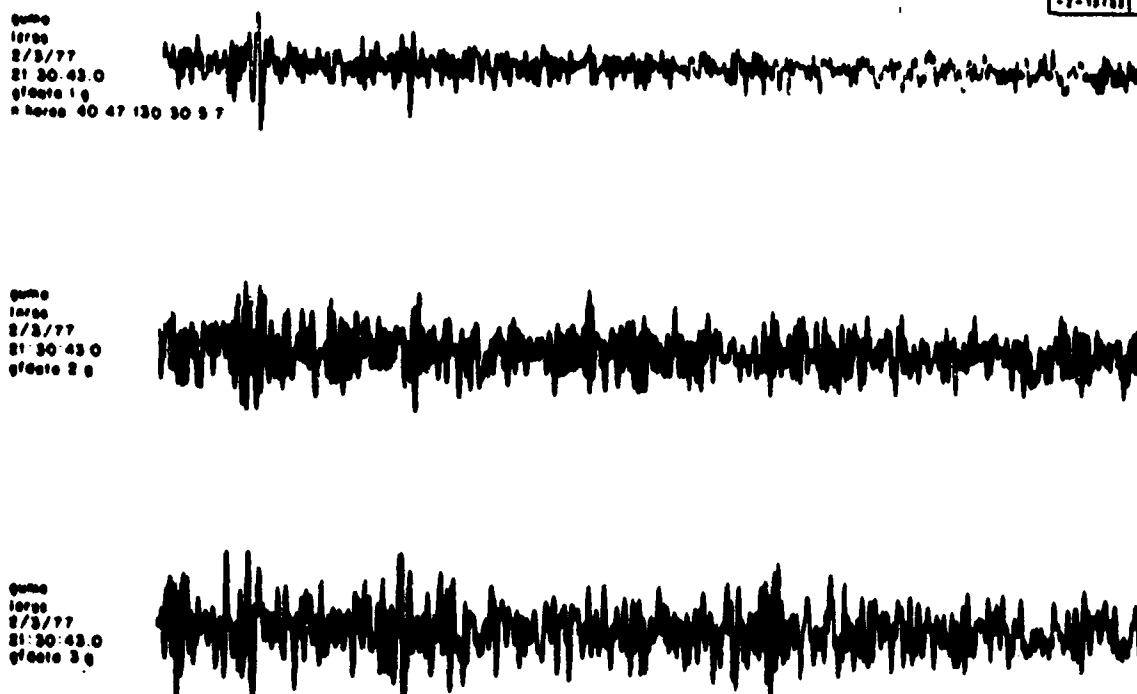


Fig. IV-10. Using a tentative location to constrain arrival time.



TEST OF SEISMIC DISPLAY PACKAGE

Fig. IV-11. Displayed to left of each seismogram are the station code, instrument code, date and time of the first sample, the gram file name, and comment.

## GLOSSARY

ALPA	Alaskan Long-Period Array
ARPANET	DARPA Computer Network
DADS	Data Analysis and Display System
DCS	Datacomputer Subroutine Package
EDR	Earthquake Data Reports
IFFT	Inverse Fast Fourier Transform
ISC	International Seismological Center
J-B	Jeffreys-Bullen (Tables)
LASA	Large Aperture Seismic Array
LP	Long Period
LRSM	Long Range Seismic Measurements
NCER	National Center for Earthquake Research
NTS	Nevada Test Site
PDE	Preliminary Determination of Epicenters
PESF	Preliminary Event Summary File
SATS	Semiannual Technical Summary
SDP	Signal Display Package
SNR	Signal-to-Noise Ratio
SP	Short Period
SRO	Seismic Research Observatory
USGS	United States Geological Survey
WWSSN	World Wide Standard Seismograph Network

UNCLASSIFIED

SECURITY CLASSIFICATION OF THIS PAGE (When Data Entered)

REPORT DOCUMENTATION PAGE		READ INSTRUCTIONS BEFORE COMPLETING FORM
1. REPORT NUMBER <b>18</b> ESD-TR-77-246	2. GOVT ACCESSION NO.	3. RECIPIENT'S CATALOG NUMBER
4. TITLE (and Subtitle) <b>6</b> Seismic Discrimination.	5. DATE OF REPORT & PERIOD COVERED Semiannual Technical Summary 1 Apr - 30 Sep 77 <b>rept.</b>	
7. AUTHOR(s) <b>10</b> Michael A. Chinnery	6. PERFORMING ORG. REPORT NUMBER	
9. PERFORMING ORGANIZATION NAME AND ADDRESS Lincoln Laboratory, M.I.T. P.O. Box 73 Lexington, MA 02173	8. CONTRACT OR GRANT NUMBER(s) <b>15</b> F19628-76-C-0002, <b>ARPA Order-512</b>	
11. CONTROLLING OFFICE NAME AND ADDRESS Defense Advanced Research Projects Agency 1400 Wilson Boulevard Arlington, VA 22209	10. PROGRAM ELEMENT, PROJECT, TASK AREA & WORK UNIT NUMBERS Program Element No. 62701E Project No. 2107	
14. MONITORING AGENCY NAME & ADDRESS (if different from Controlling Office) Electronic Systems Division Hanscom AFB Bedford, MA 01731	11. REPORT DATE 30 Sep 77	
16. DISTRIBUTION STATEMENT (of this Report)  Approved for public release; distribution unlimited.	13. NUMBER OF PAGES 88 <b>12</b> 86p.	
17. DISTRIBUTION STATEMENT (of the abstract entered in Block 20, if different from Report)	15. SECURITY CLASS. (of this report) Unclassified	
18. SUPPLEMENTARY NOTES  None	15a. DECLASSIFICATION DOWNGRADING SCHEDULE	
19. KEY WORDS (Continue on reverse side if necessary and identify by block number)		
seismic discrimination seismic array seismology	surface waves body waves LASA	NORSAR ARPANET
20. ABSTRACT (Continue on reverse side if necessary and identify by block number)  This report describes 21 investigations in the field of seismic discrimination. These are grouped as follows: surface-wave studies (6 contributions), studies of seismic scaling and body-wave magnitude $m_b$ (4 contributions), miscellaneous studies (3 contributions), and investigations related to data analysis and computer systems (6 contributions).		

DD FORM 1 JAN 73 1473 EDITION OF 1 NOV 68 IS OBSOLETE

UNCLASSIFIED

SECURITY CLASSIFICATION OF THIS PAGE (When Data Entered)

207 650-

Hue